TITLE: Impairment of the glial phagolysosomal system drives prion-like propagation in a *Drosophila* model of Huntington's disease

ABBREVIATED TITLE: Phagocytic glial defects drive huntingtin proteotoxicity

AUTHORS and AFFILIATIONS: Graham H. Davis[1,2,3], Aprem Zaya[3], and Margaret M. Panning Pearce[1,2,3,*]

[1]Rowan University, Department of Biological and Biomedical Sciences, Glassboro, NJ 08028, [2]Saint Joseph's University, Department of Biology, Philadelphia, PA 19131, and [3]University of the Sciences, Department of Biological Sciences, Philadelphia, PA 19104

*Correspondence should be addressed to Maggie Panning Pearce at pearcem@rowan.edu.

Number of pages: 48

Number of Figures and Tables: 18 Figures and 4 Tables

Abstract Word Count: 238

Introduction Word Count: 612

Discussion Word Count: 1342

CONFLICT OF INTEREST STATEMENT: The authors declare no competing financial interests.

ACKNOWLEDGMENTS: We would like to thank Sabrina Abbruzzese, Ryan Buist, Georgiana Moore, and David Tomlinson for experimental assistance, and all former and current members of the Pearce Lab for their support and many fruitful discussions about this project. This work was supported by funding from University of the Sciences, Rowan University, the W.W. Smith Charitable Trusts, and the National Institutes of Health (awards NS128847 and AG063295).

ABSTRACT

Protein misfolding, aggregation, and spread through the brain are primary drivers of neurodegenerative diseases pathogenesis. Phagocytic glia are responsible for regulating the load of pathogenic protein aggregates in the brain, but emerging evidence suggests that glia may also act as vectors for aggregate spread. Accumulation of protein aggregates could compromise the ability of glia to eliminate toxic materials from the brain by disrupting efficient degradation in the phagolysosomal system. A better understanding of phagocytic glial cell deficiencies in the disease state could help to identify novel therapeutic targets for multiple neurological disorders. Here, we report that mutant huntingtin (mHTT) aggregates impair glial responsiveness to injury and capacity to degrade neuronal debris in male and female adult *Drosophila* expressing the gene that causes Huntington's disease (HD). mHTT aggregate formation in neurons impairs engulfment and clearance of injured axons and causes accumulation of phagolysosomes in glia. Neuronal mHTT expression induces upregulation of key innate immunity and phagocytic genes, some of which were found to regulate mHTT aggregate burden in the brain. Finally, a forward genetic screen revealed Rab10 as a novel component of Draper-dependent phagocytosis that regulates mHTT aggregate transmission from neurons to glia. These data suggest that glial phagocytic defects enable engulfed mHTT aggregates to evade lysosomal degradation and acquire prion-like characteristics. Together, our findings reveal new mechanisms that enhance our understanding of the beneficial and potentially harmful effects of phagocytic glia in HD and potentially other neurodegenerative diseases.

20 **SIGNIFICANCE STATEMENT**

21 Deposition of amyloid aggregates is strongly associated with neurodegenerative disease
22 progression and neuronal cell loss. Many studies point to glial cells as dynamic mediators of disease,
23 capable of phagocytosing toxic materials, but also promoting chronic inflammation and proteopathic
24 aggregate spread. Thus, glia have emerged as promising therapeutic targets for disease intervention.
25 Here, we demonstrate in a *Drosophila* model of Huntington's disease that neuronal mHTT aggregates
26 interfere with glial phagocytic engulfment, phagolysosomal processing, and innate immunity
27 transcriptional responses. We also identify Rab10 as a novel modifier of prion-like transmission of
28 mHTT aggregates. Our findings add to a growing narrative of glia as double-edged players in
29 neurodegenerative diseases.

30 **INTRODUCTION**

31 Neuron-glia crosstalk is critical for maintaining homeostasis in the central nervous system
32 (CNS), and disruption of these intercellular interactions is increasingly recognized as a central
33 component of many neurological disorders, including neurodegenerative diseases. Glia perform
34 immune surveillance functions in the CNS and respond to neuronal injury by altering gene expression
35 (Magaki et al., 2018) and clearing damaged cells (Raiders et al., 2021; Zheng and Tuszynski, 2023).
36 These glial responses may initially be neuroprotective, but prolonged glial reactivity propels the
37 neurodegenerative disease state, for example, by driving premature loss of living neurons or functional
38 synapses (Neniskyte et al., 2011; Hong et al., 2016; Dejanovic et al., 2022) and inducing
39 neuroinflammation (Liddelow et al., 2017). Expanding our understanding of how glia influence neuron
40 function and survival could reveal promising new therapeutic strategies for neurodegenerative
41 diseases.

42 A pathological hallmark of most neurodegenerative diseases is the accumulation of misfolded
43 proteins into intra- or extracellular amyloid aggregates in vulnerable regions of the CNS (Knowles et al.,
44 2014). Protein aggregates form due to age-associated decline in cellular protein folding capacity
45 (Santra et al., 2019; Stein et al., 2022) and overwhelming of degradative pathways, including the
46 ubiquitin-proteasome system, autophagy, and phagocytosis (Aman et al., 2021; Duong et al., 2021;
47 Wodrich et al., 2022). As professional phagocytes of the brain, microglia and astrocytes clear damaged
48 and dysfunctional cells (Paolicelli et al., 2011; Wakida et al., 2018; Herzog et al., 2019; Lee et al., 2021)
49 and other pathogenic material, such as protein aggregates (Liu et al., 2017; Choi et al., 2020).
50 Defective glial clearance of debris may be a driving force underlying neurodegenerative disease,
51 highlighted by a growing list of genetic risk variants associated with phagocytic and endolysosomal
52 pathways (Podleśny-Drabiniok et al., 2020). Endolysosomal impairment promotes protein aggregate
53 accumulation; in turn, aggregates can drive further endolysosomal dysfunction, including deacidification
54 and membrane permeabilization of intracellular vesicles (Krasemann et al., 2017; Heckmann et al.,
55 2019; Burbidge et al., 2022; Lee et al., 2022). Aggregates that escape degradation may gain the ability

56 to spread and seed soluble proteins in a prion-like manner (Jucker and Walker, 2018; Monaco and
57 Fraldi, 2020).

58 Mechanisms by which pathogenic aggregates dysregulate endolysosomal processing remain
59 largely unknown. Intracellular membrane fusion events that regulate endo/phagosome maturation are
60 catalyzed by Rab GTPases (Ng and Tang, 2008; Chan et al., 2011; Langemeyer et al., 2018), enzymes
61 that cycle between active (GTP-bound) and inactive (GDP-bound) states to organize endomembranes
62 into distinct functional domains (Hall, 1990; Chan et al., 2011). Rab dysfunction is implicated in several
63 neurodegenerative diseases—e.g., upregulation of Rab4, Rab5, Rab7, and Rab27 has been observed
64 in Alzheimer's disease (AD) (Ginsberg et al., 2011), and several Rabs are known substrates of leucine
65 rich repeat kinase 2 (LRRK2), a genetic risk factor in familial Parkinson's disease (PD) (Jeong et al.,
66 2018). Intriguingly, spread of α-synuclein between cultured neuronal and enteroendocrine cells is
67 mediated by the LRRK2 substrate Rab35 (Bae et al., 2018; Rodrigues et al., 2022), suggesting that
68 Rab-dependent processes may contribute to formation and propagation of pathogenic aggregate
69 seeds.

70 Here, we investigated the impact of protein aggregates generated in neurons on phagocytic glial
71 cell functions in a *Drosophila* model of Huntington's disease (HD). We report that neuronal expression
72 of aggregation-prone mutant huntingtin (mHTT) protein reduces the ability of glia to clear axonal debris
73 and to mount phagocytic and innate immunity transcriptional responses following acute nerve injury.
74 We also observed mHTT-induced changes to numbers of glial lysosomes and Rab+ vesicles in
75 uninjured brains, and identify Rab10 as a novel modifier of prion-like spreading of mHTT aggregates in
76 adult fly brains. Together, these studies shed light on mechanisms by which phagocytic glia respond to
77 and are impaired by accumulation of pathogenic aggregates in neurons.

78 **MATERIALS AND METHODS**

79 *Fly husbandry*

80 Fly stocks and crosses were raised on standard cornmeal/molasses media on a 12 hr light/12 hr
81 dark cycle at 25°C, unless otherwise noted. No sex-specific differences were observed in any
82 experiments, so both males and females were utilized in this study. Transgenic or mutant flies were
83 either generated for this study (described below), purchased from Bloomington Drosophila Stock
84 Center, or kindly provided by collaborators. Genotypes and sources of all fly stocks used in this study
85 are listed in Table 1, and complete genotypes of flies used in each figure are listed in Table 2.

86 Acute antennal nerve injury was performed by bilateral removal of the second and third antennal
87 segments from anesthetized adult flies (MacDonald et al., 2006). For quantitative PCR analyses,
88 maxillary palps were removed in addition to third antennal segments to sever all olfactory receptor
89 neuron (ORN) axons. Axotomized flies were incubated for the indicated times on standard media prior
90 to dissection and processing for imaging.

91

92 *Cloning and Drosophila transgenesis*

93 pUASTattB(HTT$_{ex1}$Q25-V5) and pUASTattB(HTT$_{ex1}$Q91-V5) plasmids were cloned by PCR
94 amplification of HTT exon 1 (HTT$_{ex1}$) cDNA using a reverse primer that inserted an in-frame, C-terminal
95 V5 epitope tag (GKPIPNPLLGLDST) and ligation into the pQUASTattB vector backbone via XhoI and
96 XbaI restriction sites. pQUASTattB(HTT$_{ex1}$Q25-GFP) and pQUASTattB(HTT$_{ex1}$Q91-GFP) were
97 generated by replacing the mCherry sequence in pQUASTattB(HTT$_{ex1}$Q25-mCherry) and
98 pQUASTattB(HTT$_{ex1}$Q91-mCherry) plasmids previously generated by our lab (Pearce et al., 2015) with
99 an in-frame, C-terminal GFP sequence via Gibson Assembly (New England Biolabs, Inc. Ipswich, MA).
100 pUASTattB(pHluorin-HTT$_{ex1}$Q25-tdTomato) and pUASTattB(pHluorin-HTT$_{ex1}$Q91-tdTomato) plasmids
101 were generated by PCR amplification of HTT$_{ex1}$ cDNAs and subcloning to replace the CD4 sequence in
102 the pUASTattB(MApHS) plasmid (Han et al., 2014) via In-Fusion cloning (Takara Bio USA, Inc.,
103 Mountain View, CA). pUASTattB(mCherry-Galectin-3) and pUASTattB(mCherry-Galectin-8) were
104 cloned by PCR amplification of human LGals3 and LGals8 cDNAs from the pHAGE-mKeima-LGALS3

105 and pHAGE-FLAG-APEX2-LGALS8 plasmids (Addgene plasmids #175780 and #175758, Watertown,
106 MA) (Eapen et al., 2021) and insertion downstream of an in-frame mCherry sequence in the pUASTattB
107 vector backbone via Gibson Assembly.
108 Plasmids were microinjected into *w-* embryos with the su(Hw)attP8, attP24, VK19, or VK27
109 φC31 attP integration sites at BestGene, Inc (Chino Hills, CA). Table 1 lists detailed genotype
110 information for all transgenic flies generated in this study.
111
112 *Drosophila brain dissection and sample preparation*
113 Adult fly brains were dissected in ice-cold phosphate-buffered saline (PBS) containing either no
114 detergent or 0.03% (PBS/0.03T), 0.1% (PBS/0.1T), or 0.3% (PBS/0.3T) Triton X-100. Dissected brains
115 were fixed in 4% paraformaldehyde (PFA) in the dark at room temperature (RT) for 20 minutes. For
116 imaging of GFP or mCherry fluorescence signals, brains were washed 7X in PBS/0.03T buffer before
117 incubation in Slowfade Gold Antifade Mountant (Invitrogen, Carlsbad, CA). When imaging pHluorin-
118 tagged and other pH-sensitive constructs, such as GFP-LAMP1, brains were washed 7X in PBS for at
119 least 50 minutes at RT before incubation in Slowfade. For immunostaining, brains were washed 7X in
120 PBS/0.3T after fixation, blocked in PBS/0.3T containing 5% normal goat serum (Lampire Biological
121 Laboratories, Pipersville, PA) for 30 min at RT, incubated in primary antibodies diluted in blocking
122 solution for 24-48 hours at 4°C, washed 7X in PBS/0.3T, and then incubated in secondary antibodies
123 diluted in blocking solution for 16-20 hours at 4°C. After a final set of 7X PBS/0.3T washes, dissected
124 brains were incubated in Slowfade. For Magic Red and LysoTracker staining, brains were dissected in
125 PBS and incubated in 1:1,000 LysoTracker Red DND-99 (Invitrogen, Carlsbad, CA) or 1:1,250 Magic
126 Red (ImmunoChemistry, Davis, CA) diluted in PBS for 20 minutes at RT. Brains were washed 5X in
127 PBS for 15 min total, fixed in 4% PFA in PBS/0.1T for 20 minutes at RT, washed 6X in PBS/0.1T for 30
128 min total, and incubated in Slowfade. Following incubation in Slowfade for 1-24 hours at 4°C in the
129 dark, all brains were bridge-mounted in Slowfade on glass microscopy slides under #1.5 cover glass,
130 and edges were sealed using clear nail polish.

131 Primary antibodies used in this study include: chicken anti-GFP (RRID: AB_300798; 1:1,000;
132 Abcam, Cambridge, UK), chicken anti-GFP (RRID: AB_2534023; 1:500; Thermo Fisher Scientific Inc.,
133 Waltham, MA), rat anti-N-cadherin (clone DN-Ex #8; RRID: AB_528121; 1:75; Developmental Studies
134 Hybridoma Bank, Iowa City, IA), mouse anti-Repo (clone 8D12; RRID: AB_528448; 1:25;
135 Developmental Studies Hybridoma Bank, Iowa City, IA), mouse anti-V5 (RRID: AB_2556564; 1:125;
136 Thermo Fisher Scientific Inc., Waltham, MA), and rabbit anti-Draper (1:500; a kind gift from Marc
137 Freeman, Vollum Institute, Portland, OR). Secondary antibodies include: AlexaFluor 405 goat anti-
138 rabbit (RRID: AB_221605; 1:250), FITC-conjugated donkey anti-chicken (RRID: AB_2340356; 1:250;
139 Jackson Immuno Research Labs, West Grove, PA), AlexaFluor 568 goat anti-mouse (RRID:
140 AB_2534072; 1:250), AlexaFluor 647 goat anti-rabbit (RRID: AB_2535812; 1:250), and AlexaFluor 647
141 goat anti-rat IgGs (RRID: AB_141778; 1:250) (Invitrogen, Carlsbad, CA).
142
143 *Image acquisition*
144 All microscopy data were collected on a Leica SP8 laser-scanning confocal system equipped
145 with 405 nm, 488 nm, 561 nm, and 633 nm lasers and 40X 1.3 NA or 63X 1.4 NA oil objective lenses.
146 Leica LAS-X software was used to establish optimal settings during each microscopy session and to
147 collect optical z-slices of whole-mounted brain samples with Nyquist-optimized sampling criteria.
148 Optical zoom was used to magnify and establish a region of interest (ROI) in each sample. For images
149 showing a single glomerulus, confocal slices were collected to generate ~73 x 73 x 20 μm (*xyz*) stacks,
150 with z-axis boundaries established using fluorescent signal in DA1 or VA1lm ORN axons. For images of
151 a single antennal lobe, confocal slices were collected to generate ~117 x 117 x 26 μm (*xyz*) stacks,
152 which were located using HTT_{ex1} fluorescence in ORN axons.
153
154 *Post-imaging analysis*
155 Raw confocal data were analyzed in 2D using ImageJ/FIJI (RRID:SCR_002285; NIH, Bethesda,
156 MD) or in 3D using Imaris image analysis software (RRID:SCR_007370; Bitplane, Zürich, Switzerland).
157 Methods used for image segmentation and semi-automated quantification of fluorescent signals were

158 previously described (Donnelly et al., 2020). Briefly, raw confocal data were cropped to establish an
159 ROI for further analysis and displayed as a 2D sum intensity projection (ImageJ) or a 3D volume
160 (Imaris). Background fluorescence was subtracted from raw confocal images. mCD8-GFP and HTT_{ex1}-
161 mCherry fluorescent signals was segmented using the 'Surfaces' function in Imaris (surface detail =
162 0.25 μm, background subtraction = 0.75 μm). Using the 'split touching objects' option, seed point
163 diameter was set to 0.85 μm. pHluorin- and tdTomato-labeled VA1lm ORN axons were quantified in
164 central 30 x 30 pixels, 50-slice ROIs from sum intensity projections of each VA1lm glomerulus.
165 pHluorin- and tdTomato-labeled Or83b+ ORN axons or MBN soma were quantified from central 100 x
166 100 pixels, 75-slice ROIs of each antennal lobe or mushroom body calyx, and background intensity was
167 subtracted from sum intensity projections. Quantification of Toll-$6^{MIMICGFP}$ fluorescence was performed
168 using the 'Spots' function in Imaris (*xy* diameter = 0.5 μm, *z*-diameter = 1.0 μm), and glial nuclei-
169 associated GFP-Jra signal was quantified using the "Surfaces" function to identify Repo+/GFP+ nuclei
170 (surface detail = 0.2 μm, background subtraction = 1.6 μm, number of voxels >10).
171 mCherry-tagged $mHTT_{ex1}$ and GFP-tagged $wtHTT_{ex1}$ aggregates were identified and quantified
172 as previously reported (Donnelly et al., 2020). Briefly, mCherry+ surfaces were segmented and
173 measured in Imaris (surface detail = 0.2 μm, background subtraction = 0.45 μm, seed point diameter =
174 0.85 μm). Seeded $wtHTT_{ex1}$ aggregates were identified as $mHTT_{ex1}$-mCherry+ objects that overlapped
175 with $wtHTT_{ex1}$-GFP signal. Intracellular vesicles were identified using the 'Surfaces' algorithm in Imaris
176 (surface detail = 0.2 μm, background subtraction = 0.4 μm, volume >0.001 μm^3) to segment fluorescent
177 signals associated with lysosomes (MR+, LTR+, LAMP1-GFP+, GFP-LAMP1+, mCherry-Galectin-3+,
178 or mCherry-Galectin-8+) or phagosomes (YRab+ or YFP-Rab+). Intracellular vesicles associated with
179 $mHTT_{ex1}$ aggregates were identified by filtering for lysosomal or phagosomal surfaces within 0.2 μm of
180 $mHTT_{ex1}$ objects using the "Shortest Distance" calculation in Imaris.
181
182 *qPCR*
183 Transgenic *Drosophila* were flash frozen in liquid nitrogen, and heads were collected using a
184 microsieve with a 230 nm filter to separate bodies from heads and 170 nm filter to separate heads from

185 appendages. Total RNA was extracted from isolated fly heads using the Zymo Direct-Zol RNA miniprep
186 kit (Zymo Research, Irvine, CA). Extracted RNA was quantified on a Nanodrop 2000 (Thermo Fisher
187 Scientific), and equal quantities of each sample were subjected to cDNA synthesis using the High-
188 Capacity cDNA Reverse Transcription Kit (Applied Biosystems, Waltham, MA). qPCR was performed
189 on a T100 Thermal Cycler with a CFX384 Real-Time System (Bio-Rad Laboratories, Hercules, CA)
190 using 10 ng of input RNA per replicate and TB Green Premix Ex Taq II (Takara Bio, Kusatsu, Japan).
191 Sequences of all qPCR primers used in this study are listed in Table 3.
192
193 *Experimental design and statistical analyses*
194 All quantified data were organized and analyzed in Prism 9 software (Graphpad, San Diego,
195 CA). Power analyses to determine appropriate sample sizes for each experiment were calculated using
196 a Sample Size calculator available at ClinCalc.com ($\alpha = 0.05$, $\beta = 0.2$). All quantifications are graphed
197 as mean ± standard error of the mean (s.e.m). A single glomerulus or antennal lobe represented one
198 biological replicate. Statistical comparisons were performed using the following tests where appropriate:
199 unpaired, two-tailed *t*-test when comparing two samples and ANOVA followed by *post hoc* multiple
200 comparison tests when comparing ≥3 samples. Detailed statistical information for each experiment,
201 including sample sizes (*n*), means, and test results are summarized in Table 4.

202 **RESULTS**

203 *Expression of mHTT exon 1 fragments in neurons inhibits phagocytic clearance of axonal debris*

204 HD is a monogenic neurodegenerative disease caused by expansion of a CAG repeat region in
205 exon 1 of the *huntingtin* (*HTT/IT15)* gene beyond a pathogenic threshold of 37 repeats, leading to
206 production of mHTT proteins containing expanded N-terminal polyglutamine (polyQ≥37) tracts
207 (Scherzinger et al., 1999). mHTT proteins are prone to misfolding and accumulate into insoluble
208 aggregates (Wanker, 2000), whereas wild-type HTT (wtHTT) proteins containing polyQ≤36 tracts
209 remain soluble unless seeded by a pre-formed HTT aggregate (Preisinger et al., 1999; Chen et al.,
210 2001). To recapitulate these molecular features of HD, we generated transgenic flies that express N-
211 terminal exon 1 fragments of human mHTT ($mHTT_{ex1}$) containing a polyQ91 tract or wtHTT ($wtHTT_{ex1}$)
212 with a polyQ25 tract via the GAL4-UAS (Brand and Perrimon, N., 1993) or QF-QUAS binary expression
213 systems (Potter and Luo, 2011). As we have previously reported (Pearce et al., 2015; Donnelly et al.,
214 2020), fluorescent protein fusions of $mHTT_{ex1}$ and $wtHTT_{ex1}$ appeared punctate (i.e., aggregated or
215 insoluble) or diffuse (i.e., soluble), respectively, in axon termini of the DA1 type of olfactory receptor
216 neurons (ORNs), which synapse in the DA1 glomerulus of the antennal lobe in the central brain of adult
217 flies (Couto et al., 2005) (Fig. 1A and B).

218 To monitor the capacity of glia to maintain CNS homeostasis in the presence of $mHTT_{ex1}$
219 aggregates, we performed a series of experiments that quantified glial responses to acute injury in the
220 adult fly CNS. Surgical removal of the second and third antennal segments initiates Wallerian
221 degeneration of ORN axons, inducing a robust phagocytic glial response that involves upregulation of
222 the scavenger receptor, Draper, and clearance of axonal debris within 7 days (MacDonald et al., 2006).
223 To determine if neuronal $mHTT_{ex1}$ expression affects the ability of glial cells to efficiently clear axonal
224 debris, we co-expressed mCherry-tagged HTT_{ex1} transgenes with membrane-targeted GFP (mCD8-
225 GFP) in DA1 ORNs and measured GFP and mCherry fluorescence intensities following antennal nerve
226 axotomy (Fig. 1A-D). Interestingly, $mHTT_{ex1}$ expression was associated with reduced steady-state
227 mCD8-GFP levels in DA1 ORN axons in 2 and 4 week-old flies (Fig. 1E), likely due to neurotoxicity
228 caused by accumulation of $mHTT_{ex1}$ aggregates over time. Quantification of DA1 ORN axons remaining

229 after antennal nerve injury revealed that clearance of axonal debris was reduced in flies co-expressing
230 neuronal $mHTT_{ex1}$ compared with controls expressing $wtHTT_{ex1}$ (Fig. 1C). This effect could be observed
231 as early as 1 day post-injury, suggesting that $mHTT_{ex1}$ causes defects in both clearance and
232 engulfment of axonal debris. Delayed clearance of axonal debris was exacerbated in older (14 and 28
233 day-old) $mHTT_{ex1}$-expressing flies (Fig. 1C), possibly related to a decline in Draper activity during
234 normal aging (Purice et al., 2016) and/or enhanced glial dysfunction compounded by $mHTT_{ex1}$
235 aggregate accumulation. Quantification of mCherry fluorescence indicated that clearance of axonal
236 $mHTT_{ex1}$ was also slowed compared to $wtHTT_{ex1}$ (Fig. 1D), suggesting that glia are deficient in
237 degrading both axonal debris and neuronal $mHTT_{ex1}$ aggregates.
238 We also tested whether formation of $mHTT_{ex1}$ aggregates in glial cells impacts ORN axonal
239 debris clearance following acute injury. Restricting expression of $mHTT_{ex1}$ to glia resulted in
240 appearance of heterogeneously-sized $mHTT_{ex1}$ aggregates throughout the brain (Fig. 2A). Glial
241 $mHTT_{ex1}$ aggregates also slowed injury-induced clearance of mCD8-GFP-labeled axons compared with
242 $wtHTT_{ex1}$-expressing controls (Fig. 2B-D), though glial $mHTT_{ex1}$ expression did not affect DA1 ORN
243 axon abundance in 1 day-old flies (Fig. 2E). Together, these findings indicate that $mHTT_{ex1}$ aggregates
244 originating in either neurons or glia slow efficient clearance of injured ORN axons by phagocytic glia.
245
246 *Neuronal mHTT aggregates impair nascent phagosome formation*
247 Phagocytosis occurs via 4 major steps: (1) extension of phagocyte membranes toward
248 extracellular “find me” cues, (2) recognition of “eat me” signals by scavenger receptors, (3) cytoskeletal
249 and plasma membrane reorganization to surround and internalize extracellular material, and (4)
250 maturation of nascent phagosomes through sequential endomembrane fusions that culminate at the
251 lysosome (Vieira et al., 2002). We have previously reported that the conserved scavenger receptor,
252 Draper/Ced-1/MEGF10 (MacDonald et al., 2006; Evans et al., 2015; Iram et al., 2016), regulates
253 engulfment, clearance, and intercellular spreading of $mHTT_{ex1}$ aggregates originating in ORN axons
254 (Pearce et al., 2015; Donnelly et al., 2020). To determine whether delayed clearance of injured axons
255 containing $mHTT_{ex1}$ aggregates (Fig. 1C and 2D) could result from defective Draper-dependent

256 engulfment, we co-expressed V5-tagged $mHTT_{ex1}$ or $wtHTT_{ex1}$ with the ratiometric membrane-
257 associated pH sensor (MApHS), consisting of the transmembrane domain of CD4 flanked by N-terminal
258 ecliptic pHluorin and C-terminal tdTomato (Han et al., 2014), in the VA1lm type of ORNs. Ecliptic
259 pHluorin is brightest at pH 7.5 and dims as pH drops, quenching at pH <6.0 (Miesenböck et al., 1998),
260 whereas tdTomato fluorescence is pH resistant. Thus, internalization of MApHS-labeled ORN axonal
261 debris into a rapidly-acidified nascent phagosome can be monitored by calculating pHluorin:tdTomato
262 fluorescence intensity ratios (Han et al., 2014). Indeed, pHluorin:tdTomato ratios in VA1lm axons were
263 decreased at 14 and 25 hours post-axotomy (Fig. 3A-C), and this effect was lost when *draper* was
264 deleted from glia using the tissue-specific CRISPR/Cas9-TriM method (Fig. 3C and E-G) (Poe et al.,
265 2019), demonstrating that this construct accurately reports nascent phagosome acidification following
266 engulfment. Notably, the decrease in pHluorin:tdTomato ratio following injury was less pronounced in
267 VA1lm ORN axons co-expressing $mHTT_{ex1}$ compared with $wtHTT_{ex1}$-expressing controls (Fig. 3A-C),
268 suggesting that $mHTT_{ex1}$ aggregates impair nascent phagosome formation following engulfment.
269
270 *Neuronal mHTT accumulates in low pH intracellular compartments*
271 $mHTT_{ex1}$ expression was associated with a slight but significant decrease in steady-state
272 pHluorin:tdTomato ratios in MApHS-labeled axons compared with $wtHTT_{ex1}$-expressing controls (Fig.
273 3D), suggesting that even in the absence of acute injury, $mHTT_{ex1}$ signals for ORN axon engulfment. To
274 test this, we generated transgenic flies that express $mHTT_{ex1}$ or $wtHTT_{ex1}$ fused to N-terminal pHluorin
275 and C-terminal tdTomato fluorescent proteins, herein referred to as mHTT-associated pH sensor
276 (mHApHS) or wtHTT-associated pH sensor (wtHApHS). Accumulation of HTT_{ex1} protein in low pH
277 cellular compartments would cause a decrease in the ratio of pHluorin:tdTomato fluorescence for these
278 constructs. wtHApHS and mHApHS transgenes were expressed in either Or83b+ ORNs, which
279 encompass 70-80% of all adult ORNs (Fig. 4A-B) (Larsson et al., 2004), or mushroom body neurons
280 (MBNs; Fig. 4D-E), which are downstream in the fly olfactory circuit and innervate the learning and
281 memory center of the fly CNS (McGuire et al., 2001). In both ORN axons and MBN soma,
282 pHluorin:tdTomato ratios associated with mHApHS were significantly decreased compared with

283 wtHApHS controls (Fig. 4C and F), suggesting that $mHTT_{ex1}$ proteins accumulate in acidified cellular
284 compartments. To discriminate $mHTT_{ex1}$ proteins engulfed by glia from $mHTT_{ex1}$ internalized into
285 neuronal autophagolysosomes, we measured VA1lm ORN axonal mHApHS-associated fluorescence in
286 animals with glial *draper* loss-of-function (Fig. 4G-H). Glial *draper* knockout increased
287 pHluorin:tdTomato ratios for axonal mHApHS (Fig. 4I), suggesting that at least some portion of
288 $mHTT_{ex1}$ aggregates accumulate in acidic portions of the glial phagolysosomal system.
289
290 *Neuronal mHTT impairs injury-responsive gene upregulation*
291 Glia alter their transcriptional profile to elicit cellular responses to insult or injury in the brain. For
292 example, acute CNS injury in *Drosophila* increases transcription of many genes involved in
293 phagocytosis and innate immunity, including the cell surface receptors, Draper and Toll-6, and
294 components of their downstream signaling pathways (Fig. 5A) (Purice et al., 2017; Byrns et al., 2021;
295 Alphen et al., 2022). To test whether the reduced ability of glia to clear $mHTT_{ex1}$ -containing axonal
296 debris correlates with reduced injury responsiveness at a transcriptional level, we used qPCR and
297 GFP-tagged reporters to quantify changes in gene expression of key components of these phagocytic
298 and innate immunity pathways following $mHTT_{ex1}$ accumulation in neurons. $mHTT_{ex1}$ expression in
299 uninjured Or83b+ ORNs increased relative expression of *toll-6, relish*, and *drpr-I* transcripts between
300 1.2- and 1.5-fold (Fig. 5B) and levels of GFP-tagged Toll-6 and Jra proteins in the CNS (Fig. 5C-H),
301 suggesting that neuronal $mHTT_{ex1}$ aggregates activate a mild injury response in the brain. Jra-GFP
302 expression increased throughout the CNS and in Repo+ nuclei (Fig. 5F-H), suggesting that $mHTT_{ex1}$-
303 induced upregulation of this subunit of the AP-1 transcription factor can be at least partially attributed to
304 glia. To test whether $mHTT_{ex1}$ impairs the ability of glia to respond to acute neural injury, we monitored
305 gene expression changes after bilateral antennal and maxillary palp nerve ablation. Similar to previous
306 reports (Purice et al., 2017), expression of *toll-6, dorsal, relish, drpr-I*, *mmp1,* and *ets21c* genes was
307 significantly increased 3 hrs after injury to ORN axons expressing either mCD8-GFP or $wtHTT_{ex1}$ (Fig.
308 5B). However, injury-induced upregulation of each of these genes was significantly reduced in animals
309 expressing $mHTT_{ex1}$ in Or83b+ ORNs (Fig. 5B), suggesting that $mHTT_{ex1}$ aggregation attenuates glial

310 transcriptional responses to injury. We further analyzed the impact of $mHTT_{ex1}$ on downstream immune
311 responses in the brain by measuring induction of antimicrobial peptide (AMP) genes, well-established
312 transcriptional targets of activated Relish/NFκB following Toll-6 or immune-deficiency pathway
313 activation (Swanson et al., 2020b, 2020a; Alphen et al., 2022). Levels of five AMP genes, including
314 *drosomycin*, *attacinA*, *attacinD*, *diptericinA*, and *metchnikowin*, were significantly increased 3 hours
315 after ORN axotomy (Fig. 6A-E), similar to previous reports (Katzenberger et al., 2013; Swanson et al.,
316 2020b; Marischuk et al., 2021). Interestingly, $mHTT_{ex1}$ expression in ORNs alone was sufficient to
317 induce upregulation of *drosomycin* and *attacinD* (Fig. 6A & C), albeit to a lesser extent than following
318 acute injury. Further, injury-induced upregulation of *drosomycin* and *attacinA* was significantly reduced
319 by $mHTT_{ex1}$ expression in ORNs, suggesting that the activity of Relish-dependent signaling is altered by
320 accumulation of $mHTT_{ex1}$ aggregates. Together, these data indicate that neuronal $mHTT_{ex1}$ aggregates
321 trigger a mild immune response in the brain, but also inhibit the ability of glia to mount robust
322 transcriptional responses to neural injury.

323 Our findings are in agreement with previously published work demonstrating that expression of
324 $mHTT_{ex1}$ and Aβ in neurons activates Draper-dependent phagocytosis, likely in an effort to reduce
325 levels of these pathogenic proteins in the brain (Pearce et al., 2015; Ray et al., 2017). We further
326 investigated this by immunostaining adult fly brains expressing $mHTT_{ex1}$ in ORNs to monitor expression
327 levels and localization of endogenous Draper protein. In 1 week-old adult flies expressing neuronal
328 $mHTT_{ex1}$, Draper immunolabeling increased ~1.2-fold in the vicinity of ORN axons compared with age-
329 matched controls expressing $wtHTT_{ex1}$ (Fig. 7A-C). Closer analysis revealed that in some cases,
330 Draper immunofluorescence was directly adjacent to or surrounding $mHTT_{ex1}$-mCherry fluorescence
331 (Fig. 7D). To further examine these interactions, we used image segmentation and three-dimensional
332 reconstruction of confocal stacks to represent $mHTT_{ex1}$-mCherry+ aggregates and Draper+ glial
333 membranes as individual "surfaces" (Fig. 7E-F), as previously described (Donnelly et al., 2020). Close
334 physical association of $mHTT_{ex1}$ with Draper and other glial proteins was defined as surfaces located
335 ≤0.2 μm from a $mHTT_{ex1}$ object. Interestingly, whereas almost no Draper signal was detected near
336 $wtHTT_{ex1}$ (Fig. 7E), ~14% of $mHTT_{ex1}$ aggregates were closely associated with Draper surfaces (Fig.

337 7F1-3). These findings are consistent with Draper+ glial membranes being recruited to neuronal
338 $mHTT_{ex1}$ aggregates to facilitate engulfment.
339 Synaptic neuropil in the *Drosophila* brain is primarily inhabited by two glial subtypes,
340 ensheathing glia and astrocytic glia (Doherty et al., 2009). In adult flies, ensheathing glia
341 compartmentalize synaptic regions and respond to CNS injury by upregulating Draper and clearing
342 debris via phagocytosis (Doherty et al., 2009). Consistent with our previous findings in all repo+ glia
343 (Pearce et al., 2015), mz0709+ ensheathing glia were vulnerable to prion-like conversion of glial
344 $wtHTT_{ex1}$ proteins by $mHTT_{ex1}$ aggregates generated in DA1 ORN axons (Fig. 8A, C-D). Seeded
345 $wtHTT_{ex1}$ aggregates were defined as $wtHTT_{ex1}$ signal that colocalized with $mHTT_{ex1}$ objects identified
346 by image segmentation of confocal stacks (Donnelly et al., 2020). Conversely, seeding of $wtHTT_{ex1}$
347 expressed in alrm+ astrocytic glia, which lack detectable Draper expression in the adult fly brain
348 (Doherty et al., 2009), was not observed (Fig. 8B-D). Interestingly, ensheathing glial-specific RNAi
349 knockdown of Toll-6, Relish, and NijA increased $mHTT_{ex1}$ aggregate numbers in DA1 ORN axons,
350 similar to the effects of Draper-I knockdown (Fig. 9A-B). Further, adult-specific, pan-glial knockdown of
351 Ets21c, which was found to be required for normal development, also increased numbers of $mHTT_{ex1}$
352 aggregates in DA1 ORN axons (Fig. 9C-D). Mean $mHTT_{ex1}$ aggregate volume was not affected by
353 ensheathing glial knockdown of these genes except for a ~20% increase following NijA depletion (Fig.
354 9E), suggesting that aggregate or vesicle size was unaffected by these genetic manipulations. Thus,
355 several glial genes with established roles in phagocytic and innate immune signaling regulate basal
356 turnover of $mHTT_{ex1}$ aggregates in ORN axons.
357
358 *Neuronal mHTT aggregates are associated with defects in multiple endolysosomal compartments*
359 Our findings thus far indicate that neuronal $mHTT_{ex1}$ aggregates elicit mild injury responses in
360 the brain and reduce the ability of phagocytic glia to respond transcriptionally and functionally to acute
361 nerve injury. We have previously postulated that prion-like spreading of $mHTT_{ex1}$ in the fly CNS could
362 be facilitated by escape of engulfed aggregates from the endolysosomal compartment of phagocytic
363 glia (Pearce et al., 2015; Donnelly et al., 2020). Therefore, we sought to determine whether neuronal

364 $mHTT_{ex1}$ aggregates are associated with defects in endolysosomal processing in non-injured brains.
365 We first measured effects of neuronal $mHTT_{ex1}$ expression on the quantity, size, and function of
366 lysosomes using dyes that label active cathepsins and low pH cellular compartments. Expression of
367 $mHTT_{ex1}$ in Or83b+ ORNs increased numbers of lysosomes labeled by the active cathepsin dye, Magic
368 Red (MR) (Fig. 10A-C), and the low pH sensor, LysoTracker Red (LTR) (Fig. 10D-F), compared with
369 control brains expressing $wtHTT_{ex1}$. High resolution analysis of confocal stacks and filtering for
370 segmented MR+ and LTR+ surfaces within 0.2 μm of a $mHTT_{ex1}$ object revealed close association of
371 MR+ and LTR+ signals with $mHTT_{ex1}$ aggregates (Fig. 10C and F-H).

372 We next employed *Drosophila* genetic tools to assess the impact of neuronal $mHTT_{ex1}$
373 specifically on glial lysosomes by driving expression of lysosomal-associated membrane protein 1
374 (LAMP1) tagged at its cytosolic C-terminus with GFP (LAMP1-GFP) in all glia. Neuronal $mHTT_{ex1}$
375 expression increased the overall number of glial LAMP1-GFP+ vesicles and the number of LAMP1-
376 GFP+ vesicles in close proximity to HTT_{ex1} signal (Fig. 11A-C and G-H). We typically observed only
377 partial overlap of LAMP1-GFP signal with $mHTT_{ex1}$ aggregate surfaces identified by this method,
378 possibly due to incomplete labeling or rupture of lysosomal membranes as a result of aggregate size or
379 structural features. Interestingly, this subpopulation of LAMP1-GFP+ lysosomes closely associated with
380 $mHTT_{ex1}$ were enlarged compared with all lysosomes (Fig. 11I). To examine whether neuronal $mHTT_{ex1}$
381 aggregates affect lysosome integrity, we expressed a transgene encoding LAMP1 fused at its N-
382 terminus to GFP in glia. This construct integrates into the lysosomal membrane such that GFP is
383 exposed to the lumen, and loss of GFP signal can thus be used to monitor LAMP1+ lysosome
384 degradative activity (Pulipparacharuvil et al., 2005). Interestingly, the quantity and mean volume of
385 GFP-LAMP1+ vesicles were significantly increased in brains expressing $mHTT_{ex1}$ in Or83b+ ORNs
386 (Fig. 11D-G), suggesting lysosomal enlargement and dysfunction due to $mHTT_{ex1}$ aggregates. GFP-
387 LAMP1+ surfaces were also more associated with $mHTT_{ex1}$ aggregates compared to $wtHTT_{ex1}$ controls
388 (Fig. 11F and I).

389 To directly test whether glial endolysosomes experience increased membrane damage due to
390 neuronal $mHTT_{ex1}$ expression, we generated transgenic flies expressing mCherry-tagged Galectin-3 or

391 Galectin-8, lectins that translocate from the cytoplasm to the lumen of ruptured lysosomes and
392 endosomes, respectively (Aits et al., 2015; Daussy and Wodrich, 2020; Jia et al., 2020). Neuronal
393 $mHTT_{ex1}$ expression increased overall numbers of glial Galectin-3/8+ surfaces (Fig. 12A-E), Galectin-
394 3/8+ surfaces closely associated with $mHTT_{ex1}$ aggregates (Fig. 12F), and mean volume of $mHTT_{ex1}$-
395 associated Galectin-3/8+ vesicles (Fig. 12G). Together, these data suggest that neuronal $mHTT_{ex1}$
396 aggregates induce non cell-autonomous accumulation, enlargement, and membrane damage of
397 endolysosome vesicles in glial cells.
398 "Seeding-competent" mHTT aggregates are defined by their ability to nucleate or "seed" the
399 aggregation of normally-soluble wtHTT proteins, a defining characteristic of infectious prion and other
400 prion-like proteins (Jucker and Walker, 2018; Donnelly et al., 2022). Many studies have pointed to a
401 role for defective clearance by endolysosomal pathways in promoting the propagation of pathogenic
402 aggregates (Freeman et al., 2013; Jiang et al., 2017; Chen et al., 2019; Jiang and Bhaskar, 2020;
403 Polanco and Götz, 2022). To test whether altered glial lysosome function affects seeding competency
404 of $mHTT_{ex1}$, we used RNAi to individually knockdown proteins with known roles in lysosome
405 degradation in glia and examined the ability of neuronal mCherry-tagged $mHTT_{ex1}$ to seed aggregation
406 of glial, GFP-tagged $wtHTT_{ex1}$. Depletion of two subunits of the vacuolar ATPase (V-ATPase), Vha68-3
407 (Portela et al., 2018) and rabconnectin-3A (Yan et al., 2009), and Spinster, a late-endosomal and
408 lysosomal efflux permease (Rong et al., 2011), increased numbers of glial $wtHTT_{ex1}$ aggregates
409 detected as GFP+ surfaces that colocalized with $mHTT_{ex1}$ aggregates (Fig. 13A-C) (Donnelly et al.,
410 2020). Knockdown of Vha16-1, a V-ATPase subunit that regulates endolysosome membrane fusion
411 (Finbow et al., 1994; Dunlop et al., 1995), did not affect $wtHTT_{ex1}$ seeding; however, it did cause
412 accumulation of $mHTT_{ex1}$ aggregates in DA1 ORN axons (Fig. 13A and B). Together, these findings
413 suggest that disruption of normal glial lysosome acidification and/or degradative capacity promotes
414 formation of seeding-competent $mHTT_{ex1}$ aggregates.
415
416 *The GTPase Rab10 mediates prion-like transmission of mHTT aggregates*

417 Lysosome dysfunction could occur secondary to upstream defects in endo/phagosome
418 maturation. Our prior work supports a model in which a portion of $mHTT_{ex1}$ aggregates engulfed by glia
419 evade degradation during phagosome maturation and/or phagolysosome formation (Pearce et al.,
420 2015; Donnelly et al., 2020). To test this model, we used forward genetic screening to interrogate roles
421 for glial Rab GTPases in prion-like conversion of cytoplasmic $wtHTT_{ex1}$ proteins by engulfed neuronal
422 $mHTT_{ex1}$ aggregates. The *Drosophila* genome encodes 31 Rab and Rab-like proteins, all of which have
423 mammalian orthologs, and most of these GTPases are implicated in vesicle and target membrane
424 fusion in cells (Zhang et al., 2007). To determine whether any *Drosophila* Rabs mediate escape of
425 phagocytosed $mHTT_{ex1}$ aggregates and seeding of $wtHTT_{ex1}$ in the glial cytoplasm, we individually
426 knocked down each Rab in repo+ glia using RNAi. Glial-restricted silencing of 23 of the 31 Rabs
427 produced viable adults, and these flies were used to monitor effects of Rab knockdown on $mHTT_{ex1}$-
428 induced aggregation of $wtHTT_{ex1}$ in glia. Only two Rab RNAi lines, $Rab10^{RNAi}$ and $Rab23^{RNAi\#2}$,
429 significantly altered numbers of induced $wtHTT_{ex1}$ aggregates (Fig. 14A-C). Of note, 3 additional Rab23
430 RNAi lines had no significant effects on numbers of $wtHTT_{ex1}$ aggregates, suggesting that $Rab23^{RNAi\#2}$
431 may cause off-target effects. Strikingly, Rab10 depletion reduced numbers of seeded $wtHTT_{ex1}$
432 aggregates, phenocopying effects of Draper knockdown (Fig. 14A and C) and suggesting that Draper
433 and Rab10 function in the same pathway. To test whether this effect of Rab10 loss-of-function was
434 mediated via a reduction in Draper expression, we measured endogenous Draper immunofluorescence
435 in *rab10* null flies. Draper protein levels were ~18% lower in $rab10^{-/-}$ animals compared to wild-type
436 controls (Fig. 14D). This reduction is unlikely to fully account for decreased seeding of $wtHTT_{ex1}$
437 following Rab10 knockdown, as numbers of $wtHTT_{ex1}$ aggregates are similar between wild-type and
438 *draper* heterozygotes (Fig. 14G) (Pearce et al., 2015). To further explore this, we attempted to restore
439 Draper function via overexpression of Draper-I, which rescues loss of Draper function in aged flies
440 (Purice et al., 2016). However, transgenic expression of Draper-I in glia failed to rescue the effects of
441 Rab10 knockdown on $wtHTT_{ex1}$ aggregate seeding (Fig. 14E). These findings suggest that Rab10 acts
442 downstream of Draper rather than by regulating Draper activity. We further tested for interactions
443 between *drpr* and *rab10* using loss-of-function alleles to examine effects on $mHTT_{ex1}$ aggregate

transmission from presynaptic DA1 ORNs to postsynaptic projection neurons (PNs), a process previously reported to require transport though Draper+ glia (Donnelly et al., 2020). Because reduced survival of *rab10* null flies (Kohrs et al., 2021) was exacerbated by transgenic HTT_{ex1} expression, we tested for genetic interaction between *drpr* and *rab10* in heterozygous and trans-heterozygous animals. While we detected no change in $mHTT_{ex1}$ aggregate numbers (Fig. 14F), significantly fewer $wtHTT_{ex1}$ aggregates formed in PNs of *rab10*$^{+/-}$ *drpr*$^{+/-}$ transheterozygotes than in individual heterozygotes (Fig. 14G). This same effect was not observed in *rab14*$^{+/-}$ *drpr*$^{+/-}$ transheterozygous animals (Fig. 14G), indicating that the genetic interaction is specific to *drpr* and *rab10*. Thus, Draper and Rab10 appear to function in the same phagocytic pathway that regulates prion-like transmission of phagocytosed $mHTT_{ex1}$ aggregates in the fly brain.

Neuronal mHTT aggregates alter numbers of early and late glial phagosomes

Our forward genetic screen indicates that at least one glial Rab GTPase, Rab10, regulates the seeding capacity of neuronal $mHTT_{ex1}$ aggregates. Interestingly, Rab10 has been reported to regulate phagosome maturation in mammalian cells (Cardoso et al., 2010; Seto et al., 2011; Lee et al., 2020; Wang et al., 2023), and Rab10 expression and activity are altered in neurodegenerative diseases, including AD and PD (Eguchi et al., 2018; Tavana et al., 2018; Yan et al., 2018). Because little is known about Rab10's role in glia, we sought to characterize this GTPase alongside two additional Rabs with well-established roles in endocytosis, Rab5 and Rab7, markers of early and late endo/phagosomes, respectively (Hutagalung and Novick, 2011). Interestingly, we found that *rab10*, *rab5*, and *rab7* were upregulated between ~1.4 and 2.4-fold following acute injury to ORN axons, and $mHTT_{ex1}$ expression in Or83b+ ORNs alone caused upregulation of *rab10* and *rab7* genes by ~1.2-fold (Fig. 15A). Interestingly, injury-induced upregulation of *rab5* and *rab7* was inhibited by ~50% and ~100%, respectively, in flies expressing $mHTT_{ex1}$ compared to controls (Fig. 15A). Altogether, these results identify *rab5*, *rab7*, and *rab10* as novel injury-response genes in the fly CNS and suggest that neuronal $mHTT_{ex1}$ aggregates impair injury-induced responses of *rab5* and *rab7*.

470 We next examined effects of neuronal $mHTT_{ex1}$ expression on the localization of Rab10, Rab5,
471 and Rab7 proteins endogenously-tagged with YFP-myc at their N-termini, herein referred to as
472 YRab10, YRab5, and YRab7 (Dunst et al., 2015). YRab+ vesicles were identified in confocal stacks as
473 segmented YFP+ surfaces with a mean diameter of 0.3-8 μm (Fig. 15B-G), consistent with vesicle sizes
474 reported in other fly tissues (Prince et al., 2019). Expression of $mHTT_{ex1}$ in Or83b+ ORN axons caused
475 an overall increase in numbers of YRab10+ and YRab7+ vesicles, but a decrease in the number of
476 YRab5+ vesicles compared with $wtHTT_{ex1}$ controls (Fig. 15H). Further, each of these YRab+ vesicles
477 subpopulations were closely associated with $mHTT_{ex1}$ aggregates more frequently than with $wtHTT_{ex1}$
478 (Fig. 15I), suggesting that $mHTT_{ex1}$ protein interacts with each of these intracellular vesicle
479 subpopulations in the brain.

480 To assess effects of neuronal $mHTT_{ex1}$ aggregates specifically on glial Rab+ compartments, we
481 expressed YFP-tagged Rab5, 7, and 10 transgenes in all glia. Similar to our findings with endogenous
482 YRabs, expression of $mHTT_{ex1}$ in Or83b+ ORN axons was associated with increased numbers of glial
483 YFP-Rab10+ and -Rab7+ vesicles (Fig. 16A-B, E-F, and G); however, we observed a significant
484 decrease in glial YFP-Rab5+ vesicle abundance (Fig. 16C-D and G). YFP-Rab10+, -5+, and -7+
485 vesicles increased their association with axonal $mHTT_{ex1}$ aggregates compared with $wtHTT_{ex1}$ (Fig.
486 16H), in many cases with closely associated YFP-Rab+ signal partially surrounding a $mHTT_{ex1}$
487 aggregate (Fig. 17). Of note, only a small fraction of YFP-Rab+ vesicles were identified as associated
488 with $mHTT_{ex1}$ aggregates, possibly due to transient interactions with vesicle compartments as
489 aggregates transit the glial phagolysosomal system, heterogeneous labeling of phagosomes by these
490 markers in intact brain tissue, or because our selection filter excluded YFP-Rab+ surfaces located >0.2
491 μm away from an aggregate. The mean volume of YFP-Rab7+ vesicles that interacted with $mHTT_{ex1}$
492 aggregates was significantly increased compared with $wtHTT_{ex1}$ controls (Fig. 16I), suggesting that
493 $mHTT_{ex1}$ leads to enlargement of Rab7+ late phagolysosomes. Together, these data suggest that
494 accumulation of phagocytosed $mHTT_{ex1}$ aggregates in Rab7+ or Rab10+ late phagosomes and
495 decreased association with early Rab5+ phagosomes could be a key mechanism underlying protein
496 aggregate-induced toxicity and spreading in HD.

497 **DISCUSSION**

498 Toxic amyloid aggregates have been a primary target in neurodegenerative disease drug
499 development for decades, with some recent promise using immunotherapy to reduce aggregate loads
500 in the brain (Karran and De Strooper, 2022). Microglia and astrocytes have also emerged as attractive
501 therapeutic targets in efforts to boost neuroprotective glial functions or reduce neuroinflammation.
502 However, approaches that target glial cells must effectively strike a balance between amplifying
503 beneficial and reducing harmful effects of these cells in the brain. Here, we tested for interactions
504 between phagocytic glia and pathogenic protein aggregates in a *Drosophila* model of HD. We report
505 that aggregates formed by $mHTT_{ex1}$ protein fragments impair glial transcriptional and functional
506 responses to CNS injury, induce upregulation of stress response and innate immunity genes, and alter
507 numbers of endolysosomal vesicles detected in uninjured brains. A targeted forward genetic screen
508 revealed that Rab10, a GTPase previously reported to regulate phagosome maturation, mediates prion-
509 like conversion of cytoplasmic $wtHTT_{ex1}$ proteins by phagocytosed $mHTT_{ex1}$ aggregates. Together,
510 these findings suggest that neuronal $mHTT_{ex1}$ aggregates compromise intracellular membrane integrity
511 as they transit endolysosomal systems, generating toxic, seeding-competent aggregates that propagate
512 disease phenotypes.

513 Glia respond to neural injury by altering their transcriptional, morphological, and metabolic
514 profiles to promote neuronal survival and clear debris from the brain; however, failure of glia to return to
515 a resting state elicits harmful neuroinflammatory consequences (Liddelow et al., 2020). We have
516 previously reported that activated phagocytic glia can have both beneficial (i.e., elimination of toxic
517 aggregates) and harmful (i.e., as vectors for aggregate spread) effects in the brain (Pearce et al., 2015;
518 Donnelly et al., 2020). We report here that key glial injury-responsive pathways, i.e., Draper-mediated
519 phagocytosis and Toll-6-mediated innate immune signaling, are induced in the presence $mHTT_{ex1}$
520 aggregation in the adult fly brain. These findings are in line with studies from other labs demonstrating
521 that *Drosophila* Toll-6 and mammalian Toll-Like Receptor signaling pathways are upregulated in
522 response to dying neurons during development (McLaughlin et al., 2019) and in patient and mammalian
523 models of neurodegenerative disease (Casula et al., 2011; Miron et al., 2018; Kouli et al., 2020).

524 Interestingly, increased microglial NF-κB signaling mediates tau spread and toxicity in mice, further
525 linking innate immunity to prion-like mechanisms of disease progression (Wang et al., 2022). Thus,
526 activation of glial immune pathways may contribute to feed-forward mechanisms involving aggregate
527 formation, pathology propagation, and neuroinflammatory signaling.

528 Genome-wide association studies have revealed numerous genes associated with increased
529 risk of AD and other neurodegenerative diseases, and many of these risk variants are enriched in
530 pathways that control key glial cell functions. For example, rare risk-associated variants of the
531 microglial *TREM2* gene alter amyloid aggregate accumulation and seeding in cells and animal models
532 (Leyns et al., 2019; Parhizkar et al., 2019; Jain et al., 2023). A number of additional genes involved in
533 endolysosomal processing are associated with increased risk of AD, PD, FTD, and/or ALS, such as the
534 phagocytic receptor *CD33*, endosomal genes *BIN1* and *RIN3*, and *GRN*, which encodes the lysosomal
535 progranulin protein (Podleśny-Drabiniok et al., 2020; Welikovitch et al., 2023). Although
536 Draper/MEGF10 variants are not known risk factors in neurodegenerative disease, MEGF10 is highly
537 expressed in phagocytic astrocytes (Chung et al., 2013), mediates Aβ aggregate engulfment (Singh et
538 al., 2010; Fujita et al., 2020), and acts as a receptor for C1q, a mediator of early synapse loss in AD
539 mouse models (Hong et al., 2016; Iram et al., 2016). Our finding that upregulation of *draper* and other
540 phagocytic genes is inhibited by $mHTT_{ex1}$ expression suggests that glial responsiveness and
541 phagocytic capacity is attenuated in the presence of protein aggregate pathology in neurons. Genetic or
542 environmental risk factors that impact glial health could accelerate these defects and exacerbate
543 aggregate-induced neurotoxicity in the brain.

544 Lysosomes are essential for cell survival, not only to clear damaged or toxic materials from
545 cells, but also as intracellular centers for macromolecule recycling, energy metabolism, and cell-cell
546 communication. Lysosomal abnormalities, including vesicle enlargement, deacidification, and
547 membrane leakiness, have been reported in patient brains and animal and cell models of multiple
548 neurodegenerative diseases, suggesting that these defects play a central role in disease progression
549 (Bonam et al., 2019; Polanco and Götz, 2022; Udayar et al., 2022). We report here that Rab7+,
550 Rab10+, and Lamp1+ phagolysosomes accumulate in glia as a result of $mHTT_{ex1}$ expression in

551 neurons and that lysosome dysfunction and membrane permeabilization increase in the presence of
552 $mHTT_{ex1}$ aggregates. We also observed that neuronal aggregates were associated with decreased
553 nascent phagosome formation and reduced numbers of early (Rab5+) phagosomes in glia. These
554 findings are consistent with a "traffic jam" model (Small et al., 2017) in which $mHTT_{ex1}$ aggregates
555 accumulate over time in glial endolysosomal compartments, preventing proper flow of materials into
556 (i.e., engulfment) and out of (i.e., degradation) the pathway (Fig. 18). We postulate that persistence of
557 aggregates in faulty endolysosomes promotes formation and/or release of degradation-resistant
558 aggregates with enhanced toxicity and seeding capacity. This hypothesis is in agreement with recent
559 studies in tauopathy models showing that Aβ aggregation occurs secondary to lysosome deacidification
560 and membrane permeabilization (Lee et al., 2022), and hypophagocytic glia contribute to tau aggregate
561 propagation (Hopp et al., 2018; Brelstaff et al., 2021). Release of seeding-competent aggregates from
562 dysfunctional lysosomes could occur via active exocytosis, perhaps in an effort to alleviate cell toxicity,
563 or passively due to vesicle rupture (Flavin et al., 2017; Falcon et al., 2018; Yuste-Checa et al., 2021).
564 Among the growing list of genes linked to neurodegenerative disease pathogenesis are Rab
565 GTPases and genes that modify Rab functions (Kiral et al., 2018). Rab proteins are essential for vesicle
566 sorting and trafficking in all cells and use GTP hydrolysis to differentially associate with and organize
567 intracellular membranes (Homma et al., 2021). In a forward genetic screen aimed at identifying Rabs
568 that regulate phagocytic processing of neuronal $mHTT_{ex1}$ aggregates, we uncovered glial Rab10 as a
569 modifier of prion-like spreading of $mHTT_{ex1}$ from neurons to glia. Interestingly, several Rab proteins
570 have been previously reported to alter secretion or cell-to-cell propagation of tau or α-synuclein
571 aggregates (Rodriguez et al., 2017; Bae et al., 2018; Ugbode et al., 2019; Rodrigues et al., 2022),
572 suggesting that Rab-dependent endomembrane fusion could be exploited by prion-like aggregates. Our
573 data suggest that Rab10 acts downstream of Draper to enable engulfed $mHTT_{ex1}$ aggregates to evade
574 lysosomal degradation, perhaps escaping to the cytoplasm during Rab10-dependent vesicle fusion.
575 While relatively understudied compared with other Rabs, Rab10 has been reported to localize to and
576 regulate maturing endo/phagosomes and lysosomes in human macrophages and microglia (Cardoso et
577 al., 2010; Lee et al., 2020). Interestingly, Rab10 has already been implicated in multiple

578 neurodegenerative diseases: (1) *RAB10* gene expression is altered in human AD brains (Ridge et al.,
579 2017), (2) rare *RAB10* polymorphisms are linked to protection against AD (Ridge et al., 2017; Tavana
580 et al., 2018), (3) Rab10 depletion is associated with reduced Aβ levels (Udayar et al., 2013; Ridge et
581 al., 2017), and (4) Rab10 is a substrate of the PD risk factor gene leucine-rich repeat kinase 2 (LRRK2)
582 (Steger et al., 2016; Seol et al., 2019). Mutant LRRK2-mediated Rab phosphorylation leads to
583 endocytic defects (Liu et al., 2020; Rivero-Ríos et al., 2020; Streubel-Gallasch et al., 2021), and
584 LRRK2-modified Rab10 localizes to and promotes secretion from stressed lysosomes (Eguchi et al.,
585 2018; Kluss et al., 2022). Interestingly, phosphorylated Rab10 (pRab10) levels are elevated in the CNS
586 of AD and PD patients, and pRab10 has been reported to colocalize with pathological tau (Yan et al.,
587 2018; Tezuka et al., 2022) suggesting that post-translational modification of Rab10 modifies the
588 disease state. Whether Rab10's phosphorylation status affects its ability to regulate prion-like activity of
589 $mHTT_{ex1}$ or other amyloid aggregates warrants further investigation.

590 In conclusion, our findings demonstrate that axonal $mHTT_{ex1}$ aggregates activate glial
591 phagocytosis but also impair normal glial responses to acute neural injury. Aggregate engulfment-
592 induced defects in endolysosomal processing, such as Rab-mediated vesicle membrane fusion, could
593 facilitate the formation and spread of prion-like aggregate seeds in the brain. These findings point to
594 central roles for phagocytic glia in regulating pathological aggregate burden in HD and highlight the
595 importance of exploring therapeutic interventions that target non-neuronal cells.

596 **REFERENCES**

597 Aits, S., Kricker, J., Liu, B., Ellegaard, A.-M., Hämälistö, S., Tvingsholm, S., et al. (2015). Sensitive
598 detection of lysosomal membrane permeabilization by lysosomal galectin puncta assay.
599 *Autophagy* 11, 1408–1424. doi: 10.1080/15548627.2015.1063871

600 Alphen, B. van, Stewart, S., Iwanaszko, M., Xu, F., Li, K., Rozenfeld, S., et al. (2022). Glial immune-
601 related pathways mediate effects of closed head traumatic brain injury on behavior and lethality
602 in Drosophila. *PLOS Biology* 20, e3001456. doi: 10.1371/journal.pbio.3001456

603 Aman, Y., Schmauck-Medina, T., Hansen, M., Morimoto, R. I., Simon, A. K., Bjedov, I., et al. (2021).
604 Autophagy in healthy aging and disease. *Nat Aging* 1, 634–650. doi: 10.1038/s43587-021-
605 00098-4

606 Bae, E.-J., Kim, D.-K., Kim, C., Mante, M., Adame, A., Rockenstein, E., et al. (2018). LRRK2 kinase
607 regulates α-synuclein propagation via RAB35 phosphorylation. *Nat Commun* 9, 3465. doi:
608 10.1038/s41467-018-05958-z

609 Bonam, S. R., Wang, F., and Muller, S. (2019). Lysosomes as a therapeutic target. *Nat Rev Drug*
610 *Discov* 18, 923–948. doi: 10.1038/s41573-019-0036-1

611 Brand, A. H., and Perrimon, N. (1993). Targeted gene expression as a means of altering cell fates and
612 generating dominant phenotypes | Development | The Company of Biologists. Available at:
613 https://journals.biologists.com/dev/article/118/2/401/37970/Targeted-gene-expression-as-a-
614 means-of-altering (Accessed September 19, 2022).

615 Brelstaff, J. H., Mason, M., Katsinelos, T., McEwan, W. A., Ghetti, B., Tolkovsky, A. M., et al. (2021).
616 Microglia become hypofunctional and release metalloproteases and tau seeds when
617 phagocytosing live neurons with P301S tau aggregates. *Science Advances* 7, eabg4980. doi:
618 10.1126/sciadv.abg4980

619 Burbidge, K., Rademacher, D. J., Mattick, J., Zack, S., Grillini, A., Bousset, L., et al. (2022). LGALS3
620 (galectin 3) mediates an unconventional secretion of SNCA/α-synuclein in response to
621 lysosomal membrane damage by the autophagic-lysosomal pathway in human midbrain
622 dopamine neurons. *Autophagy* 18, 1020–1048. doi: 10.1080/15548627.2021.1967615

623 Byrns, C. N., Saikumar, J., and Bonini, N. M. (2021). Glial AP1 is activated with aging and accelerated
624 by traumatic brain injury. *Nat Aging* 1, 585–597. doi: 10.1038/s43587-021-00072-0
625 Cardoso, C. M. P., Jordao, L., and Vieira, O. V. (2010). Rab10 regulates phagosome maturation and its
626 overexpression rescues Mycobacterium-containing phagosomes maturation. *Traffic* 11, 221–
627 235. doi: 10.1111/j.1600-0854.2009.01013.x
628 Casula, M., Iyer, A. M., Spliet, W. G. M., Anink, J. J., Steentjes, K., Sta, M., et al. (2011). Toll-like
629 receptor signaling in amyotrophic lateral sclerosis spinal cord tissue. *Neuroscience* 179, 233–
630 243. doi: 10.1016/j.neuroscience.2011.02.001
631 Chan, C.-C., Scoggin, S., Wang, D., Cherry, S., Dembo, T., Greenberg, B., et al. (2011). Systematic
632 Discovery of Rab GTPases with Synaptic Functions in Drosophila. *Current Biology* 21, 1704–
633 1715. doi: 10.1016/j.cub.2011.08.058
634 Chen, J. J., Nathaniel, D. L., Raghavan, P., Nelson, M., Tian, R., Tse, E., et al. (2019). Compromised
635 function of the ESCRT pathway promotes endolysosomal escape of tau seeds and propagation
636 of tau aggregation. *J. Biol. Chem.*, jbc.RA119.009432. doi: 10.1074/jbc.RA119.009432
637 Chen, S., Berthelier, V., Yang, W., and Wetzel, R. (2001). Polyglutamine aggregation behavior in vitro
638 supports a recruitment mechanism of cytotoxicity11Edited by F. Cohen. *Journal of Molecular*
639 *Biology* 311, 173–182. doi: 10.1006/jmbi.2001.4850
640 Choi, I., Zhang, Y., Seegobin, S. P., Pruvost, M., Wang, Q., Purtell, K., et al. (2020). Microglia clear
641 neuron-released α-synuclein via selective autophagy and prevent neurodegeneration. *Nat*
642 *Commun* 11, 1386. doi: 10.1038/s41467-020-15119-w
643 Chung, W.-S., Clarke, L. E., Wang, G. X., Stafford, B. K., Sher, A., Chakraborty, C., et al. (2013).
644 Astrocytes mediate synapse elimination through MEGF10 and MERTK pathways. *Nature* 504,
645 394–400. doi: 10.1038/nature12776
646 Couto, A., Alenius, M., and Dickson, B. J. (2005). Molecular, Anatomical, and Functional Organization
647 of the Drosophila Olfactory System. *Current Biology* 15, 1535–1547. doi:
648 10.1016/j.cub.2005.07.034

649 Daussy, C. F., and Wodrich, H. (2020). “Repair Me if You Can”: Membrane Damage, Response, and
650 Control from the Viral Perspective. *Cells* 9, 2042. doi: 10.3390/cells9092042
651 Dejanovic, B., Wu, T., Tsai, M.-C., Graykowski, D., Gandham, V. D., Rose, C. M., et al. (2022).
652 Complement C1q-dependent excitatory and inhibitory synapse elimination by astrocytes and
653 microglia in Alzheimer’s disease mouse models. *Nat Aging* 2, 837–850. doi: 10.1038/s43587-
654 022-00281-1
655 Doherty, J., Logan, M. A., Taşdemir, O. E., and Freeman, M. R. (2009). Ensheathing glia function as
656 phagocytes in the adult Drosophila brain. *J Neurosci* 29, 4768–4781. doi:
657 10.1523/JNEUROSCI.5951-08.2009
658 Donnelly, K. M., Coleman, C. M., Fuller, M. L., Reed, V. L., Smerina, D., Tomlinson, D. S., et al. (2022).
659 Hunting for the cause: Evidence for prion-like mechanisms in Huntington’s disease. *Frontiers in*
660 *Neuroscience* 16. Available at: https://www.frontiersin.org/articles/10.3389/fnins.2022.946822
661 (Accessed January 31, 2024).
662 Donnelly, K. M., DeLorenzo, O. R., Zaya, A. D., Pisano, G. E., Thu, W. M., Luo, L., et al. (2020).
663 Phagocytic glia are obligatory intermediates in transmission of mutant huntingtin aggregates
664 across neuronal synapses. *eLife* 9, e58499. doi: 10.7554/eLife.58499
665 Dunlop, J., Jones, P. C., and Finbow, M. E. (1995). Membrane insertion and assembly of ductin: a
666 polytopic channel with dual orientations. *EMBO J* 14, 3609–3616.
667 Dunst, S., Kazimiers, T., von Zadow, F., Jambor, H., Sagner, A., Brankatschk, B., et al. (2015).
668 Endogenously Tagged Rab Proteins: A Resource to Study Membrane Trafficking in Drosophila.
669 *Dev Cell* 33, 351–365. doi: 10.1016/j.devcel.2015.03.022
670 Duong, L., Radley, H., Lee, B., Dye, D., Pixley, F., Grounds, M., et al. (2021). Macrophage function in
671 the elderly and impact on injury repair and cancer. *Immunity & Ageing* 18, 4. doi:
672 10.1186/s12979-021-00215-2
673 Eapen, V. V., Swarup, S., Hoyer, M. J., Paulo, J. A., and Harper, J. W. (2021). Quantitative proteomics
674 reveals the selectivity of ubiquitin-binding autophagy receptors in the turnover of damaged
675 lysosomes by lysophagy. *eLife* 10, e72328. doi: 10.7554/eLife.72328

676 Eguchi, T., Kuwahara, T., Sakurai, M., Komori, T., Fujimoto, T., Ito, G., et al. (2018). LRRK2 and its
677 substrate Rab GTPases are sequentially targeted onto stressed lysosomes and maintain their
678 homeostasis. *Proc Natl Acad Sci U S A* 115, E9115–E9124. doi: 10.1073/pnas.1812196115
679 Evans, I. R., Rodrigues, F. S. L. M., Armitage, E. L., and Wood, W. (2015). Draper/CED-1 Mediates an
680 Ancient Damage Response to Control Inflammatory Blood Cell Migration In Vivo. *Curr Biol* 25,
681 1606–1612. doi: 10.1016/j.cub.2015.04.037
682 Falcon, B., Noad, J., McMahon, H., Randow, F., and Goedert, M. (2018). Galectin-8–mediated
683 selective autophagy protects against seeded tau aggregation. *J Biol Chem* 293, 2438–2451.
684 doi: 10.1074/jbc.M117.809293
685 Finbow, M. E., Goodwin, S. F., Meagher, L., Lane, N. J., Keen, J., Findlay, J. B. C., et al. (1994).
686 Evidence that the 16 kDa proteolipid (subunit c) of the vacuolar H+-ATPase and ductin from gap
687 junctions are the same polypeptide in Drosophila and Manduca: molecular cloning of the
688 Vha16k gene from Drosophila. *Journal of Cell Science* 107, 1817–1824. doi:
689 10.1242/jcs.107.7.1817
690 Flavin, W. P., Bousset, L., Green, Z. C., Chu, Y., Skarpathiotis, S., Chaney, M. J., et al. (2017).
691 Endocytic vesicle rupture is a conserved mechanism of cellular invasion by amyloid proteins.
692 *Acta Neuropathol* 134, 629–653. doi: 10.1007/s00401-017-1722-x
693 Freeman, D., Cedillos, R., Choyke, S., Lukic, Z., McGuire, K., Marvin, S., et al. (2013). Alpha-Synuclein
694 Induces Lysosomal Rupture and Cathepsin Dependent Reactive Oxygen Species Following
695 Endocytosis. *PLOS ONE* 8, e62143. doi: 10.1371/journal.pone.0062143
696 Fujita, Y., Maeda, T., Sato, C., Sato, M., Hatakeyama, H., Ota, Y., et al. (2020). Engulfment of Toxic
697 Amyloid β-protein in Neurons and Astrocytes Mediated by MEGF10. *Neuroscience* 443, 1–7.
698 doi: 10.1016/j.neuroscience.2020.07.016
699 Ginsberg, S. D., Mufson, E. J., Alldred, M. J., Counts, S. E., Wuu, J., Nixon, R. A., et al. (2011).
700 Upregulation of select rab GTPases in cholinergic basal forebrain neurons in mild cognitive
701 impairment and Alzheimer's disease. *J Chem Neuroanat* 42, 102–110. doi:
702 10.1016/j.jchemneu.2011.05.012

703 Hall, A. (1990). The Cellular Functions of Small GTP-Binding Proteins. doi: 10.1126/science.2116664
704 Han, C., Song, Y., Xiao, H., Wang, D., Franc, N. C., Jan, L. Y., et al. (2014). Epidermal cells are the
705 primary phagocytes in the fragmentation and clearance of degenerating dendrites in Drosophila.
706 *Neuron* 81, 544–560. doi: 10.1016/j.neuron.2013.11.021
707 Heckmann, B. L., Teubner, B. J. W., Tummers, B., Boada-Romero, E., Harris, L., Yang, M., et al.
708 (2019). LC3-associated endocytosis facilitates β-amyloid clearance and mitigates
709 neurodegeneration in murine Alzheimer's Disease. *Cell* 178, 536. doi:
710 10.1016/j.cell.2019.05.056
711 Herzog, C., Pons Garcia, L., Keatinge, M., Greenald, D., Moritz, C., Peri, F., et al. (2019). Rapid
712 clearance of cellular debris by microglia limits secondary neuronal cell death after brain injury in
713 vivo. *Development* 146, dev174698. doi: 10.1242/dev.174698
714 Homma, Y., Hiragi, S., and Fukuda, M. (2021). Rab family of small GTPases: an updated view on their
715 regulation and functions. *FEBS J* 288, 36–55. doi: 10.1111/febs.15453
716 Hong, S., Beja-Glasser, V. F., Nfonoyim, B. M., Frouin, A., Li, S., Ramakrishnan, S., et al. (2016).
717 Complement and microglia mediate early synapse loss in Alzheimer mouse models. *Science*
718 352, 712–716. doi: 10.1126/science.aad8373
719 Hopp, S. C., Lin, Y., Oakley, D., Roe, A. D., DeVos, S. L., Hanlon, D., et al. (2018). The role of
720 microglia in processing and spreading of bioactive tau seeds in Alzheimer's disease. *J*
721 *Neuroinflammation* 15, 269. doi: 10.1186/s12974-018-1309-z
722 Hutagalung, A. H., and Novick, P. J. (2011). Role of Rab GTPases in Membrane Traffic and Cell
723 Physiology. *Physiol Rev* 91, 119–149. doi: 10.1152/physrev.00059.2009
724 Iram, T., Ramirez-Ortiz, Z., Byrne, M. H., Coleman, U. A., Kingery, N. D., Means, T. K., et al. (2016).
725 Megf10 Is a Receptor for C1Q That Mediates Clearance of Apoptotic Cells by Astrocytes. *J*
726 *Neurosci* 36, 5185–5192. doi: 10.1523/JNEUROSCI.3850-15.2016
727 Jain, N., Lewis, C. A., Ulrich, J. D., and Holtzman, D. M. (2023). Chronic TREM2 activation exacerbates
728 Aβ-associated tau seeding and spreading. *J Exp Med* 220, e20220654. doi:
729 10.1084/jem.20220654

730 Jeong, G. R., Jang, E.-H., Bae, J. R., Jun, S., Kang, H. C., Park, C.-H., et al. (2018). Dysregulated
731 phosphorylation of Rab GTPases by LRRK2 induces neurodegeneration. *Molecular*
732 *Neurodegeneration* 13, 8. doi: 10.1186/s13024-018-0240-1
733 Jia, J., Claude-Taupin, A., Gu, Y., Choi, S. W., Peters, R., Bissa, B., et al. (2020). Galectin-3
734 coordinates a cellular system for lysosomal repair and removal. *Dev Cell* 52, 69-87.e8. doi:
735 10.1016/j.devcel.2019.10.025
736 Jiang, P., Gan, M., Yen, S.-H., McLean, P. J., and Dickson, D. W. (2017). Impaired endo-lysosomal
737 membrane integrity accelerates the seeding progression of α-synuclein aggregates. *Sci Rep* 7,
738 7690. doi: 10.1038/s41598-017-08149-w
739 Jiang, S., and Bhaskar, K. (2020). Degradation and Transmission of Tau by Autophagic-Endolysosomal
740 Networks and Potential Therapeutic Targets for Tauopathy. *Frontiers in Molecular Neuroscience*
741 13. Available at: https://www.frontiersin.org/articles/10.3389/fnmol.2020.586731 (Accessed
742 October 31, 2023).
743 Jucker, M., and Walker, L. C. (2018). Propagation and spread of pathogenic protein assemblies in
744 neurodegenerative diseases. *Nat. Neurosci.* 21, 1341–1349. doi: 10.1038/s41593-018-0238-6
745 Karran, E., and De Strooper, B. (2022). The amyloid hypothesis in Alzheimer disease: new insights
746 from new therapeutics. *Nat Rev Drug Discov* 21, 306–318. doi: 10.1038/s41573-022-00391-w
747 Katzenberger, R. J., Loewen, C. A., Wassarman, D. R., Petersen, A. J., Ganetzky, B., and Wassarman,
748 D. A. (2013). A Drosophila model of closed head traumatic brain injury. *Proceedings of the*
749 *National Academy of Sciences* 110, E4152–E4159. doi: 10.1073/pnas.1316895110
750 Kiral, F. R., Kohrs, F. E., Jin, E. J., and Hiesinger, P. R. (2018). Rab GTPases and Membrane
751 Trafficking in Neurodegeneration. *Curr Biol* 28, R471–R486. doi: 10.1016/j.cub.2018.02.010
752 Kluss, J. H., Beilina, A., Williamson, C. D., Lewis, P. A., Cookson, M. R., and Bonet-Ponce, L. (2022).
753 Lysosomal positioning regulates Rab10 phosphorylation at LRRK2+ lysosomes. *Proc Natl Acad*
754 *Sci U S A* 119, e2205492119. doi: 10.1073/pnas.2205492119
755 Knowles, T. P. J., Vendruscolo, M., and Dobson, C. M. (2014). The amyloid state and its association
756 with protein misfolding diseases. *Nat Rev Mol Cell Biol* 15, 384–396. doi: 10.1038/nrm3810

757 Kohrs, F. E., Daumann, I.-M., Pavlovic, B., Jin, E. J., Kiral, F. R., Lin, S.-C., et al. (2021). Systematic
758 functional analysis of rab GTPases reveals limits of neuronal robustness to environmental
759 challenges in flies. *eLife* 10, e59594. doi: 10.7554/eLife.59594
760 Kouli, A., Camacho, M., Allinson, K., and Williams-Gray, C. H. (2020). Neuroinflammation and protein
761 pathology in Parkinson's disease dementia. *Acta Neuropathologica Communications* 8, 211.
762 doi: 10.1186/s40478-020-01083-5
763 Krasemann, S., Madore, C., Cialic, R., Baufeld, C., Calcagno, N., El Fatimy, R., et al. (2017). The
764 TREM2-APOE Pathway Drives the Transcriptional Phenotype of Dysfunctional Microglia in
765 Neurodegenerative Diseases. *Immunity* 47, 566-581.e9. doi: 10.1016/j.immuni.2017.08.008
766 Langemeyer, L., Fröhlich, F., and Ungermann, C. (2018). Rab GTPase Function in Endosome and
767 Lysosome Biogenesis. *Trends in Cell Biology* 28, 957–970. doi: 10.1016/j.tcb.2018.06.007
768 Larsson, M. C., Domingos, A. I., Jones, W. D., Chiappe, M. E., Amrein, H., and Vosshall, L. B. (2004).
769 Or83b Encodes a Broadly Expressed Odorant Receptor Essential for Drosophila Olfaction.
770 *Neuron* 43, 703–714. doi: 10.1016/j.neuron.2004.08.019
771 Lee, H., Flynn, R., Sharma, I., Haberman, E., Carling, P. J., Nicholls, F. J., et al. (2020). LRRK2 Is
772 Recruited to Phagosomes and Co-recruits RAB8 and RAB10 in Human Pluripotent Stem Cell-
773 Derived Macrophages. *Stem Cell Reports* 14, 940–955. doi: 10.1016/j.stemcr.2020.04.001
774 Lee, J.-H., Kim, J.-Y., Noh, S., Lee, H., Lee, S. Y., Mun, J. Y., et al. (2021). Astrocytes phagocytose
775 adult hippocampal synapses for circuit homeostasis. *Nature* 590, 612–617. doi:
776 10.1038/s41586-020-03060-3
777 Lee, J.-H., Yang, D.-S., Goulbourne, C. N., Im, E., Stavrides, P., Pensalfini, A., et al. (2022). Faulty
778 autolysosome acidification in Alzheimer's disease mouse models induces autophagic build-up of
779 Aβ in neurons, yielding senile plaques. *Nat Neurosci* 25, 688–701. doi: 10.1038/s41593-022-
780 01084-8
781 Leyns, C. E. G., Gratuze, M., Narasimhan, S., Jain, N., Koscal, L. J., Jiang, H., et al. (2019). TREM2
782 function impedes tau seeding in neuritic plaques. *Nat Neurosci* 22, 1217–1222. doi:
783 10.1038/s41593-019-0433-0

Liddelow, S. A., Guttenplan, K. A., Clarke, L. E., Bennett, F. C., Bohlen, C. J., Schirmer, L., et al. (2017). Neurotoxic reactive astrocytes are induced by activated microglia. *Nature* 541, 481–487. doi: 10.1038/nature21029

Liddelow, S. A., Marsh, S. E., and Stevens, B. (2020). Microglia and Astrocytes in Disease: Dynamic Duo or Partners in Crime? *Trends Immunol* 41, 820–835. doi: 10.1016/j.it.2020.07.006

Liu, C.-C., Hu, J., Zhao, N., Wang, J., Wang, N., Cirrito, J. R., et al. (2017). Astrocytic LRP1 Mediates Brain Aβ Clearance and Impacts Amyloid Deposition. *J Neurosci* 37, 4023–4031. doi: 10.1523/JNEUROSCI.3442-16.2017

Liu, Z., Xu, E., Zhao, H. T., Cole, T., and West, A. B. (2020). LRRK2 and Rab10 coordinate macropinocytosis to mediate immunological responses in phagocytes. *EMBO J* 39, e104862. doi: 10.15252/embj.2020104862

MacDonald, J. M., Beach, M. G., Porpiglia, E., Sheehan, A. E., Watts, R. J., and Freeman, M. R. (2006). The Drosophila Cell Corpse Engulfment Receptor Draper Mediates Glial Clearance of Severed Axons. *Neuron* 50, 869–881. doi: 10.1016/j.neuron.2006.04.028

Magaki, S. D., Williams, C. K., and Vinters, H. V. (2018). Glial function (and dysfunction) in the normal & ischemic brain. *Neuropharmacology* 134, 218–225. doi: 10.1016/j.neuropharm.2017.11.009

Marischuk, K., Crocker, K. L., Ahern-Djamali, S., and Boekhoff-Falk, G. (2021). Innate immunity pathways activate cell proliferation after penetrating traumatic brain injury in adult Drosophila. 2021.09.01.458615. doi: 10.1101/2021.09.01.458615

McGuire, S. E., Le, P. T., and Davis, R. L. (2001). The Role of Drosophila Mushroom Body Signaling in Olfactory Memory. *Science* 293, 1330–1333. doi: 10.1126/science.1062622

McLaughlin, C. N., Perry-Richardson, J. J., Coutinho-Budd, J. C., and Broihier, H. T. (2019). Dying neurons utilize innate immune signaling to prime glia for phagocytosis during development. *Dev Cell* 48, 506-522.e6. doi: 10.1016/j.devcel.2018.12.019

Miesenböck, G., De Angelis, D. A., and Rothman, J. E. (1998). Visualizing secretion and synaptic transmission with pH-sensitive green fluorescent proteins. *Nature* 394, 192–195. doi: 10.1038/28190

811 Miron, J., Picard, C., Frappier, J., Dea, D., Théroux, L., and Poirier, J. (2018). TLR4 Gene Expression
812 and Pro-Inflammatory Cytokines in Alzheimer's Disease and in Response to Hippocampal
813 Deafferentation in Rodents. *Journal of Alzheimer's Disease* 63, 1547–1556. doi: 10.3233/JAD-
814 171160
815 Monaco, A., and Fraldi, A. (2020). Protein Aggregation and Dysfunction of Autophagy-Lysosomal
816 Pathway: A Vicious Cycle in Lysosomal Storage Diseases. *Front Mol Neurosci* 13, 37. doi:
817 10.3389/fnmol.2020.00037
818 Neniskyte, U., Neher, J. J., and Brown, G. C. (2011). Neuronal Death Induced by Nanomolar Amyloid β
819 Is Mediated by Primary Phagocytosis of Neurons by Microglia*. *Journal of Biological Chemistry*
820 286, 39904–39913. doi: 10.1074/jbc.M111.267583
821 Ng, E. L., and Tang, B. L. (2008). Rab GTPases and their roles in brain neurons and glia. *Brain*
822 *Research Reviews* 58, 236–246. doi: 10.1016/j.brainresrev.2008.04.006
823 Paolicelli, R. C., Bolasco, G., Pagani, F., Maggi, L., Scianni, M., Panzanelli, P., et al. (2011). Synaptic
824 pruning by microglia is necessary for normal brain development. *Science* 333, 1456–1458. doi:
825 10.1126/science.1202529
826 Parhizkar, S., Arzberger, T., Brendel, M., Kleinberger, G., Deussing, M., Focke, C., et al. (2019). Loss
827 of TREM2 function increases amyloid seeding but reduces plaque-associated ApoE. *Nat*
828 *Neurosci* 22, 191–204. doi: 10.1038/s41593-018-0296-9
829 Pearce, M. M. P., Spartz, E. J., Hong, W., Luo, L., and Kopito, R. R. (2015). Prion-like transmission of
830 neuronal huntingtin aggregates to phagocytic glia in the Drosophila brain. *Nat Commun* 6, 6768.
831 doi: 10.1038/ncomms7768
832 Podleśny-Drabiniok, A., Marcora, E., and Goate, A. M. (2020). Microglial Phagocytosis: A Disease-
833 Associated Process Emerging from Alzheimer's Disease Genetics. *Trends Neurosci* 43, 965–
834 979. doi: 10.1016/j.tins.2020.10.002
835 Poe, A. R., Wang, B., Sapar, M. L., Ji, H., Li, K., Onabajo, T., et al. (2019). Robust CRISPR/Cas9-
836 Mediated Tissue-Specific Mutagenesis Reveals Gene Redundancy and Perdurance in
837 Drosophila. *Genetics* 211, 459–472. doi: 10.1534/genetics.118.301736

838 Polanco, J. C., and Götz, J. (2022). Exosomal and vesicle-free tau seeds—propagation and
839 convergence in endolysosomal permeabilization. *The FEBS Journal* 289, 6891–6907. doi:
840 10.1111/febs.16055
841 Portela, M., Yang, L., Paul, S., Li, X., Veraksa, A., Parsons, L. M., et al. (2018). Lgl reduces endosomal
842 vesicle acidification and Notch signaling by promoting the interaction between Vap33 and the V-
843 ATPase complex. *Sci Signal* 11, eaar1976. doi: 10.1126/scisignal.aar1976
844 Potter, C. J., and Luo, L. (2011). Using the Q system in Drosophila. *Nat Protoc* 6, 1105–1120. doi:
845 10.1038/nprot.2011.347
846 Preisinger, E., Jordan, B. M., Kazantsev, A., and Housman, D. (1999). Evidence for a recruitment and
847 sequestration mechanism in Huntington's disease. *Philos Trans R Soc Lond B Biol Sci* 354,
848 1029–1034. doi: 10.1098/rstb.1999.0455
849 Prince, E., Kroeger, B., Gligorov, D., Wilson, C., Eaton, S., Karch, F., et al. (2019). Rab-mediated
850 trafficking in the secondary cells of Drosophila male accessory glands and its role in fecundity.
851 *Traffic* 20, 137–151. doi: 10.1111/tra.12622
852 Pulipparacharuvil, S., Akbar, M. A., Ray, S., Sevrioukov, E. A., Haberman, A. S., Rohrer, J., et al.
853 (2005). Drosophila Vps16A is required for trafficking to lysosomes and biogenesis of pigment
854 granules. *Journal of Cell Science* 118, 3663–3673. doi: 10.1242/jcs.02502
855 Purice, M. D., Ray, A., Münzel, E. J., Pope, B. J., Park, D. J., Speese, S. D., et al. (2017). A novel
856 Drosophila injury model reveals severed axons are cleared through a Draper/MMP-1 signaling
857 cascade. *eLife* 6, e23611. doi: 10.7554/eLife.23611
858 Purice, M. D., Speese, S. D., and Logan, M. A. (2016). Delayed glial clearance of degenerating axons
859 in aged Drosophila is due to reduced PI3K/Draper activity. *Nat Commun* 7. doi:
860 10.1038/ncomms12871
861 Raiders, S., Han, T., Scott-Hewitt, N., Kucenas, S., Lew, D., Logan, M. A., et al. (2021). Engulfed by
862 Glia: Glial Pruning in Development, Function, and Injury across Species. *J. Neurosci.* 41, 823–
863 833. doi: 10.1523/JNEUROSCI.1660-20.2020

Ray, A., Speese, S. D., and Logan, M. A. (2017). Glial Draper Rescues Aβ Toxicity in a Drosophila Model of Alzheimer's Disease. *J Neurosci* 37, 11881–11893. doi: 10.1523/JNEUROSCI.0862-17.2017

Ridge, P. G., Karch, C. M., Hsu, S., Arano, I., Teerlink, C. C., Ebbert, M. T. W., et al. (2017). Linkage, whole genome sequence, and biological data implicate variants in RAB10 in Alzheimer's disease resilience. *Genome Med* 9, 100. doi: 10.1186/s13073-017-0486-1

Rivero-Ríos, P., Romo-Lozano, M., Fernández, B., Fdez, E., and Hilfiker, S. (2020). Distinct Roles for RAB10 and RAB29 in Pathogenic LRRK2-Mediated Endolysosomal Trafficking Alterations. *Cells* 9, 1719. doi: 10.3390/cells9071719

Rodrigues, P. V., de Godoy, J. V. P., Bosque, B. P., Amorim Neto, D. P., Tostes, K., Palameta, S., et al. (2022). Transcellular propagation of fibrillar α-synuclein from enteroendocrine to neuronal cells requires cell-to-cell contact and is Rab35-dependent. *Sci Rep* 12, 4168. doi: 10.1038/s41598-022-08076-5

Rodriguez, L., Mohamed, N.-V., Desjardins, A., Lippé, R., Fon, E. A., and Leclerc, N. (2017). Rab7A regulates tau secretion. *J Neurochem* 141, 592–605. doi: 10.1111/jnc.13994

Rong, Y., McPhee, C. K., Deng, S., Huang, L., Chen, L., Liu, M., et al. (2011). Spinster is required for autophagic lysosome reformation and mTOR reactivation following starvation. *Proc Natl Acad Sci U S A* 108, 7826–7831. doi: 10.1073/pnas.1013800108

Santra, M., Dill, K. A., and de Graff, A. M. R. (2019). Proteostasis collapse is a driver of cell aging and death. *Proceedings of the National Academy of Sciences* 116, 22173–22178. doi: 10.1073/pnas.1906592116

Scherzinger, E., Sittler, A., Schweiger, K., Heiser, V., Lurz, R., Hasenbank, R., et al. (1999). Self-assembly of polyglutamine-containing huntingtin fragments into amyloid-like fibrils: Implications for Huntington's disease pathology. *Proc Natl Acad Sci U S A* 96, 4604–4609.

Seol, W., Nam, D., and Son, I. (2019). Rab GTPases as Physiological Substrates of LRRK2 Kinase. *Exp Neurobiol* 28, 134–145. doi: 10.5607/en.2019.28.2.134

890 Seto, S., Tsujimura, K., and Koide, Y. (2011). Rab GTPases regulating phagosome maturation are
891 differentially recruited to mycobacterial phagosomes. *Traffic* 12, 407–420. doi: 10.1111/j.1600-
892 0854.2011.01165.x
893 Singh, T. D., Park, S.-Y., Bae, J., Yun, Y., Bae, Y.-C., Park, R.-W., et al. (2010). MEGF10 functions as
894 a receptor for the uptake of amyloid-β. *FEBS Letters* 584, 3936–3942. doi:
895 10.1016/j.febslet.2010.08.050
896 Small, S. A., Simoes-Spassov, S., Mayeux, R., and Petsko, G. A. (2017). Endosomal traffic jams
897 represent a pathogenic hub and therapeutic target in Alzheimer's disease. *Trends Neurosci* 40,
898 592–602. doi: 10.1016/j.tins.2017.08.003
899 Steger, M., Tonelli, F., Ito, G., Davies, P., Trost, M., Vetter, M., et al. (2016). Phosphoproteomics
900 reveals that Parkinson's disease kinase LRRK2 regulates a subset of Rab GTPases. *Elife* 5,
901 e12813. doi: 10.7554/eLife.12813
902 Stein, K. C., Morales-Polanco, F., van der Lienden, J., Rainbolt, T. K., and Frydman, J. (2022). Ageing
903 exacerbates ribosome pausing to disrupt cotranslational proteostasis. *Nature* 601, 637–642. doi:
904 10.1038/s41586-021-04295-4
905 Streubel-Gallasch, L., Giusti, V., Sandre, M., Tessari, I., Plotegher, N., Giusto, E., et al. (2021).
906 Parkinson's Disease–Associated LRRK2 Interferes with Astrocyte-Mediated Alpha-Synuclein
907 Clearance. *Mol Neurobiol* 58, 3119–3140. doi: 10.1007/s12035-021-02327-8
908 Swanson, L. C., Rimkus, S. A., Ganetzky, B., and Wassarman, D. A. (2020a). Loss of the Antimicrobial
909 Peptide Metchnikowin Protects Against Traumatic Brain Injury Outcomes in Drosophila
910 melanogaster. *G3 (Bethesda)* 10, 3109–3119. doi: 10.1534/g3.120.401377
911 Swanson, L. C., Trujillo, E. A., Thiede, G. H., Katzenberger, R. J., Shishkova, E., Coon, J. J., et al.
912 (2020b). Survival Following Traumatic Brain Injury in Drosophila Is Increased by Heterozygosity
913 for a Mutation of the NF-κB Innate Immune Response Transcription Factor Relish. *Genetics*
914 216, 1117–1136. doi: 10.1534/genetics.120.303776

915 Tavana, J. P., Rosene, M., Jensen, N. O., Ridge, P. G., Kauwe, J. S., and Karch, C. M. (2018). RAB10:
916 an Alzheimer's disease resilience locus and potential drug target. *Clin Interv Aging* 14, 73–79.
917 doi: 10.2147/CIA.S159148
918 Tezuka, T., Taniguchi, D., Sano, M., Shimada, T., Oji, Y., Tsunemi, T., et al. (2022). Pathophysiological
919 evaluation of the LRRK2 G2385R risk variant for Parkinson's disease. *npj Parkinsons Dis.* 8, 1–
920 7. doi: 10.1038/s41531-022-00367-y
921 Udayar, V., Buggia-Prévot, V., Guerreiro, R. L., Siegel, G., Rambabu, N., Soohoo, A. L., et al. (2013). A
922 Paired RNAi and RabGAP Overexpression Screen Identifies Rab11 as a Regulator of β-Amyloid
923 Production. *Cell Rep* 5, 1536–1551. doi: 10.1016/j.celrep.2013.12.005
924 Udayar, V., Chen, Y., Sidransky, E., and Jagasia, R. (2022). Lysosomal dysfunction in
925 neurodegeneration: emerging concepts and methods. *Trends in Neurosciences* 45, 184–199.
926 doi: 10.1016/j.tins.2021.12.004
927 Ugbode, C., Fort-Aznar, L., and Sweeney, S. T. (2019). Leaky endosomes push tau over the seed limit.
928 *Journal of Biological Chemistry* 294, 18967–18968. doi: 10.1074/jbc.H119.011687
929 Vieira, O. V., Botelho, R. J., and Grinstein, S. (2002). Phagosome maturation: aging gracefully.
930 *Biochem J* 366, 689–704. doi: 10.1042/BJ20020691
931 Wakida, N. M., Cruz, G. M. S., Ro, C. C., Moncada, E. G., Khatibzadeh, N., Flanagan, L. A., et al.
932 (2018). Phagocytic response of astrocytes to damaged neighboring cells. *PLOS ONE* 13,
933 e0196153. doi: 10.1371/journal.pone.0196153
934 Wang, C., Fan, L., Khawaja, R. R., Liu, B., Zhan, L., Kodama, L., et al. (2022). Microglial NF-κB drives
935 tau spreading and toxicity in a mouse model of tauopathy. *Nat Commun* 13, 1969. doi:
936 10.1038/s41467-022-29552-6
937 Wang, Y., Arnold, M. L., Smart, A. J., Wang, G., Androwski, R. J., Morera, A., et al. (2023). Large
938 vesicle extrusions from C. elegans neurons are consumed and stimulated by glial-like
939 phagocytosis activity of the neighboring cell. *eLife* 12, e82227. doi: 10.7554/eLife.82227
940 Wanker, E. E. (2000). Protein Aggregation and Pathogenesis of Huntingtons Disease: Mechanisms and
941 Correlations. 381, 937–942. doi: 10.1515/BC.2000.114

942 Welikovitch, L. A., Dujardin, S., Dunn, A. R., Fernandes, A. R., Khasnavis, A., Chibnik, L. B., et al.
943 (2023). Rate of tau propagation is a heritable disease trait in genetically diverse mouse strains.
944 *iScience* 26, 105983. doi: 10.1016/j.isci.2023.105983
945 Wodrich, A. P. K., Scott, A. W., Shukla, A. K., Harris, B. T., and Giniger, E. (2022). The Unfolded
946 Protein Responses in Health, Aging, and Neurodegeneration: Recent Advances and Future
947 Considerations. *Front Mol Neurosci* 15, 831116. doi: 10.3389/fnmol.2022.831116
948 Yan, T., Wang, L., Gao, J., Siedlak, S. L., Huntley, M. L., Termsarasab, P., et al. (2018). Rab10
949 Phosphorylation is a Prominent Pathological Feature in Alzheimer's Disease. *J Alzheimers Dis*
950 63, 157–165. doi: 10.3233/JAD-180023
951 Yan, Y., Denef, N., and Schüpbach, T. (2009). The vacuolar proton pump (V-ATPase) is required for
952 Notch signaling and endosomal trafficking in Drosophila. *Dev Cell* 17, 387–402. doi:
953 10.1016/j.devcel.2009.07.001
954 Yuste-Checa, P., Trinkaus, V. A., Riera-Tur, I., Imamoglu, R., Schaller, T. F., Wang, H., et al. (2021).
955 The extracellular chaperone Clusterin enhances Tau aggregate seeding in a cellular model. *Nat*
956 *Commun* 12, 4863. doi: 10.1038/s41467-021-25060-1
957 Zhang, J., Schulze, K. L., Hiesinger, P. R., Suyama, K., Wang, S., Fish, M., et al. (2007). Thirty-One
958 Flavors of Drosophila Rab Proteins. *Genetics* 176, 1307–1322. doi:
959 10.1534/genetics.106.066761
960 Zheng, B., and Tuszynski, M. H. (2023). Regulation of axonal regeneration after mammalian spinal cord
961 injury. *Nat Rev Mol Cell Biol* 24, 396–413. doi: 10.1038/s41580-022-00562-y
962

963 **FIGURE LEGENDS**

964 **Figure 1. mHTT$_{ex1}$ expression in ORNs impairs clearance of injured axons**. (**A-B**) Maximum
965 intensity projections of mCD8-GFP-labeled DA1 ORN axons expressing (**A**) HTT$_{ex1}$Q25- (wtHTT$_{ex1}$) or
966 (**B**) HTT$_{ex1}$Q91-mCherry (mHTT$_{ex1}$) in 7 day-old uninjured flies (*left*) or 14 day-old flies subjected to
967 bilateral antennal nerve axotomy 7 days earlier (*right*). Scale bars = 5 µm. (**C-D**) Quantification of (**C**)
968 mCD8-GFP+ and (**D**) HTT$_{ex1}$-mCherry+ DA1 ORN axons remaining in 7, 14, and 28 day-old uninjured
969 flies or flies at 1, 3, and 5 days post-injury. (**E**) Quantification of mCD8-GFP+ DA1 ORN axons in 7, 14,
970 and 28 day-old flies expressing HTT$_{ex1}$Q25- or HTT$_{ex1}$Q91-mCherry in DA1 ORNs. All quantified data
971 were normalized to uninjured 1 day-old adults and graphed as mean ± s.e.m.; *p<0.05, **p<0.01,
972 ***p<0.001, ****p<0.0001 by unpaired two-tailed *t*-test.

973

974 **Figure 2. mHTT$_{ex1}$ expression in glia is associated with reduced ORN axon clearance post-injury.**
975 (**A-B**) Maximum intensity projections of antennal lobes from 5-6 day-old flies expressing HTT$_{ex1}$Q25-
976 (*top*) or HTT$_{ex1}$Q91-V5 (*bottom*) in glia and immunostained with anti-V5. Scale bars = 10 µm. (**B-C**)
977 Maximum intensity projections of mCD8-GFP-labeled DA1 ORN axons in 1 day-old flies expressing (**B**)
978 HTT$_{ex1}$Q25- or (**C**) HTT$_{ex1}$Q91-V5 in repo+ glia. Scale bars = 5 µm. (**D**) Quantification of mCD8-GFP+
979 DA1 ORN axons in flies expressing HTT$_{ex1}$Q25- or HTT$_{ex1}$Q91-V5 in repo+ glia, either uninjured or at 1
980 and 3 days post-injury. (**E**) Quantification of mCD8-GFP+ DA1 ORN axons in 1 day-old flies expressing
981 HTT$_{ex1}$Q25- or HTT$_{ex1}$Q91-mCherry in repo+ glia. All data were normalized to uninjured 1 day-old adult
982 flies and graphed as mean ± s.e.m.; ***p<0.001 by unpaired two-tailed *t*-test.

983

984 **Figure 3. mHTT$_{ex1}$ expression inhibits engulfment of injured ORN axons.** (**A-B**) Maximum intensity
985 projections of VA1lm ORN axons co-expressing the ratiometric phagocytic indicator, MApHS, and (**A**)
986 HTT$_{ex1}$Q25- or (**B**) HTT$_{ex1}$Q91-V5 from 7 day-old uninjured flies (*left*) and flies 25 hours post-injury
987 (*right*). Scale bars = 10µm. (**C**) pHluorin:tdTomato fluorescence intensity ratios calculated in VA1lm
988 glomeruli from 7-day-old uninjured flies and flies at 14 or 25 hours post-injury. Data were normalized to
989 the uninjured condition for each genotype. (**D**) pHluorin:tdTomato fluorescence intensity ratios in 7 day-

990 old flies co-expressing MApHS with HTT_{ex1}Q25- or HTT_{ex1}Q91-V5 in VA1lm ORNs, normalized to
991 wtHTT_{ex1} controls. Data are shown as mean ± s.e.m.; ***p*<0.01, ****p*<0.001, *****p*<0.0001 by unpaired
992 two-tailed *t*-test. (**E-F**) Maximum intensity projections of the central brain from 6-7 day-old flies
993 expressing (**E**) repo-Cas9 and (**F**) repo-Cas9 plus gRNAs targeting *draper* ("Draper KO"). Brains were
994 immunostained with anti-Draper. Scale bars = 10 µm. (**G**) Quantification of Draper immunofluorescence
995 in brains from flies shown in (**E-F**), normalized to control.
996
997 **Figure 4. Neuronal mHTT_{ex1} accumulates in acidic cellular compartments. (A-B, D-E)** Maximum
998 intensity projections of (**A-B**) Or83b+ ORN axons or (**D-E**) OK107+ MBN soma expressing (**A,D**)
999 HTT_{ex1}Q25- or (**B,E**) HTT_{ex1}Q91-associated pH sensor (HApHS) from 13-14 day-old flies. Scale bars =
1000 10 µm. (**C,F**) pHluorin:tdTomato fluorescence intensity ratios of data shown in (**A-B** and **D-E**),
1001 normalized to wtHTT_{ex1} controls. (**G-H**) Maximum intensity projections of VA1lm ORN axons co-
1002 expressing mHApHS and (**G**) repo-Cas9 or (**H**) repo-Cas9 and gRNAs targeting *draper*. Scale bars = 5
1003 µm. (**I**) pHluorin:tdTomato fluorescence intensity ratios calculated in VA1lm glomeruli from 9-10 day-old
1004 flies as shown in (**G-H**). Data were normalized to flies not expressing gRNAs. All quantified data are
1005 shown as mean ± s.e.m.; ***p*<0.01, ****p*<0.001, ****p<0.0001 by unpaired two-tailed *t*-test.
1006
1007 **Figure 5. mHTT_{ex1} expression in ORNs upregulates phagocytic and innate immunity genes and**
1008 **impairs injury-induced transcriptional responses.** (**A**) Diagrams of Toll-6 (purple) and Draper (blue)
1009 signaling pathways. (**B**) qPCR analysis of the indicated genes in 8-11 day-old flies expressing GFP,
1010 HTT_{ex1}Q25-, or HTT_{ex1}Q91-GFP in Or83b+ ORNs. RNA was isolated from heads of uninjured flies or
1011 flies 3 hours after bilateral antennal and maxillary palp nerve injury. Data are shown as mean ± s.e.m
1012 and normalized to the housekeeping gene *rpl32*. **p*<0.05, ***p*<0.01, ****p*<0.001 by one-way ANOVA;
1013 asterisks and hashtags indicate statistical significance comparing -/+ injury or genotypes, respectively.
1014 (**C-D and F-G**) Maximum intensity projections of Or83b+ ORN axons from 14-15 day-old flies
1015 expressing (**C,F**) HTT_{ex1}Q25- or (**D,G**) HTT_{ex1}Q91-V5 in (**C-D**) Toll-$6^{MIMICGFP}$ (Toll-6-GFP) or (**F-G**) Jra-
1016 GFP genetic backgrounds. Brains were immunostained with GFP, V5, and N-Cadherin (**C-D**) or GFP,

1017 Repo, and N-Cadherin (**F-G**) antibodies. In panel (**C**), diffuse wtHTT$_{ex1}$ signal was adjusted post-
1018 acquisition for increased visibility. Scale bars = 10 μm. (**E,H**) Quantification of (**E**) Toll-6-GFP or (**H**) Jra-
1019 GFP expression from flies show in (**C-D** and **F-G**). Data are graphed as mean ± s.e.m.; *p<0.05,
1020 ****p<0.0001 by unpaired two-tailed t-test.
1021
1022 **Figure 6. mHTT$_{ex1}$ expression in ORNs increases expression and impairs injury-induced**
1023 **upregulation of some AMP genes.** (**A-E**) qPCR analysis of the indicated AMP genes in 8-11 day-old
1024 flies expressing HTT$_{ex1}$Q25- or HTT$_{ex1}$Q91-GFP in Or83b+ ORNs. RNA was isolated from heads of
1025 uninjured flies or flies 3 hours after bilateral antennal and maxillary palp nerve injury. Data are shown
1026 as mean ± s.e.m and normalized to the housekeeping gene *rpl32*. **p<0.01, ***p<0.001 by unpaired
1027 two-tailed t-test; asterisks and hashtags indicate statistical significance comparing -/+ injury or
1028 genotypes, respectively.
1029
1030 **Figure 7. A subset of mHTT$_{ex1}$ aggregates are closely associated with Draper+ glial membranes**.
1031 (**A-B**) Maximum intensity projections of Or83b+ ORN axons from 7-8 day-old flies expressing (**A**)
1032 HTT$_{ex1}$Q25- or (**B**) HTT$_{ex1}$Q91-mCherry and immunostained for Draper. Scale bars = 10 μm. (**C**)
1033 Quantification of Draper immunofluorescence from flies show in (**A-B**). Data are normalized to control
1034 and graphed as mean ± s.e.m.; *p<0.05 by unpaired two-tailed *t*-test; n=12. (**D**) Single 0.35 μm
1035 confocal slice showing magnified HTT$_{ex1}$Q91-mCherry aggregate and associated Draper signal. Scale
1036 bar = 0.5 μm. (**E-F**) High-magnification confocal stacks of Draper signal within ≤0.2 μm of either (**E**)
1037 HTT$_{ex1}$Q25- or (**F1-3**) HTT$_{ex1}$Q91-mCherry surfaces. Raw data are shown to the left of segmented
1038 surfaces generated from each fluorescence signal. In (**E**), diffuse wtHTT$_{ex1}$ signal was adjusted post-
1039 acquisition for increased visibility. Scale bars = 1 μm.
1040
1041 **Figure 8. Seeded aggregation of wtHTT$_{ex1}$ protein expressed in ensheathing glia by neuronal**
1042 **mHTT$_{ex1}$ aggregates.** (**A-B**) Maximum intensity projections of DA1 glomeruli from 4-5 day-old flies
1043 expressing HTT$_{ex1}$Q91-mCherry in DA1 ORNs and HTT$_{ex1}$Q25-GFP in (**A**) mz0709+ ensheathing glia or

1044 (**B**) Alrm+ astrocytic glia. Scale bars = 5 μm. (**C-D**) Quantification of (**C**) HTT_{ex1}Q91-mCherry ("mHTT")
1045 and (**D**) seeded HTT_{ex1}Q25-GFP ("mHTT+wtHTT") aggregates from flies shown in (**A-B**). Data are
1046 shown as mean ± s.e.m.; ***p<0.001 by unpaired two-tailed t-test.
1047
1048 **Figure 9. Glial phagocytic and innate immunity genes regulate numbers of $mHTT_{ex1}$ aggregates**
1049 **in ORN axons. (A**) Maximum intensity projections of DA1 glomeruli from 7 day-old flies expressing
1050 HTT_{ex1}Q91-mCherry in DA1 ORNs and siRNAs targeting the indicated genes in ensheathing glia. Scale
1051 bars = 5 μm. (**B)** Quantification of HTT_{ex1}Q91-mCherry aggregates detected in DA1 glomeruli from flies
1052 shown in (**A**). (**C**) Maximum intensity projections of DA1 glomeruli from 7 day-old flies expressing
1053 HTT_{ex1}Q91-mCherry in DA1 ORNs and siRNAs targeting mCherry or Ets21c in repo+ glia in the
1054 presence of tubP-Gal80^{ts}. Adult flies were raised at the permissive (18°C, *top*) or restrictive (29°C,
1055 *bottom*) temperatures to regulate siRNA expression in adults. Scale bars = 5 μm. (**D**) Quantification of
1056 HTT_{ex1}Q91-mCherry aggregates detected in DA1 glomeruli from flies shown in (**C**). (**E**) Mean volumes
1057 for HTT_{ex1}Q91-mCherry aggregates detected in DA1 glomeruli from flies shown in (**A and C**). All
1058 graphed data are shown as mean ± s.e.m.; *p<0.05, **p<0.01, ***p<0.001 by one-way ANOVA or
1059 unpaired two-tail t-test compared to no RNAi or mCherry^{RNAi} controls.
1060
1061 **Figure 10. Neuronal $mHTT_{ex1}$ expression increases numbers of acidified and active lysosomes in**
1062 **adult brains. (A-B**) Maximum intensity projections of antennal lobes from 9-10 day-old adult flies
1063 expressing (**A**) HTT_{ex1}Q25- or (**B**) HTT_{ex1}Q91-GFP in Or83b+ ORNs and stained with Magic Red (MR)
1064 to label active cathepsins. Scale bars = 10 μm. (**C**) Quantification of MR+ surfaces (*left*) and HTT_{ex1}-
1065 associated MR+ surfaces (*right*) from flies shown in (**A** and **B**); HTT_{ex1}-associated vesicles were defined
1066 by filtering for MR+ surfaces ≤0.2 μm from HTT_{ex1} fluorescent signal in confocal stacks. **(D-E**) Maximum
1067 intensity projections of antennal lobes from 15 day-old flies expressing (**D**) HTT_{ex1}Q25- or (**E**)
1068 HTT_{ex1}Q91-GFP in Or83b+ ORNs and stained with Lysotracker Red (LTR) to label low pH
1069 compartments. Scale bars = 10 μm. Diffuse $wtHTT_{ex1}$ signal was adjusted post-acquisition for increased
1070 visibility in panels (**A** and **D**). (**F**) Quantification of LTR+ surfaces (*left*) and HTT_{ex1}-associated LTR+

1071 surfaces (*right*) from flies shown in (**D** and **E**); HTT_{ex1}-associated vesicles were defined by filtering for
1072 LTR+ surfaces ≤0.2 μm from HTT_{ex1} fluorescent signal in confocal stacks. Data are shown as mean ±
1073 s.e.m.; ****p<0.0001 by unpaired two-tailed t-test. (**G-H**) High-magnification images of boxes indicated
1074 in (**B and E**) showing co-localization of MR (**G**) or LTR (**H**) with $mHTT_{ex1}$ fluorescent signals. Scale bars
1075 = 1 μm.
1076
1077 **Figure 11. LAMP1+ vesicle accumulation in fly brains expressing $mHTT_{ex1}$ in ORNs. (A-B**)
1078 Confocal stacks showing antennal lobes from 19-22 day-old flies expressing (**A**) HTT_{ex1}Q25- or (**B**)
1079 HTT_{ex1}Q91-mCherry in Or83b+ ORNs and LAMP1 tagged at its cytoplasmic C-terminus with GFP
1080 (LAMP1-GFP) in glia. Brains were immunostained with anti-GFP to amplify LAMP1-GFP signal.
1081 LAMP1-GFP+ or HTT_{ex1}+ segmented surfaces are shown to the right of each set of raw fluorescence
1082 images. Insets show magnified regions of interest from each image. Scale bars = 10 μm. (**C**) High-
1083 magnification confocal stack showing a LAMP1-GFP+ surface within 0.2 μm of two HTT_{ex1}Q91-
1084 mCherry+ aggregates. Scale bar = 1 μm. **(D-E**) Confocal stacks showing antennal lobes from 21-22
1085 day-old flies expressing (**D**) HTT_{ex1}Q25- or (**E**) HTT_{ex1}Q91-mCherry in Or83b+ ORNs and LAMP1
1086 tagged at its luminal N-terminus with GFP (GFP-LAMP1) in glia. GFP-LAMP1+ or HTT_{ex1}+ segmented
1087 surfaces are shown to the right of each set of raw fluorescence images. Insets show a single GFP-
1088 LAMP1+ surface of interest from each image. Scale bars = 10 μm. Diffuse $wtHTT_{ex1}$ signal was
1089 adjusted post-acquisition for increased visibility in panels (**A** and **D**). (**F**) High-magnification confocal
1090 stack showing a GFP-LAMP1+ surface within 0.2 μm of a HTT_{ex1}Q91-mCherry+ aggregate. Scale bar =
1091 1μm. (**G-I**) Quantification of total LAMP1-GFP+ or GFP-LAMP1+ surfaces (**G**), LAMP1-GFP+ or GFP-
1092 LAMP1+ surfaces ≤0.2 μm from HTT_{ex1} surfaces (**H**), and mean LAMP1-GFP+ or GFP-LAMP1+
1093 surface volume (**I**) in brains expressing HTT_{ex1}Q25- or HTT_{ex1}Q91-mCherry. The dark red bars in (**I**)
1094 represent LAMP1+ surfaces that co-localized with $mHTT_{ex1}$. All graphed data are shown as mean ±
1095 s.e.m.; *p<0.05, **p<0.01, ***p<0.001, ****p<0.0001 by unpaired two-tailed t-test.
1096

1097 **Figure 12. Increased association of Galectins-3 and -8 expressed in glia with neuronal mHTT$_{ex1}$**
1098 **aggregates. (A-D**) Confocal stacks showing antennal lobes from 16-18 day-old flies expressing
1099 HTT$_{ex1}$Q25- (**A and C**) or HTT$_{ex1}$Q91-GFP (**B and D**) in Or83b+ ORNs together with Galectin-3 (**A-B**) or
1100 Galectin-8 (**C-D**) tagged with mCherry in glia. Segmented Galectin+ or HTT$_{ex1}$+ surfaces are shown to
1101 the right of each set of raw fluorescence images. Insets show Galectin+ surfaces of interest from each
1102 image. Scale bars = 10 μm. (**E-G**) Quantification of total Galectin+ surfaces (**E**), Galectin+ surfaces
1103 ≤0.2 μm from HTT$_{ex1}$ surfaces (**F**), and mean Galectin+ surface volume (**G**) in brains expressing
1104 HTT$_{ex1}$Q25- or HTT$_{ex1}$Q91-mCherry. The dark red bars in (**G**) represent Galectin+ surfaces that co-
1105 localized with mHTT$_{ex1}$. All graphed data are shown as mean ± s.e.m.; *p<0.05, **p<0.01, ***p<0.001,
1106 ****p<0.0001 by unpaired two-tailed *t*-test.
1107
1108 **Figure 13. Knockdown of genes regulating lysosome acidification alters seeded aggregation of**
1109 **glial wtHTT$_{ex1}$ protein by neuronal mHTT$_{ex1}$ aggregates.** (**A**) Confocal stacks showing DA1 glomeruli
1110 from 8-9 day-old flies expressing HTT$_{ex1}$Q91-mCherry in DA1 ORNs and HTT$_{ex1}$Q25-GFP plus siRNAs
1111 targeting the indicated genes in repo+ glia. Negative controls expressed siRNAs targeting mCherry.
1112 Scale bars = 5 μm. (**B-C**) Quantification of (**B**) HTT$_{ex1}$Q91-mCherry or (**C**) seeded HTT$_{ex1}$Q25-GFP
1113 aggregates from brains shown in (**A**). Data are shown as mean ± s.e.m.; *p<0.05, ***p<0.005 by
1114 unpaired two-tailed *t*-test.
1115
1116 **Figure 14. Rab10 is required for seeded aggregation of glial wtHTT$_{ex1}$ by neuronal mHTT$_{ex1}$**
1117 **aggregates.** (**A**) Confocal stacks of DA1 glomeruli from 7 day-old flies expressing HTT$_{ex1}$Q91-mCherry
1118 in DA1 ORNs and HTT$_{ex1}$Q25-GFP plus siRNAs targeting firefly luciferase (FFLuc), Draper, or Rab10 in
1119 repo+ glia. Surfaces representing mHTT$_{ex1}$ aggregates (*red*) and seeded wtHTT$_{ex1}$ aggregates are
1120 superimposed on the raw data. Scale bars = 5μm. (**B-C**) mHTT$_{ex1}$ (**B**) or mHTT$_{ex1}$+wtHTT$_{ex1}$ (**C**)
1121 aggregates quantified from flies expressing HTT$_{ex1}$Q91-mCherry in DA1 ORNs and HTT$_{ex1}$Q25-GFP
1122 plus siRNAs targeting Draper-I (Drpr) or 23 different Rab GTPases in repo+ glia. Negative controls
1123 expressed no siRNAs or siRNAs targeting FFLuc or mCherry (*black bars*). (**D**) Normalized Draper

1124 immunofluorescence in the central brain of 4-5 day-old wild-type (*rab10* $^{+/+}$) and *rab10* null (*rab10* $^{-/-}$)
1125 flies. (**E**) Quantification of seeded wtHTT$_{ex1}$ aggregates in flies expressing HTT$_{ex1}$Q91-mCherry in DA1
1126 ORNs and HTT$_{ex1}$Q25-GFP plus siRNAs targeting Rab10, without or with Draper-I cDNAs in repo+glia.
1127 (**F-G**) Quantification of mHTT$_{ex1}$ (**F**) or mHTT$_{ex1}$+wtHTT$_{ex1}$ (**G**) aggregates from 10 day-old flies
1128 expressing HTT$_{ex1}$Q91-mCherry in DA1 ORNs and HTT$_{ex1}$Q25-GFP in PNs, either heterozygous or
1129 trans-heterozygous for *draper* (*drpr/*+), *rab10* (*rab10/*+), or *rab14* (*rab14/*+) mutant alleles. All graphed
1130 data are shown as mean ± s.e.m.; *p<0.05, **p<0.01, ***p<0.005 by one-way ANOVA or unpaired two-
1131 tailed *t*-test comparing to controls.
1132
1133 **Figure 15. Association of neuronal mHTT$_{ex1}$ aggregates with Rab GTPases that label early,**
1134 **maturing, and late phagosomes. (A)** qPCR analysis of *rab10*, *rab5*, and *rab7* expression in 8-11 day-
1135 old flies expressing GFP, HTT$_{ex1}$Q25-, or HTT$_{ex1}$Q91-GFP in Or83b+ ORNs. RNA was isolated from
1136 heads of uninjured flies or flies 3 hours after bilateral antennal and maxillary palp nerve injury. Data are
1137 shown as mean ± s.e.m and normalized to the housekeeping gene *rpl32*. *p<0.05, **p<0.01, ***p<0.001
1138 by one-way ANOVA, asterisks and hashtags indicate statistical significance comparing -/+ injury or
1139 genotypes, respectively. (**B-G**) Confocal stacks of the antennal lobe from 7 day-old flies expressing (**B,**
1140 **D, & F**) HTT$_{ex1}$Q25- or (**C, E, & G**) HTT$_{ex1}$Q91-V5 in Or83b+ ORNs and endogenously-tagged (**B-C**)
1141 YRab10, (**D-E**) YRab5, or (**F-G**) YRab7 in all cells. Brains were immunostained using YFP (*green*), V5
1142 (*magenta*), and N-Cadherin (*blue*) antibodies. Segmented YRab+ or HTT+ surfaces are shown to the
1143 right of each set of raw fluorescent images. Insets show magnified YFP+ surfaces of interest from each
1144 image. Diffuse wtHTT$_{ex1}$ signal was adjusted post-acquisition for increased visibility in panels (**B, D,** and
1145 **F**). Scale bars = 10 μm. (**H-I**) Quantification of YRab+ surfaces (**H**) and YRab+ surfaces within 0.2μm of
1146 HTT$_{ex1}$+ surfaces (**I**). Data are shown as mean ± s.e.m.; *p<0.05, **p<0.01, ***p<0.001, ****p<0.0001 by
1147 unpaired two-tailed *t*-test.
1148
1149 **Figure 16. Association of neuronal mHTT aggregates with glial Rab GTPases that label early,**
1150 **maturing, and late phagosomes.** (**A-F**) Confocal stacks of the antennal lobe from 16-19 day-old flies

1151 expressing (**A, C, E**) HTT_{ex1}Q25- or (**B, D, F**) HTT_{ex1}Q91-V5 in Or83b+ ORNs together with (**A-B**) YFP-
1152 Rab10, (**C-D**) YFP-Rab5, or (**E-F**) YFP-Rab7 in repo+ glia. Brains were immunostained with anti-GFP
1153 to amplify YFP-Rab signals. Segmented Rab+ or HTT_{ex1}+ surfaces are shown to the right of each set of
1154 raw fluorescence images. Insets show magnified YFP-Rab+ surfaces of interest from each image.
1155 Diffuse wtHTT_{ex1} signal was adjusted post-acquisition for increased visibility in panels (**A, C,** and **E**).
1156 Scale bars = 10 μm. (**G-I**) Quantification of total YFP-Rab+ surfaces (**G**), YFP-Rab+ surfaces ≤0.2 μm
1157 from HTT_{ex1} surfaces (**H**), and mean YFP-Rab+ surface volume (**I**) in brains expressing HTT_{ex1}Q25- or
1158 HTT_{ex1}Q91-mCherry. The dark red bars in (**I**) represent YFP-Rab+ surfaces that co-localized with
1159 mHTT_{ex1}. All graphed data are shown as mean ± s.e.m.; *p<0.05, **p<0.01, ***p<0.001, ****p<0.0001
1160 by unpaired two-tailed *t*-test.
1161
1162 **Figure 17. Glial YFP-Rab+ surfaces are closely associated with neuronal mHTT_{ex1} aggregates**.
1163 High magnification confocal stacks showing examples of individual YFP+ surfaces within 0.2 μm of
1164 HTT_{ex1}Q91 aggregates from 21-22 day-old adult brains expressing HTT_{ex1}Q91-mCherry in Or83b+
1165 ORNs and YFP-Rab10 (**A1-3**), YFP-Rab5 (**B1-2**), or YFP-Rab7 (**C1-2**) in repo+ glia. Brains were
1166 immunostained with anti-GFP to amplify YFP-Rab signals. Scale bars = 1 μm.
1167
1168 **Figure 18. "Traffic jam" model illustrating effects of neuronal mHTT_{ex1} aggregates on phagocytic**
1169 **glia.** mHTT_{ex1} aggregates (*magenta circles*) generated in axons cause phagolysosomal defects in
1170 neighboring glial cells. Neuronal mHTT_{ex1} aggregates activate glial Draper and Toll-6 signaling
1171 pathways, but impair normal phagocytic responses to injury, including reduced nascent phagosome
1172 formation and decreased numbers of Rab5+ early phagosomes (*red arrow*). A buildup of engulfed
1173 mHTT_{ex1} aggregates in glia leads to accumulation of maturing (Rab10+ or Rab7+) phagosomes and
1174 lysosomes (LAMP1+) (*green arrows*), possibly further slowing Draper-dependent engulfment and early
1175 phagosome formation. Defective phagocytic clearance could enhance leak or ejection of some mHTT_{ex1}
1176 aggregates from phagolysosomes to increase their toxicity and capacity to seed soluble HTT proteins
1177 (*magenta + green circles*).

1178 **TABLE LEGENDS**

1179 **Table 1. *Drosophila* genotype and source information.**

1180

1181 **Table 2. Genotypes of flies used in all figures.**

1182

1183 **Table 3. Primer sequences used for qPCR analyses.**

1184

1185 **Table 4. Statistical information for all quantitative results.**

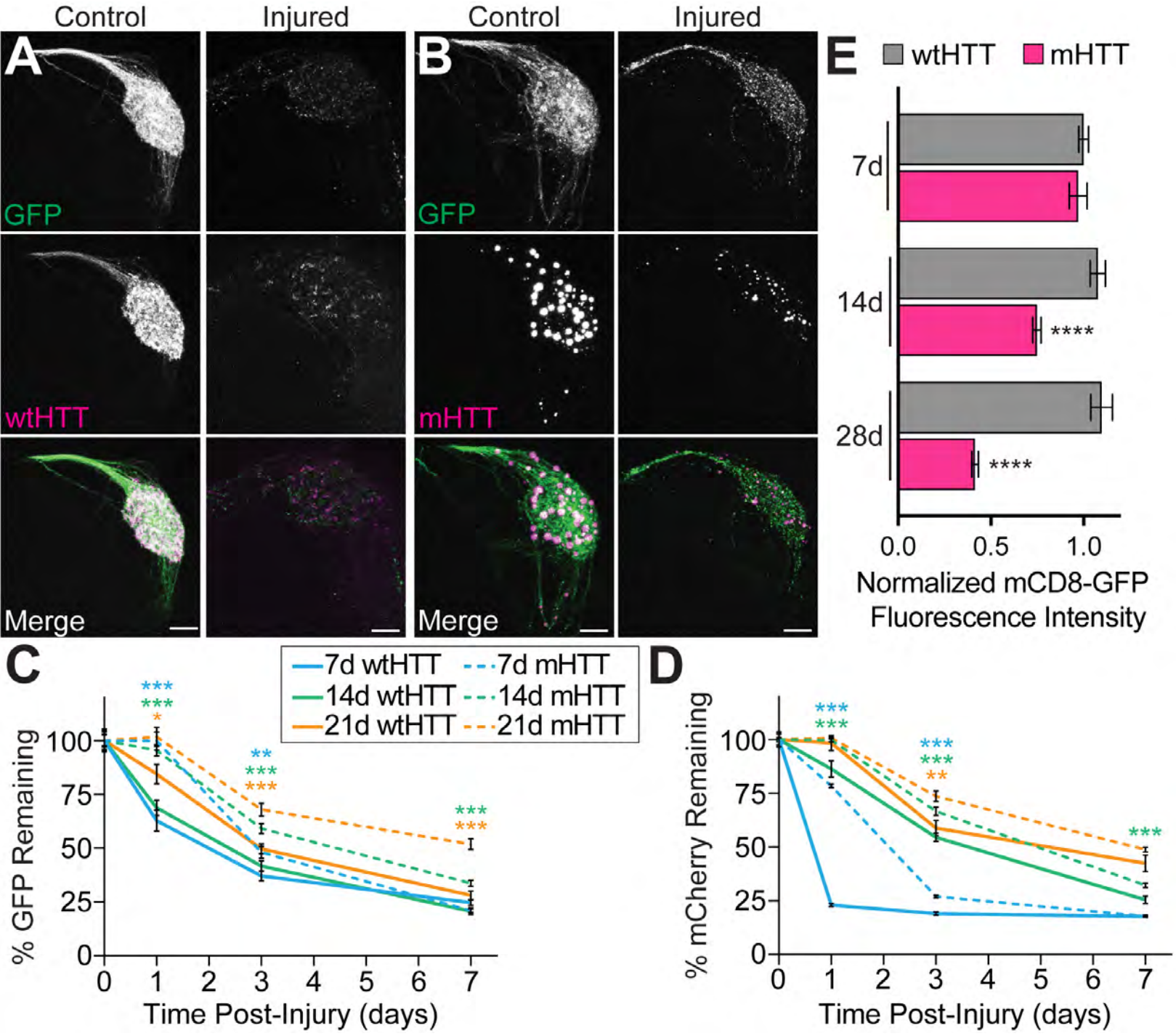
Control
Injured
Control
Injured
A
B
GFP
GFP
wtHTT
mHTT
Merge
Merge
E
wtHTT
mHTT
7d
14d
28d
****
****
0.0
0.5
1.0
Normalized mCD8-GFP Fluorescence Intensity
C
7d wtHTT
7d mHTT
14d wtHTT
14d mHTT
21d wtHTT
21d mHTT
% GFP Remaining
Time Post-Injury (days)
D
% mCherry Remaining
Time Post-Injury (days)

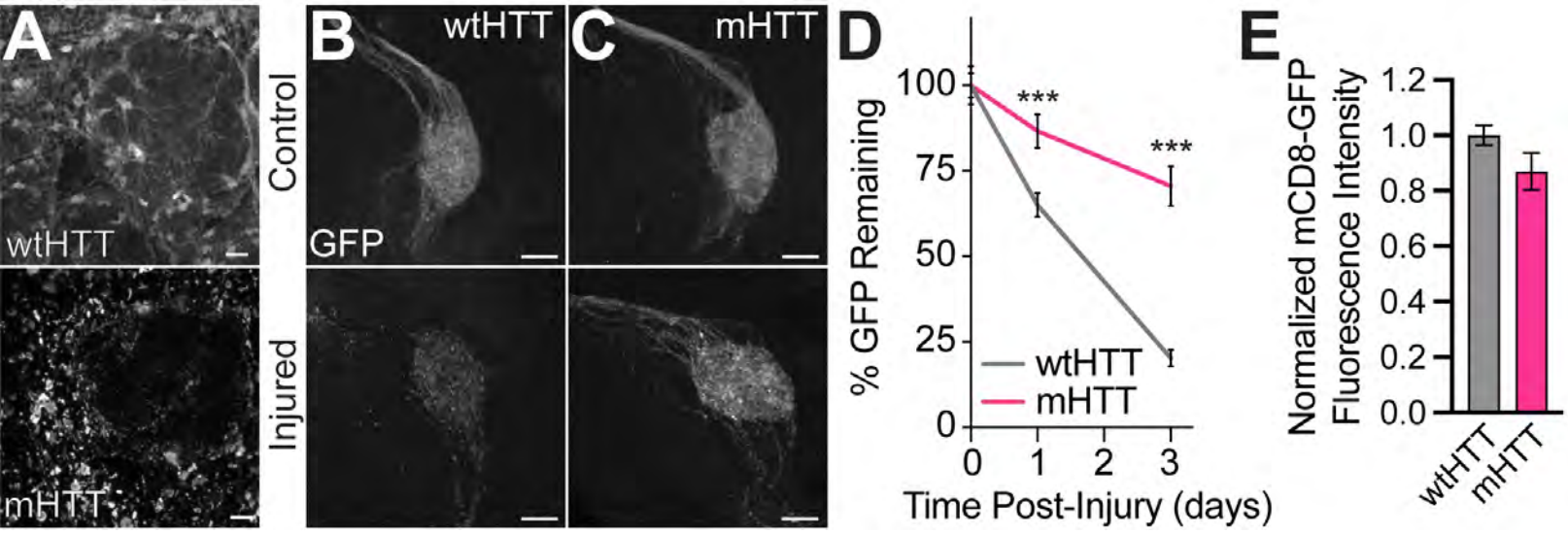
A
wtHTT
mHTT
B
wtHTT
C
mHTT
Control
Injured
GFP
D
% GFP Remaining
100
75
50
25
0
***
***
wtHTT
mHTT
0
1
2
3
Time Post-Injury (days)
E
Normalized mCD8-GFP Fluorescence Intensity
1.2
1.0
0.8
0.6
0.4
0.2
0.0
wtHTT
mHTT

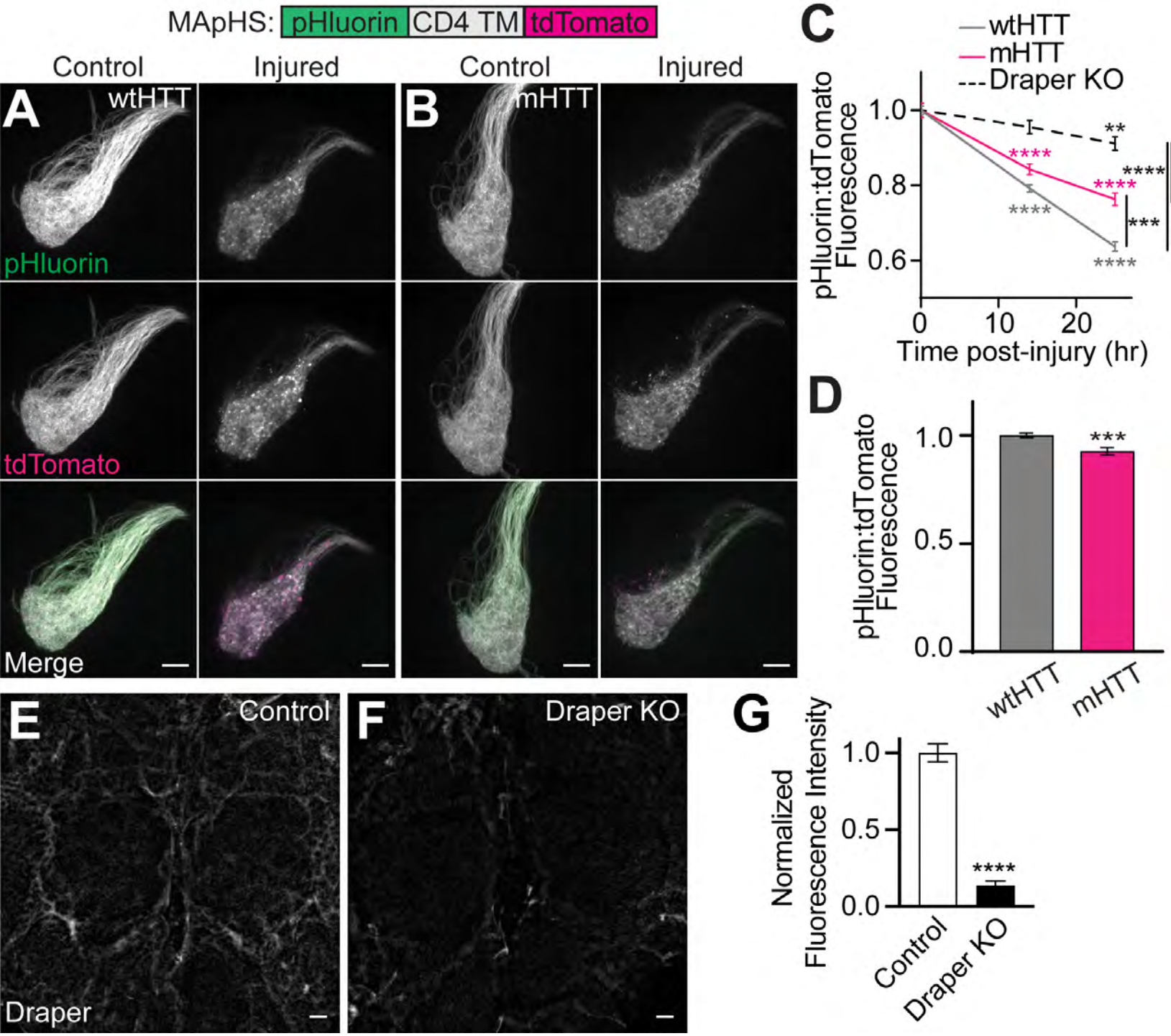
MApHS: pHluorin CD4 TM tdTomato
Control
Injured
Control
Injured
A
wtHTT
B
mHTT
pHluorin
tdTomato
Merge
C
wtHTT
mHTT
Draper KO
pHluorin:tdTomato Fluorescence
1.0
0.8
0.6
0
10
20
Time post-injury (hr)
**
****
****
****
****
***
****
D
pHluorin:tdTomato Fluorescence
1.0
0.5
0.0
***
wtHTT
mHTT
E
Control
Draper
F
Draper KO
G
Normalized Fluorescence Intensity
1.0
0.5
0.0
****
Control
Draper KO

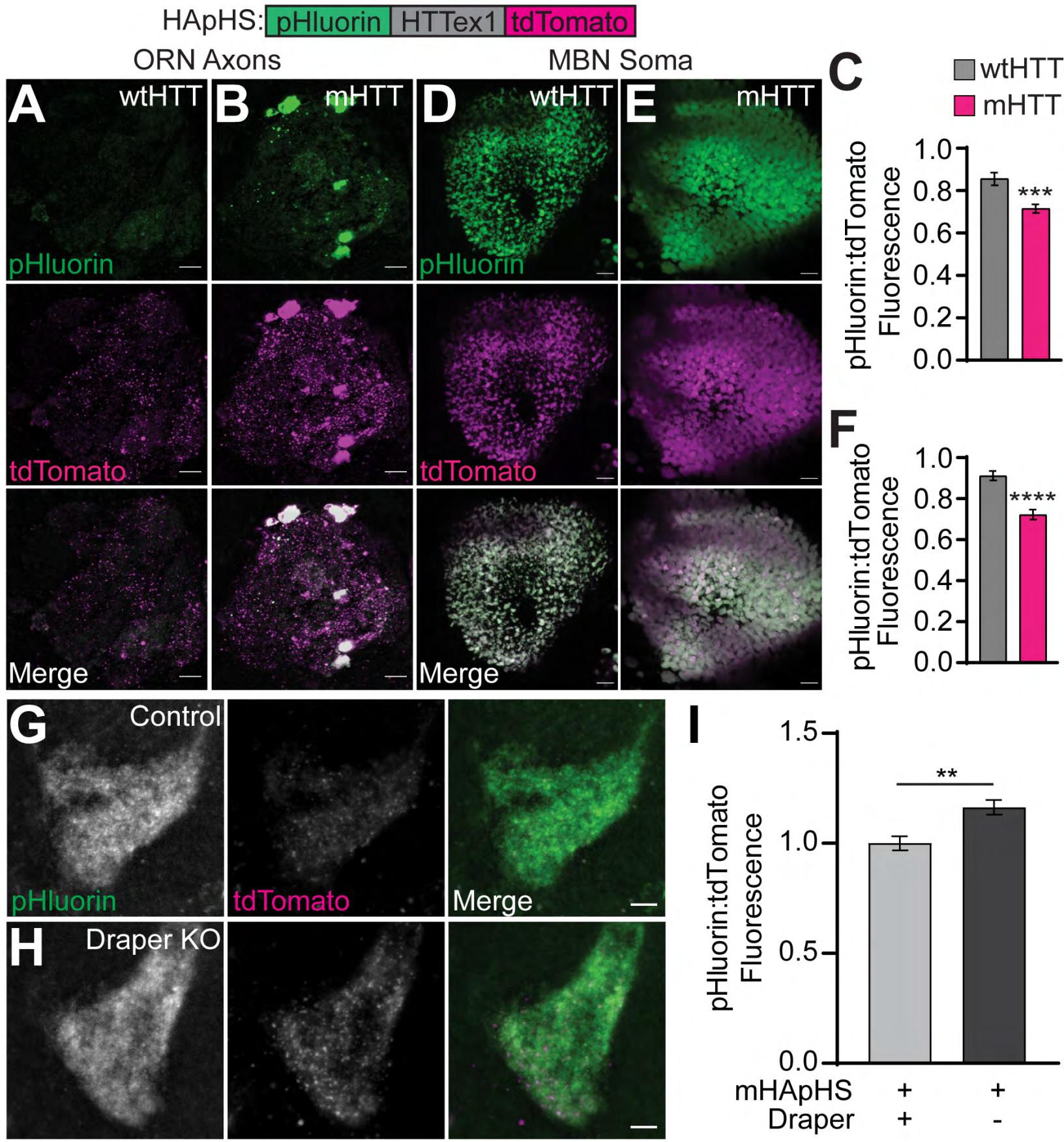
HApHS:
pHluorin
HTTex1
tdTomato
ORN Axons
MBN Soma
A
wtHTT
B
mHTT
D
wtHTT
E
mHTT
pHluorin
tdTomato
Merge
C
wtHTT
mHTT
pHluorin:tdTomato Fluorescence
1.0
0.8
0.6
0.4
0.2
0.0
***
F
****
G
Control
H
Draper KO
I
1.5
1.0
0.5
0.0
**
mHApHS + +
Draper + -

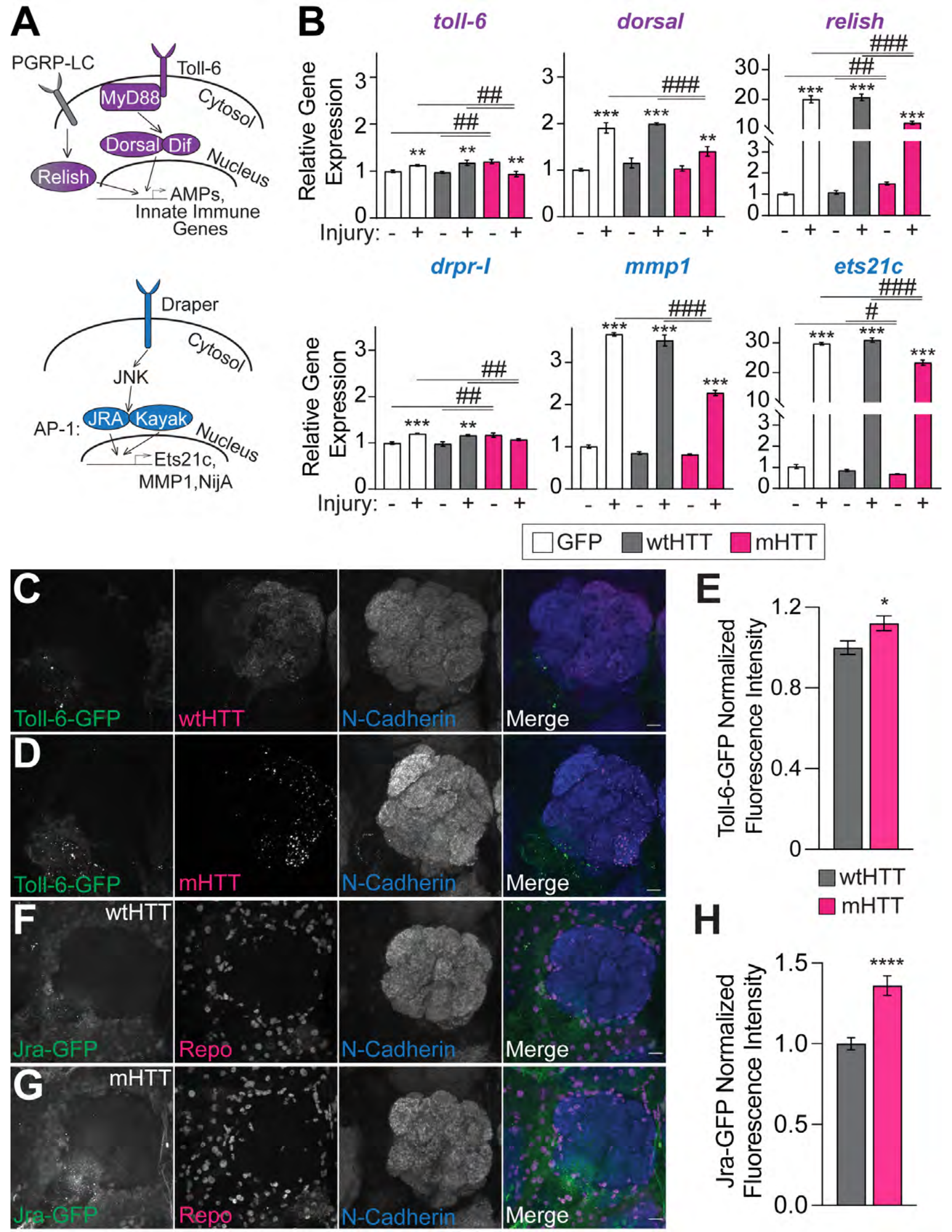
A
PGRP-LC
Toll-6
MyD88
Cytosol
Dorsal
Dif
Nucleus
Relish
AMPs,
Innate Immune
Genes
Draper
Cytosol
JNK
AP-1:
JRA
Kayak
Nucleus
Ets21c,
MMP1,NijA
B
toll-6
dorsal
relish
drpr-l
mmp1
ets21c
Relative Gene Expression
Injury: - + - + - +
GFP
wtHTT
mHTT
C
Toll-6-GFP
wtHTT
N-Cadherin
Merge
D
Toll-6-GFP
mHTT
N-Cadherin
Merge
E
Toll-6-GFP Normalized Fluorescence Intensity
wtHTT
mHTT
F
wtHTT
Jra-GFP
Repo
N-Cadherin
Merge
G
mHTT
Jra-GFP
Repo
N-Cadherin
Merge
H
Jra-GFP Normalized Fluorescence Intensity

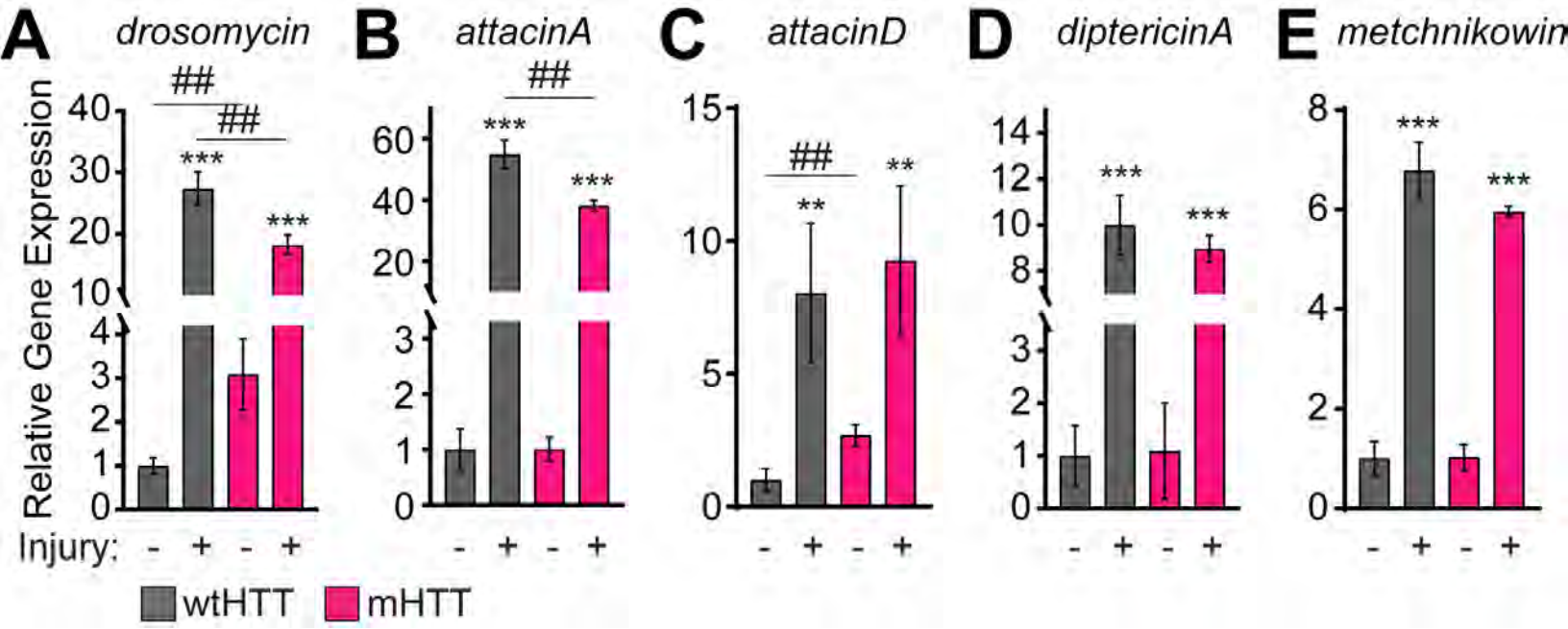
A
drosomycin
B
attacinA
C
attacinD
D
diptericinA
E
metchnikowin
Relative Gene Expression
##
***
**
Injury: - + - +
wtHTT
mHTT

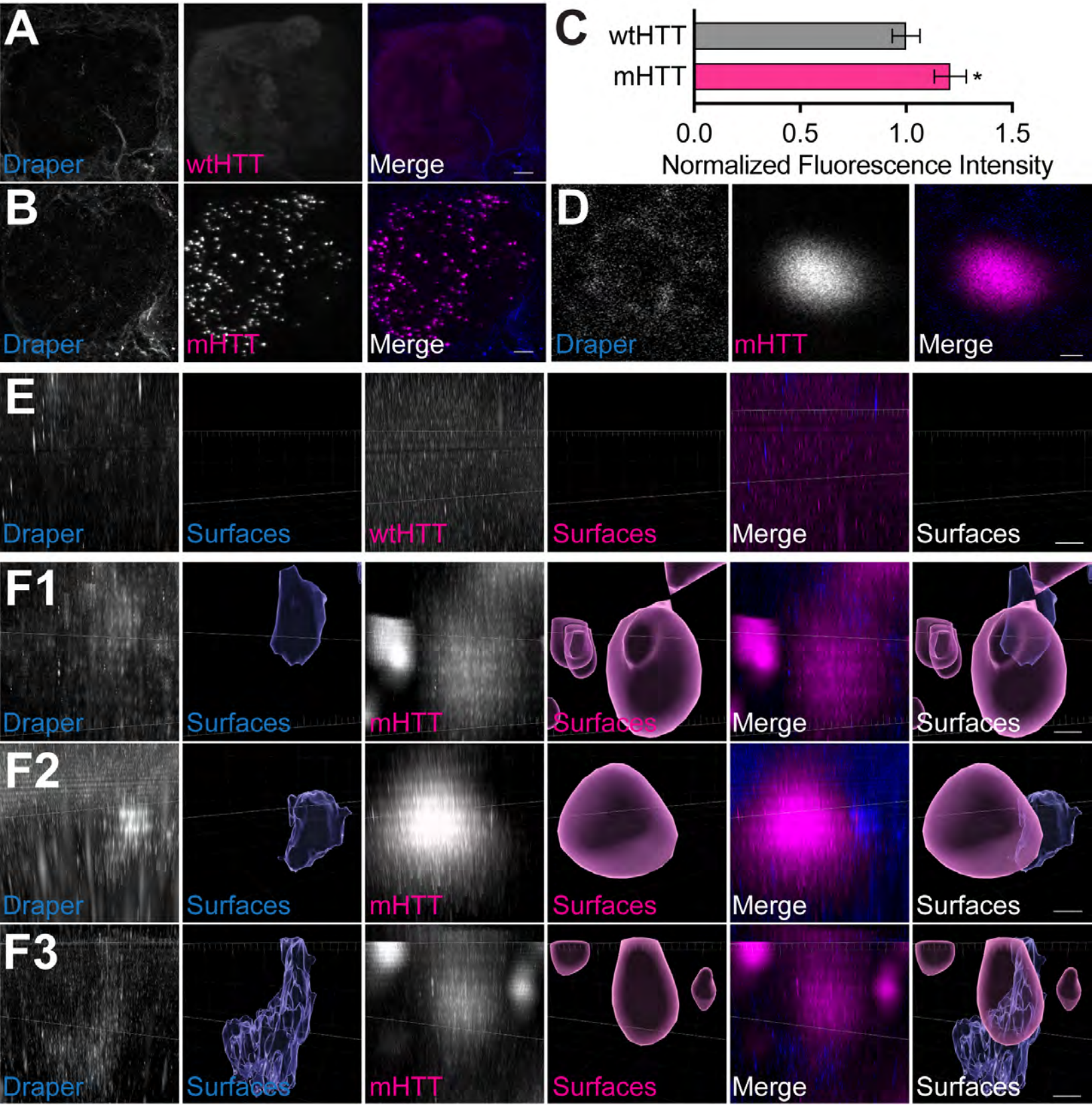
A
Draper
wtHTT
Merge
B
Draper
mHTT
Merge
C
wtHTT
mHTT
*
0.0
0.5
1.0
1.5
Normalized Fluorescence Intensity
D
Draper
mHTT
Merge
E
Draper
Surfaces
wtHTT
Surfaces
Merge
Surfaces
F1
Draper
Surfaces
mHTT
Surfaces
Merge
Surfaces
F2
Draper
Surfaces
mHTT
Surfaces
Merge
Surfaces
F3
Draper
Surfaces
mHTT
Surfaces
Merge
Surfaces

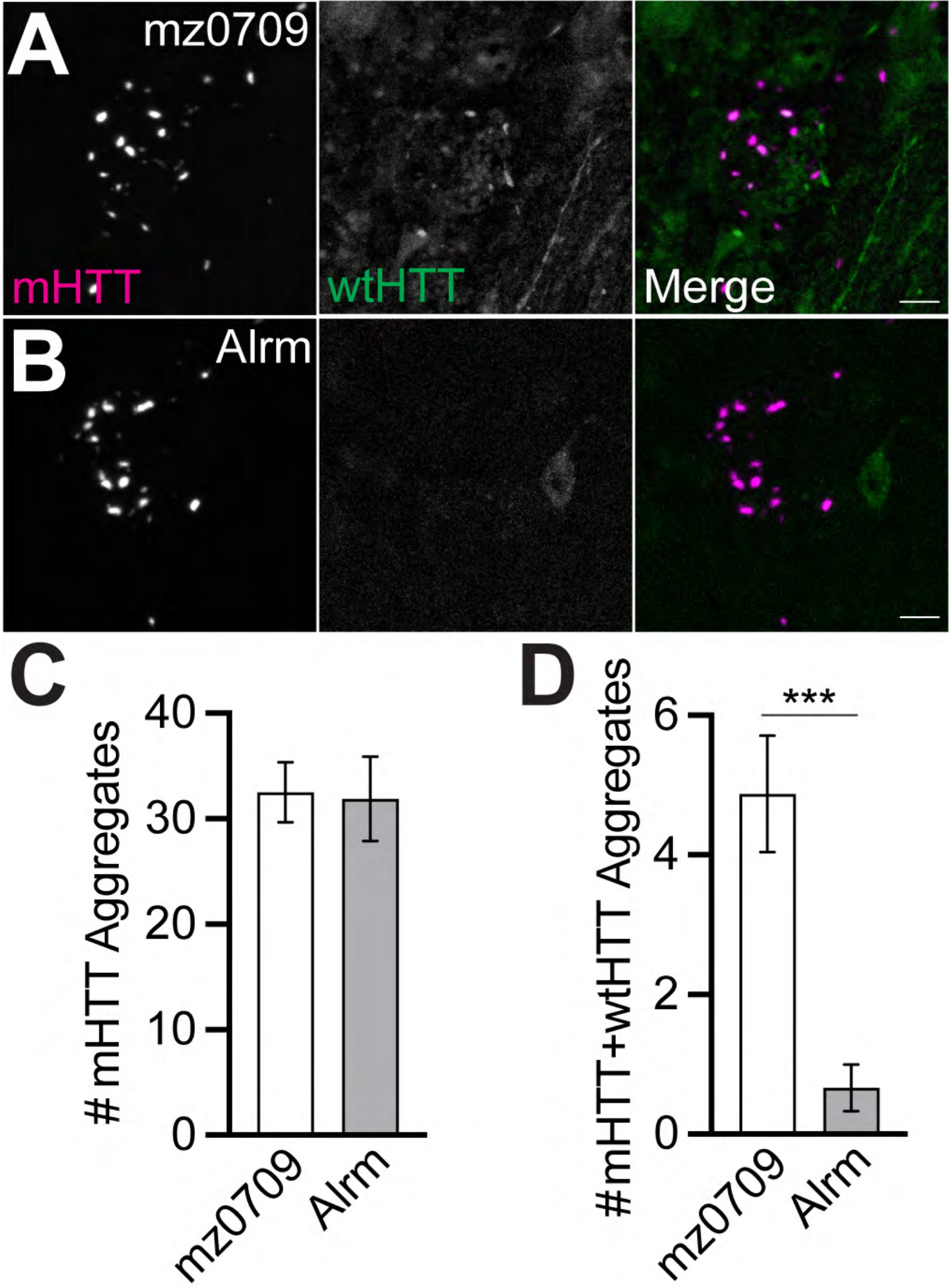
A
mz0709
mHTT
wtHTT
Merge
B
Alrm
C
mHTT Aggregates
40
30
20
10
0
mz0709
Alrm
D
#mHTT+wtHTT Aggregates
***
6
4
2
0
mz0709
Alrm

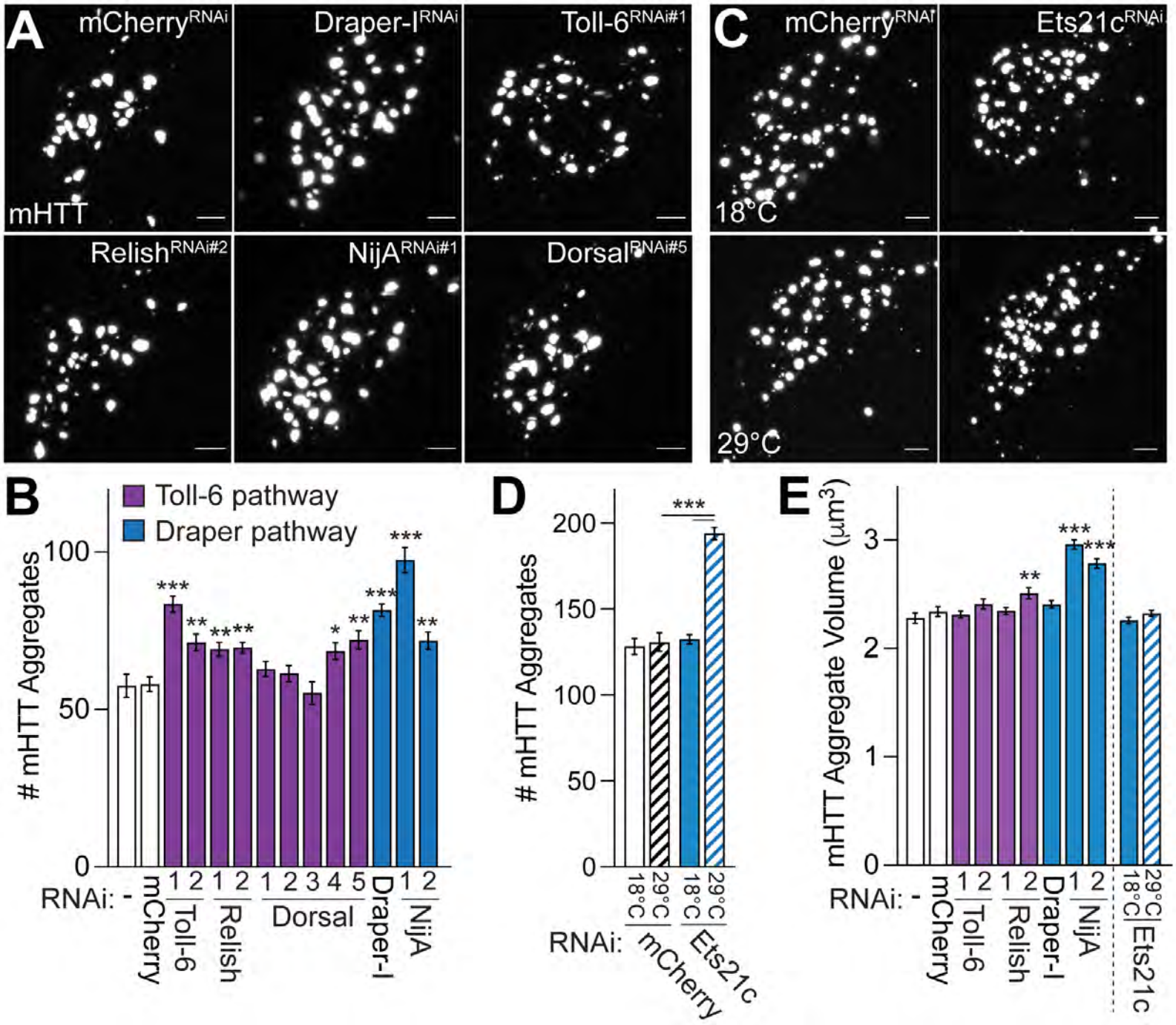
A
mCherry RNAi
Draper-I RNAi
Toll-6 RNAi#1
mHTT
Relish RNAi#2
NijA RNAi#1
Dorsal RNAi#5
C
mCherry RNAi
Ets21c RNAi
18°C
29°C
B
Toll-6 pathway
Draper pathway
mHTT Aggregates
RNAi: - mCherry Toll-6 1 2 Relish 1 2 Dorsal 1 2 3 4 5 Draper-I 1 2 NijA 1 2
D
mHTT Aggregates
RNAi: mCherry Ets21c
18°C 29°C 18°C 29°C
E
mHTT Aggregate Volume (μm³)
RNAi: - mCherry Toll-6 1 2 Relish 1 2 Draper-I 1 2 NijA 1 2 Ets21c 18°C 29°C

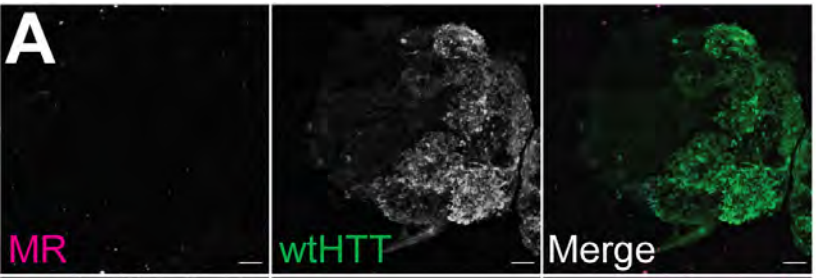
A
MR
wtHTT
Merge

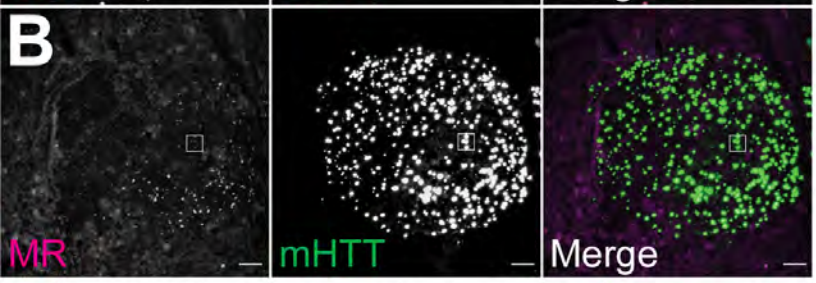
B
MR
mHTT
Merge

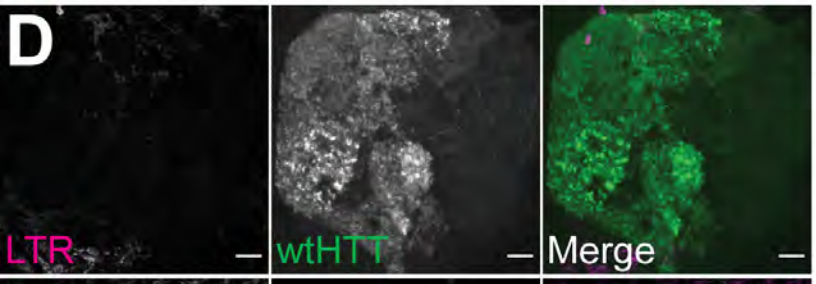
D
LTR
wtHTT
Merge

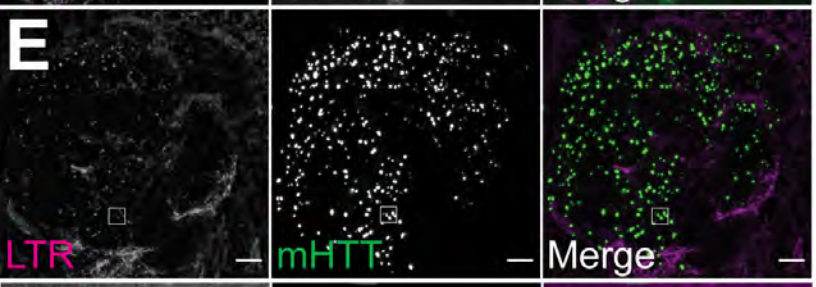
E
LTR
mHTT
Merge

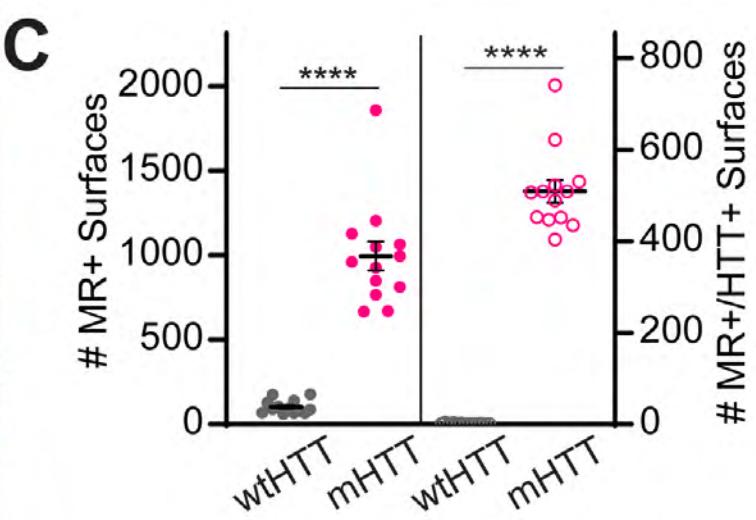
C
MR+ Surfaces
MR+/HTT+ Surfaces
2000
1500
1000
500
0
800
600
400
200
0
****
****
wtHTT
mHTT
wtHTT
mHTT

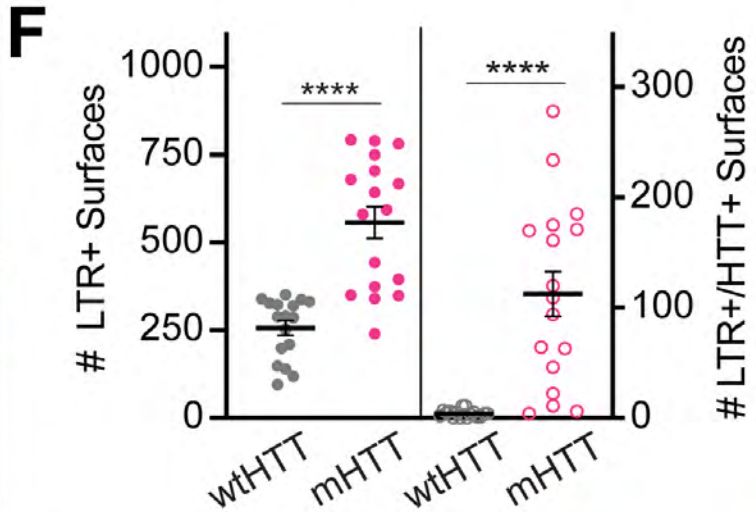
F
LTR+ Surfaces
LTR+/HTT+ Surfaces
1000
750
500
250
0
300
200
100
0
****
****
wtHTT
mHTT
wtHTT
mHTT

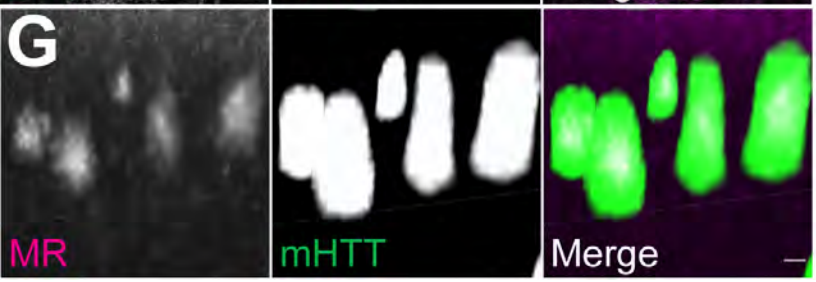
G
MR
mHTT
Merge

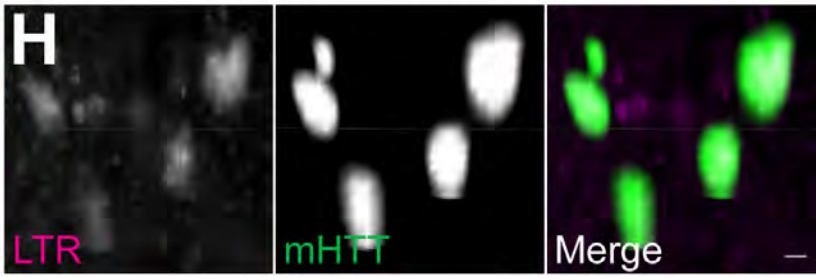
H
LTR
mHTT
Merge

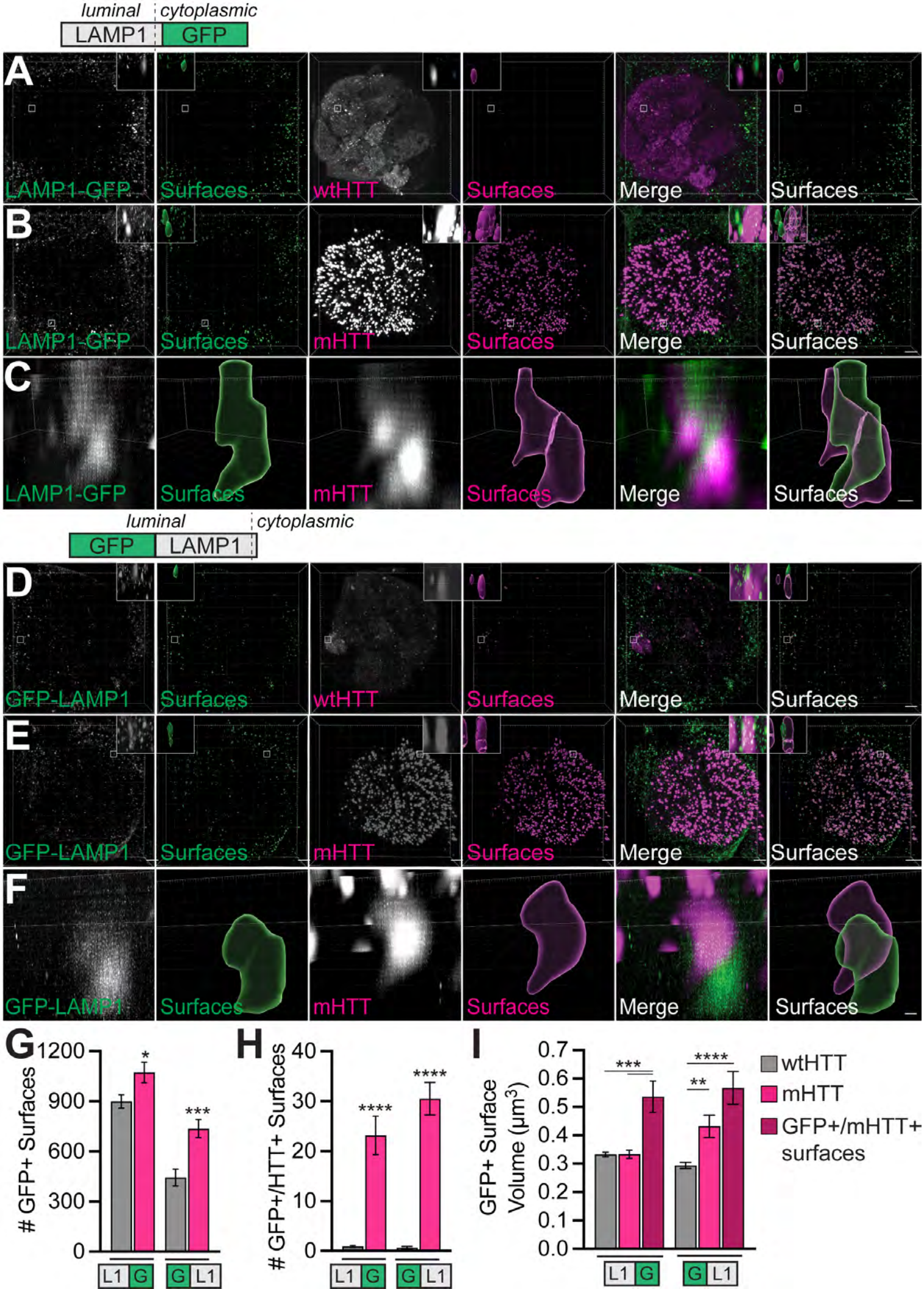
luminal
cytoplasmic
LAMP1
GFP
A
LAMP1-GFP
Surfaces
wtHTT
Surfaces
Merge
Surfaces
B
LAMP1-GFP
Surfaces
mHTT
Surfaces
Merge
Surfaces
C
LAMP1-GFP
Surfaces
mHTT
Surfaces
Merge
Surfaces
luminal
cytoplasmic
GFP
LAMP1
D
GFP-LAMP1
Surfaces
wtHTT
Surfaces
Merge
Surfaces
E
GFP-LAMP1
Surfaces
mHTT
Surfaces
Merge
Surfaces
F
GFP-LAMP1
Surfaces
mHTT
Surfaces
Merge
Surfaces
G
GFP+ Surfaces
1200
900
600
300
0
*
***
L1
G
G
L1
H
GFP+/HTT+ Surfaces
40
30
20
10
0
****
****
L1
G
G
L1
I
GFP+ Surface Volume (μm³)
0.7
0.6
0.5
0.4
0.3
0.2
0.1
0.0
***
****
**
L1
G
G
L1
wtHTT
mHTT
GFP+/mHTT+ surfaces

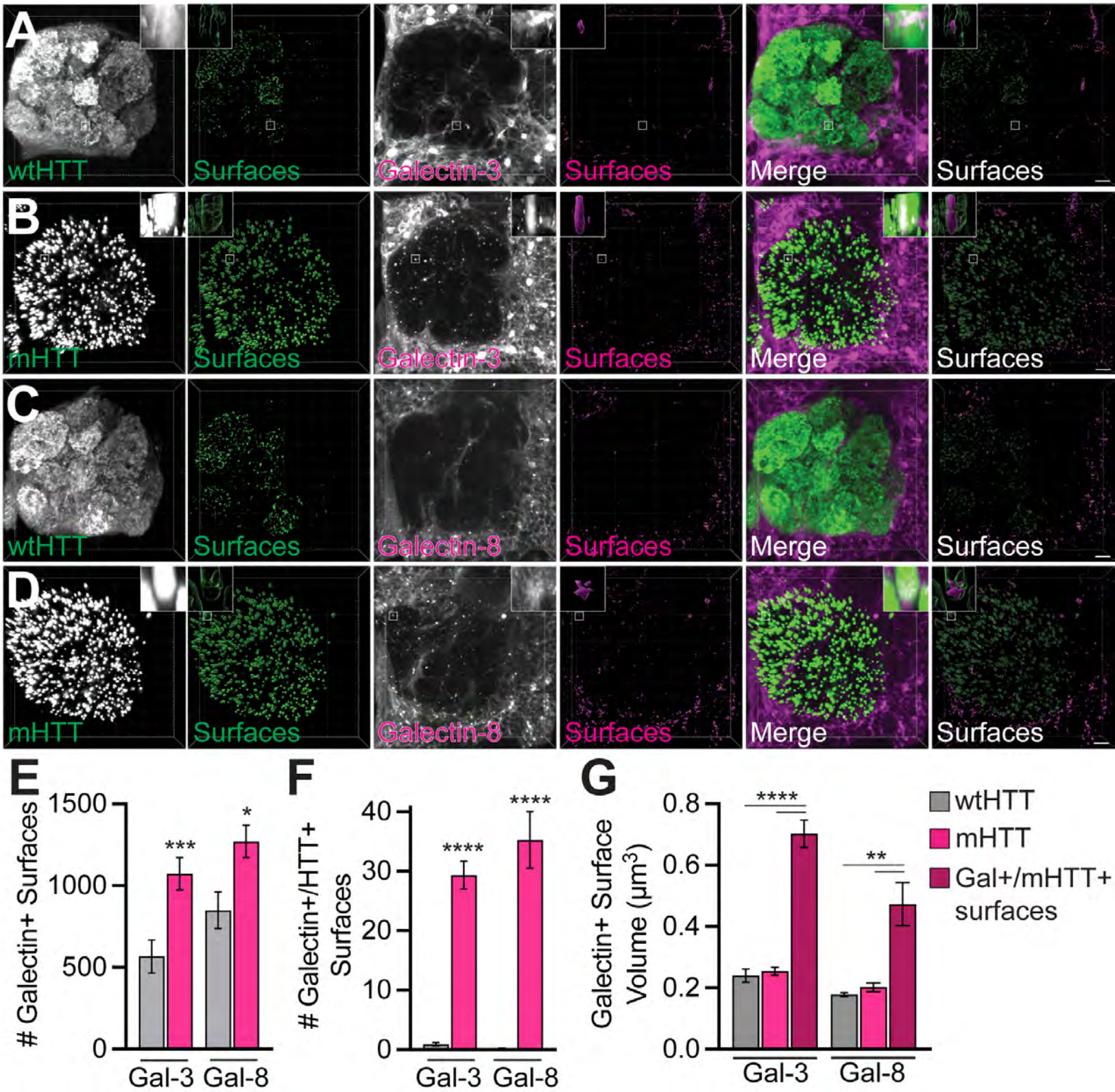
A
wtHTT
Surfaces
Galectin-3
Surfaces
Merge
Surfaces
B
mHTT
Surfaces
Galectin-3
Surfaces
Merge
Surfaces
C
wtHTT
Surfaces
Galectin-8
Surfaces
Merge
Surfaces
D
mHTT
Surfaces
Galectin-8
Surfaces
Merge
Surfaces
E
Galectin+ Surfaces
1500
1000
500
0
***
*
Gal-3
Gal-8
F
Galectin+/HTT+ Surfaces
40
30
20
10
0
****
****
Gal-3
Gal-8
G
Galectin+ Surface Volume (μm3)
0.8
0.6
0.4
0.2
0.0
****
**
Gal-3
Gal-8
wtHTT
mHTT
Gal+/mHTT+ surfaces

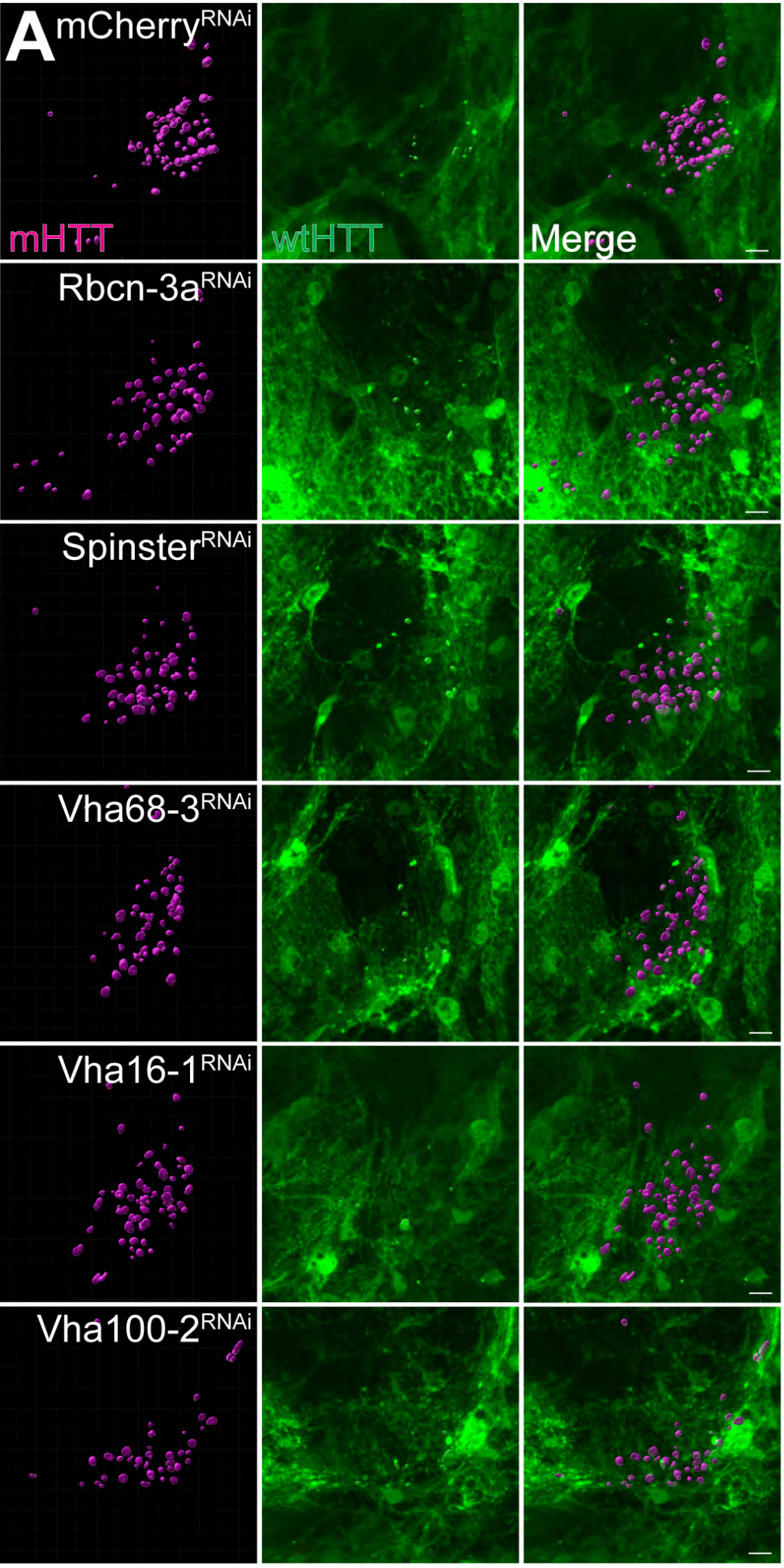
A
mCherryRNAi
mHTT
wtHTT
Merge
Rbcn-3aRNAi
SpinsterRNAi
Vha68-3RNAi
Vha16-1RNAi
Vha100-2RNAi

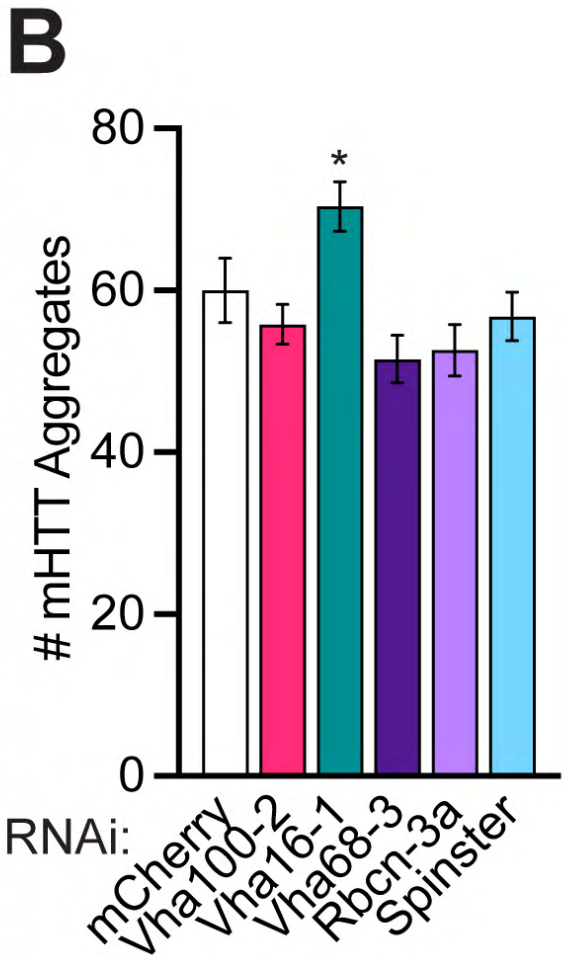
B
mHTT Aggregates
80
60
40
20
0
*
RNAi:
mCherry
Vha100-2
Vha16-1
Vha68-3
Rbcn-3a
Spinster

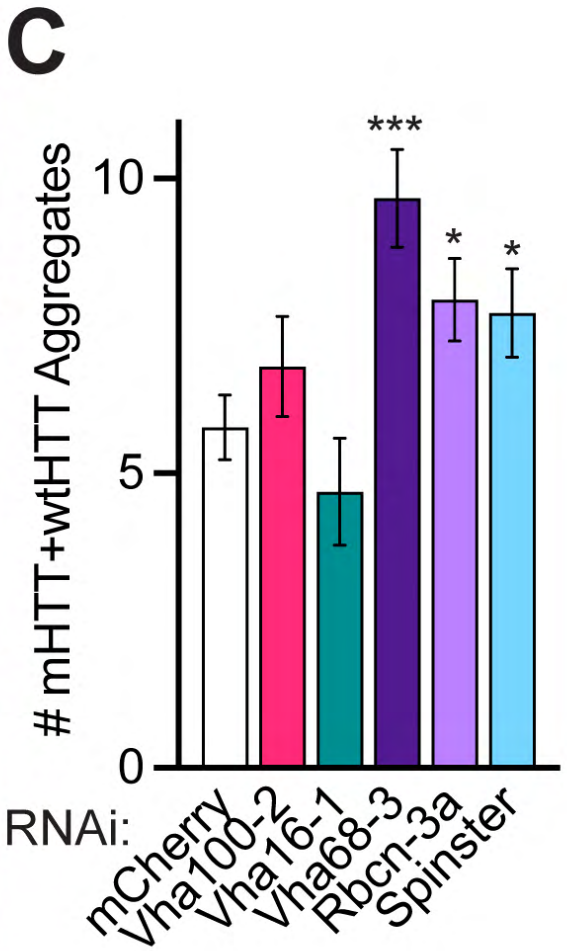
C
mHTT+wtHTT Aggregates
10
5
0
***
*
*
RNAi:
mCherry
Vha100-2
Vha16-1
Vha68-3
Rbcn-3a
Spinster

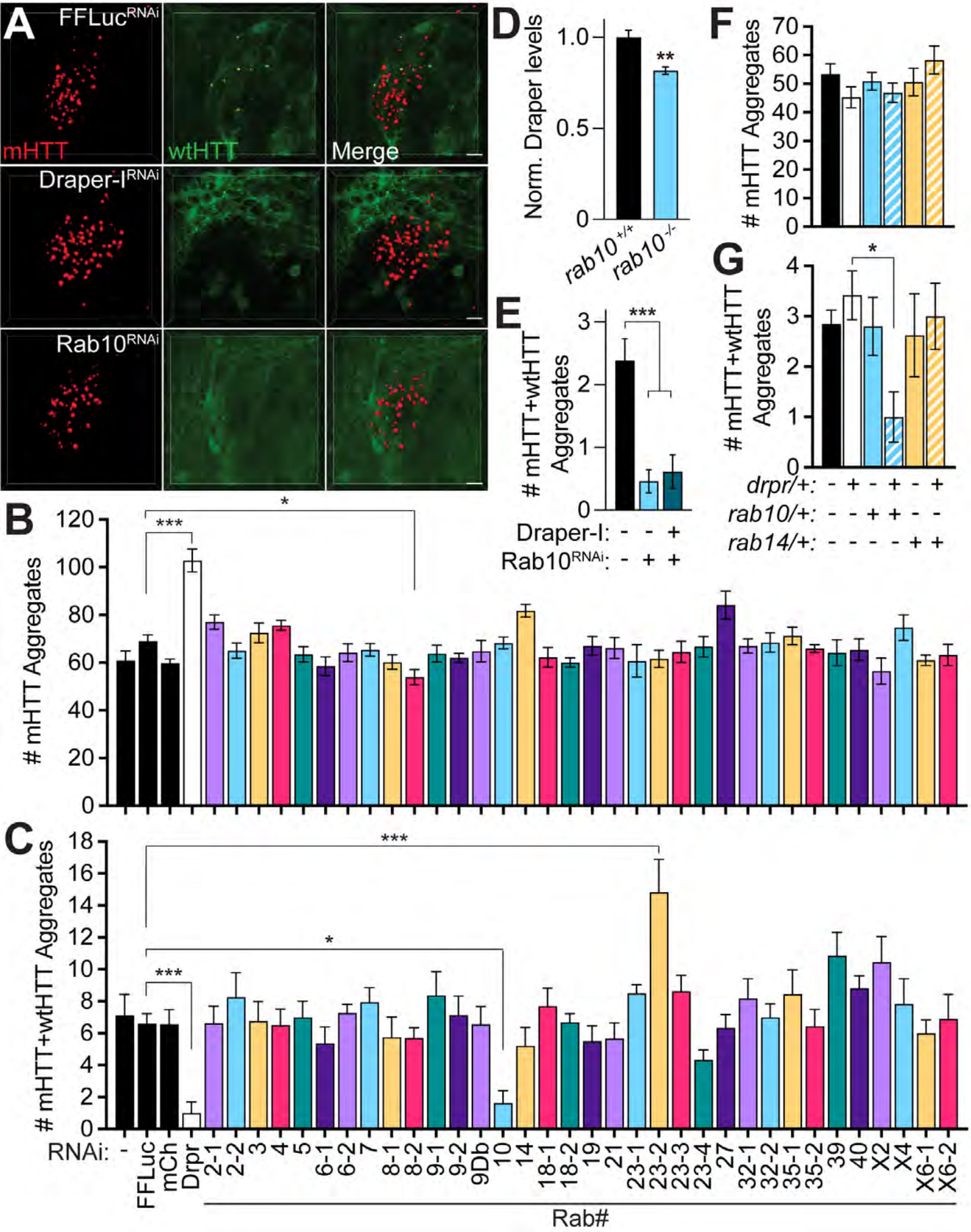
A
FFLuc^RNAi
mHTT
wtHTT
Merge
Draper-I^RNAi
Rab10^RNAi
D
Norm. Draper levels
1.0
0.5
0
**
rab10^+/+
rab10^-/-
F
mHTT Aggregates
70
60
50
40
30
20
10
0
E
mHTT+wtHTT Aggregates
3
2
1
0
***
Draper-I: - - +
Rab10^RNAi: - + +
G
mHTT+wtHTT Aggregates
4
3
2
1
0
*
drpr/+: - + - + - +
rab10/+: - - + + - -
rab14/+: - - - - + +
B
mHTT Aggregates
120
100
80
60
40
20
0
*
***
C
mHTT+wtHTT Aggregates
18
16
14
12
10
8
6
4
2
0
***
*
***
RNAi: - FFLuc mCh Drpr 2-1 2-2 3 4 5 6-1 6-2 7 8-1 8-2 9-1 9-2 9Db 10 14 18-1 18-2 19 21 23-1 23-2 23-3 23-4 27 32-1 32-2 35-1 35-2 39 40 X2 X4 X6-1 X6-2
Rab#

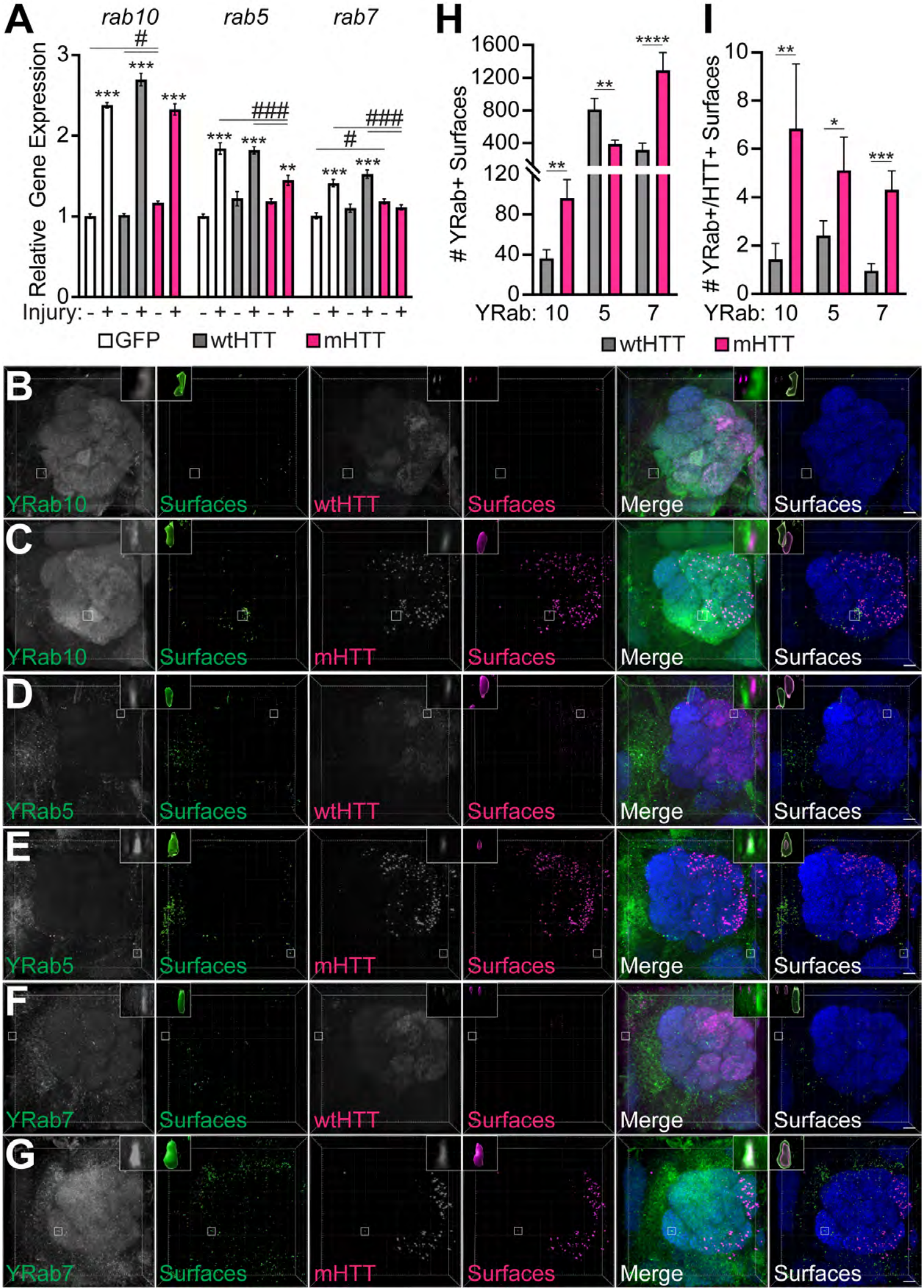
A
rab10
rab5
rab7
Relative Gene Expression
Injury: - + - + - + - + - + - + - + - + - + - +
GFP
wtHTT
mHTT
H
YRab+ Surfaces
YRab: 10 5 7
wtHTT
mHTT
I
YRab+/HTT+ Surfaces
YRab: 10 5 7
B
YRab10
Surfaces
wtHTT
Surfaces
Merge
Surfaces
C
YRab10
Surfaces
mHTT
Surfaces
Merge
Surfaces
D
YRab5
Surfaces
wtHTT
Surfaces
Merge
Surfaces
E
YRab5
Surfaces
mHTT
Surfaces
Merge
Surfaces
F
YRab7
Surfaces
wtHTT
Surfaces
Merge
Surfaces
G
YRab7
Surfaces
mHTT
Surfaces
Merge
Surfaces

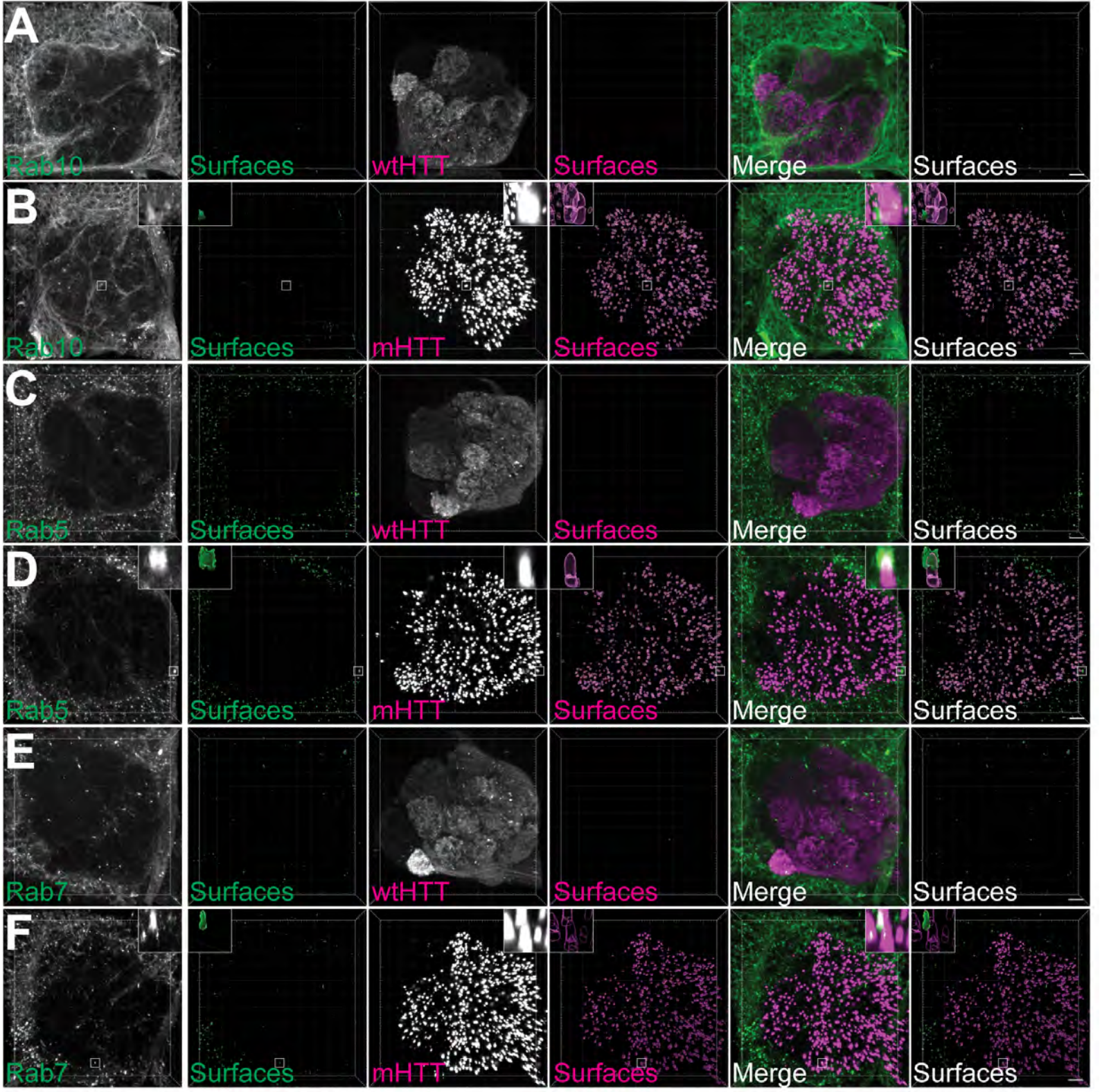
A
Rab10
Surfaces
wtHTT
Surfaces
Merge
Surfaces
B
Rab10
Surfaces
mHTT
Surfaces
Merge
Surfaces
C
Rab5
Surfaces
wtHTT
Surfaces
Merge
Surfaces
D
Rab5
Surfaces
mHTT
Surfaces
Merge
Surfaces
E
Rab7
Surfaces
wtHTT
Surfaces
Merge
Surfaces
F
Rab7
Surfaces
mHTT
Surfaces
Merge
Surfaces

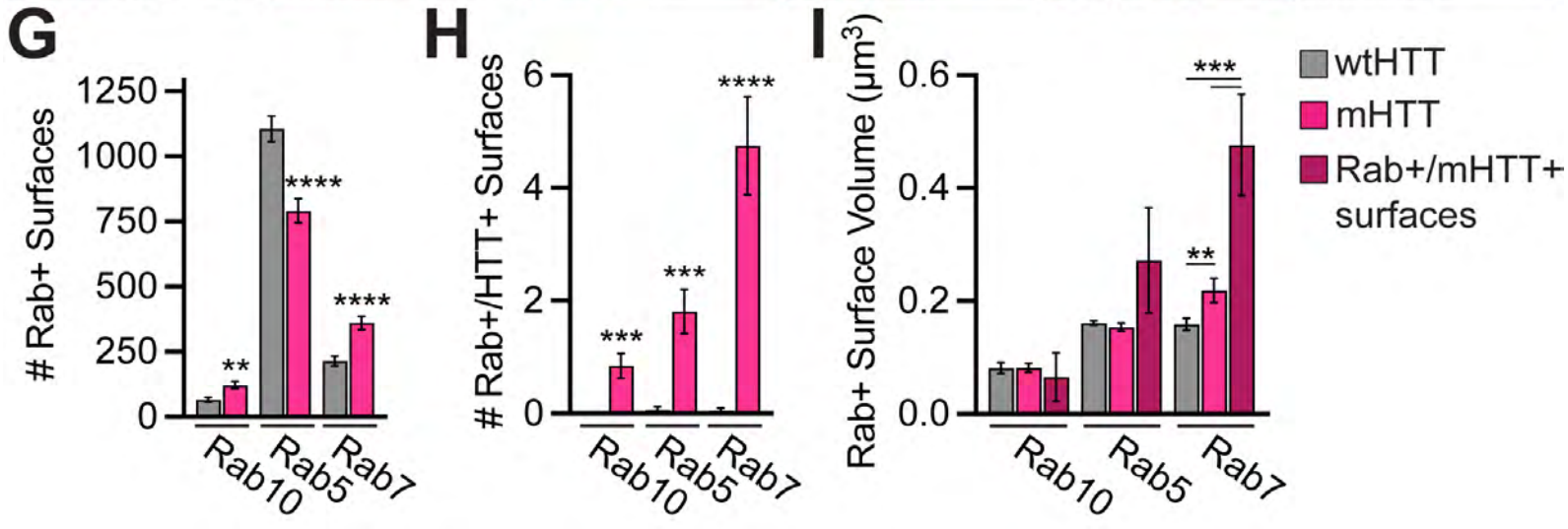
G
Rab+ Surfaces
1250
1000
750
500
250
0
**
****
****
Rab10
Rab5
Rab7
H
Rab+/HTT+ Surfaces
6
4
2
0
***
***
****
Rab10
Rab5
Rab7
I
Rab+ Surface Volume (μm³)
0.6
0.4
0.2
0.0
***
**
Rab10
Rab5
Rab7
wtHTT
mHTT
Rab+/mHTT+ surfaces

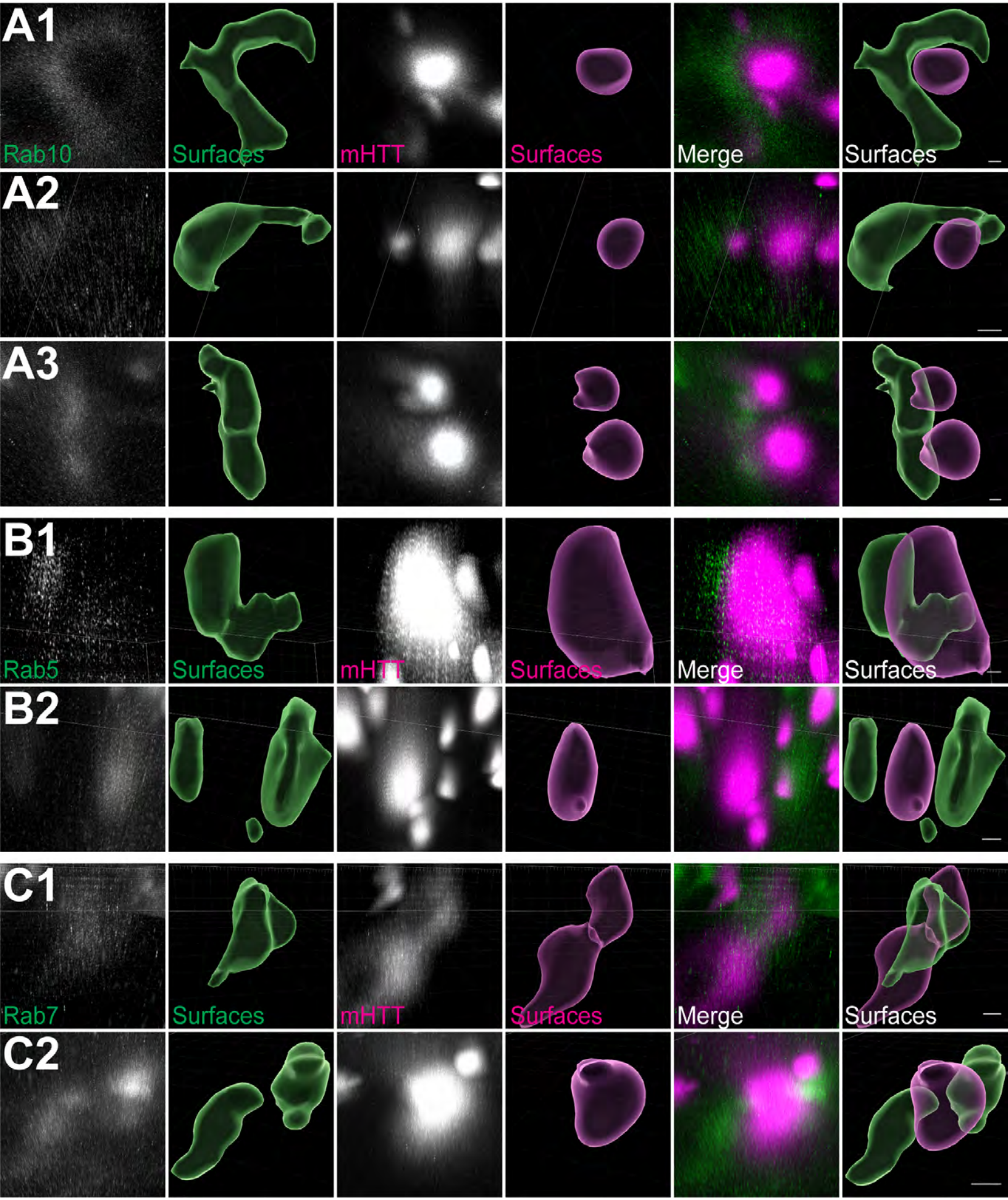
A1
Rab10
Surfaces
mHTT
Surfaces
Merge
Surfaces
A2
A3
B1
Rab5
Surfaces
mHTT
Surfaces
Merge
Surfaces
B2
C1
Rab7
Surfaces
mHTT
Surfaces
Merge
Surfaces
C2

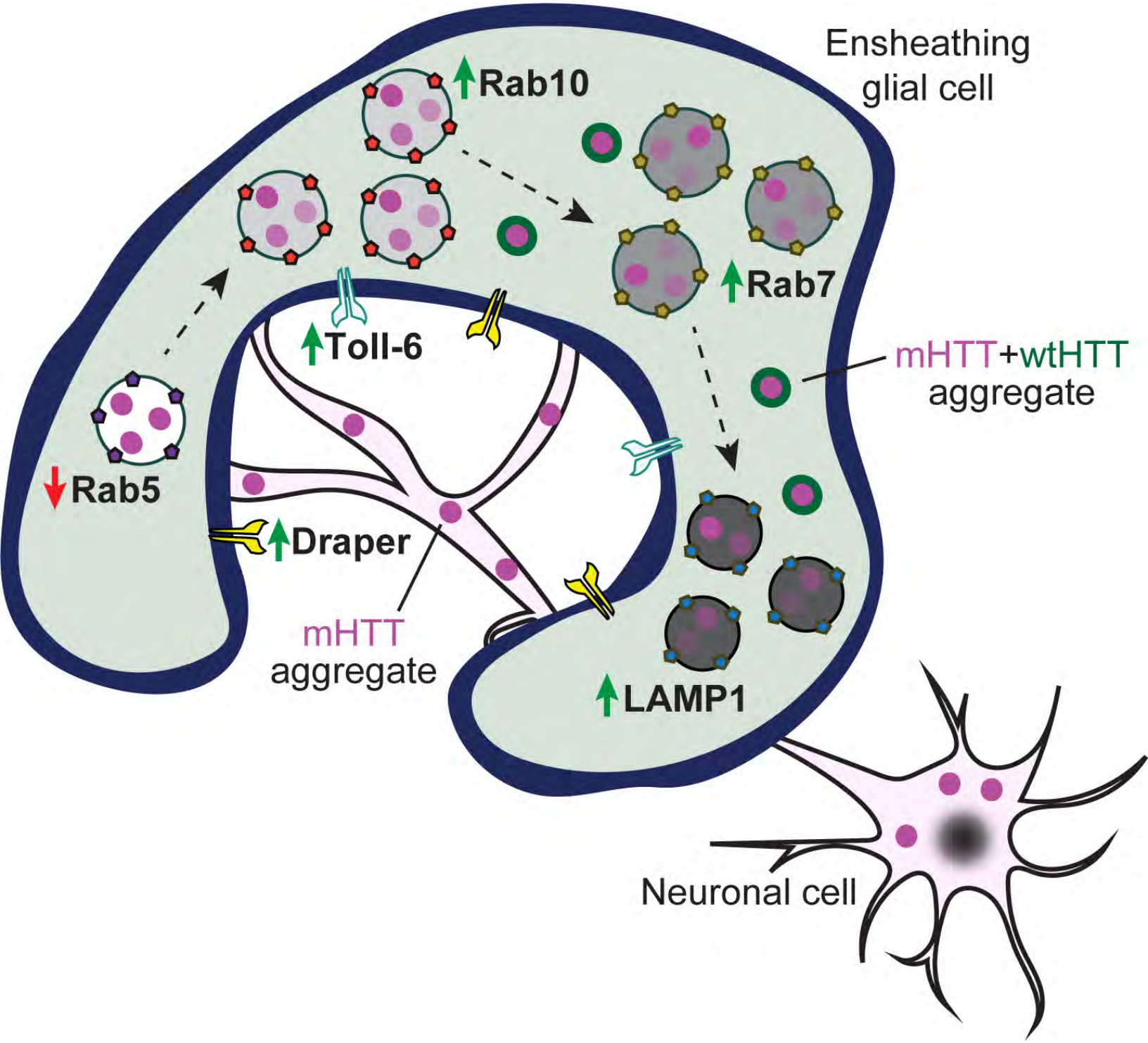
Ensheathing
glial cell
Rab10
Rab7
Toll-6
mHTT+wtHTT
aggregate
Rab5
Draper
mHTT
aggregate
LAMP1
Neuronal cell

Table 1. *Drosophila* genotype and source information.

Name	ID (if available)	Reference	Notes
Or67d-QF		Liang et al., 2013	
repo-Gal4	RRID:BDSC_7415	Sepp et al., 2001	
mz0709-Gal4		Ito et al., 1995	a gift from Marc Freeman (Vollum Institute)
alrm-Gal4	RRID:BDSC_67032		
orco-Gal4	RRID:BDSC_23292		
Or47b-Gal4	RRID:BDSC_9983		
QUAS-HTT$_{ex1}$Q25-mCherry^{attP24}		Donnelly et al., 2020	
QUAS-HTT$_{ex1}$Q91-mCherry^{attP24}		Donnelly et al., 2020	
QUAS-HTT$_{ex1}$Q91-mCherry^{attP3}		Donnelly et al., 2020	
QUAS-HTT$_{ex1}$Q91-mCherry$^{suHw(attP8)}$		This study	
UAS-HTT$_{ex1}$Q25-GFP		Donnelly et al., 2020	
UAS-HTT$_{ex1}$Q91-GFP		Donnelly et al., 2020	
UAS-GFP		Donnelly et al., 2020	
QUAS-HTT$_{ex1}$Q25-GFP		This study	
QUAS-HTT$_{ex1}$Q91-GFP		This study	
UAS-mCherry-LGals3		This study	
UAS-mCherry-LGals8		This study	
QUAS-HTT$_{ex1}$Q25-V5		This study	
QUAS-HTT$_{ex1}$Q91-V5		This study	
UAS-pHluorin-HTT$_{ex1}$Q25-tdTomato		This study	
UAS-pHluorin-HTT$_{ex1}$Q91-tdTomato		This study	
UAS-mCD8-GFP	RRID:BDSC_5137		

UAS-Draper^{RNAi}		Logan et al., 2012	a gift from Marc Freeman (Vollum Institute)
tubP-Gal80^{ts}	RRID:BDSC_7017		
UAS-Drs^{RNAi}	RRID:BDSC_55391		
UAS-PGRP-SA^{RNAi}	RRID:BDSC_60037		
UAS-MMP1^{RNAi}	RRID:BDSC_31489		
UAS-ets21c^{RNAi}	RRID:BDSC_39069		
UAS-mCherry^{RNAi}	RRID:BDSC_35785		
UAS-rel^{RNAi}	RRID:BDSC_33661, RRID BDSC_28943		
UAS-dl^{RNAi}	RRID:BDSC_38905, RRID:BDSC_32934, RRID:BDSC_34938, RRID:BDSC_27650, RRID:BDSC_36650		
UAS-NinjurinA^{RNAi}	RRID:BDSC_50632 RRID:BDSC_51358		
UAS-Toll-6^{RNAi}	RRID:BDSC_56048, RRID:BDSC_64968		
Orco-QF2	RRID:BDSC_91997		
TI{TI}Rab10^{YFP}	RRID:BDSC_62548		
TI{TI}Rab5^{YFP}	RRID:BDSC_62543		
TI{TI}Rab7^{YFP}	RRID:BDSC_62545		
UAS-MApHS		Han et al., 2014	a gift from Chun Han (Cornell University)
Repo-Cas9[6A]		Koreman et al., 2021	a gift from Chun Han (Cornell University)
gRNA-drpr(BR)		Sapar et al., 2018	a gift from Chun Han (Cornell University)
Jra-GFP.FLAG	RRID:BDSC_50755		
OK107-Gal4			
UAS-GFP-LAMP1		Pulipparacharuvil et al., 2005	A gift from Helmut Kramer (UT Southwestern)

UAS-LAMP1-GFP	RRID:BDSC_42714		*nSyb-Gal4* was removed from stock
UAS-Rbcn-3a^{RNAi}	RRID:BDSC_34612		
UAS-Spinster^{RNAi}	RRID:BDSC_27702		
UAS-Vha100-2^{RNAi}	RRID:BDSC_64859		
UAS-Vha16-1^{RNAi}	RRID:BDSC_40923		
UAS-Vha68-3^{RNAi}	RRID:BDSC_42954		
UAS-YFP-Rab5	RRID:BDSC_9775		
UAS-YFP-Rab7	RRID:BDSC_23641		
UAS-YFP-Rab10	RRID:BDSC_24097		
UAS-YFP-Rab10 (T23N)	RRID:BDSC_9788		
UAS-YFP-Rab10 (Q68L)	RRID:BDSC_23259		
UAS-Rab7^{RNAi}	RRID:BDSC_27051		
UAS-Rab10^{RNAi}	RRID:BDSC_26289		
UAS-Rab2^{RNAi}	RRID:BDSC_28701 RRID:BDSC_34922		
UAS-Rab6^{RNAi}	RRID:BDSC_27490 RRID:BDSC_35744		
UAS-Rab11^{RNAi}	RRID:BDSC_27730		
UAS-Rab3^{RNAi}	RRID:BDSC_34655		
UAS-Rab14^{RNAi}	RRID:BDSC_28708		
UAS-Rab4^{RNAi}	RRID:BDSC_33757		
UAS-Rab5^{RNAi}	RRID:BDSC_30518		
UAS-Rab8^{RNAi}	RRID:BDSC_27519 RRID:BDSC_34373		
UAS-Rab9^{RNAi}	RRID:BDSC_42942 RRID:BDSC_34374		
UAS-luciferase^{RNAi}	RRID:BDSC_31603		
UAS-Rab9Db^{RNAi}	RRID:BDSC_38269		
UAS-Rab32^{RNAi}	RRID:BDSC_38956 RRID:BDSC_28002		

UAS-Rab18^{RNAi}	RRID:BDSC_34734 RRID:BDSC_27665		
UAS-RabX4^{RNAi}	RRID:BDSC_44070		
UAS-Rab27^{RNAi}	RRID:BDSC_50537		
UAS-RabX2^{RNAi}	RRID:BDSC_53928		
UAS-Rab39^{RNAi}	RRID:BDSC_53995		
UAS-Rab23^{RNAi}	RRID:BDSC_55352 RRID:BDSC_63689 RRID:BDSC_36091 RRID:BDSC_28025		
UAS-Rab35^{RNAi}	RRID:BDSC_67952 RRID:BDSC_80457		
UAS-Rab40^{RNAi}	RRID:BDSC_80472		
UAS-RabX6^{RNAi}	RRID:BDSC_26281 RRID:BDSC_53252		
UAS-Rab19^{RNAi}	RRID:BDSC_34607		
UAS-Rab21^{RNAi}	RRID:BDSC_29403		
UAS-Rab27^{RNAi}	RRID:BDSC_35774		
UAS-Draper-I		Logan et al., 2012	a gift from Marc Freeman (Vollum Institute)
Rab10(CRISPR-KO)		Kohrs et al., 2021	a gift from P. Robin Heisinger (Freie Universität Berlin)

Table 2. Genotypes of flies used in all figures.

Figure	Genotype
Figure 1A & C-E	*Or67d-QF/Y;QUAS-HTT$_{ex1}$Q25-mCherry/QUAS-mCD8-GFP*
Figure 1B-E	*Or67d-QF/Y;QUAS-HTT$_{ex1}$Q91-mCherry/QUAS-mCD8-GFP*
Figure 2A,D-E	*Or67d-QF/Y;UAS-HTT$_{ex1}$Q25-V5/QUAS-mCD8-GFP;repo-gal4/+*
Figure 2B,D-E	*Or67d-QF/Y;UAS-HTT$_{ex1}$Q91-V5/QUAS-mCD8-GFP;repo-gal4/+*
Figure 2C	*+/Y;UAS-HTT$_{ex1}$Q25-V5/+;repo-gal4/+ & +/Y;UAS-HTT$_{ex1}$Q91-V5/+;repo-gal4/+*
Figure 3A & C-D	*w1118/Y;UAS-HTT$_{ex1}$Q25-V5/Or47b-Gal4;UAS-MapHS/+*
Figure 3B-D	*w1118/Y;UAS-HTT$_{ex1}$Q91-V5/Or47b-Gal4;UAS-MapHS/+* ;
Figure 3C	*w1118/Y;repo-Cas9/Or47b-Gal4;UAS-MapHS/gRNA-draper*
Figure 4A & C	*w1118/Y;+/+;UAS-pHluorin-HTT$_{ex1}$Q25-tdTomato/Orco-Gal4*
Figure 4B-C	*w1118/Y;+/+;UAS-pHluorin-HTT$_{ex1}$Q91-tdTomato/Orco-Gal4*
Figure 4D & F	*w1118/Y;+/+;UAS-pHluorin-HTT$_{ex1}$Q25-tdTomato/+;OK107-Gal4/+*
Figure 4E-F	*w1118/Y;+/+;UAS- pHluorin-HTT$_{ex1}$Q91-tdTomato/+;OK107-Gal4/+*
Figure 4G & I	*W1118/Y;Repo-Cas9/+;+/+*
Figure 4H-I	*W1118/Y;Repo-Cas9/+;gRNA-draper/+*
Figure 4J & L	*W1118/Y;Or47b-Gal4/repo-Cas9;+/UAS- UAS-pHluorin-HTT$_{ex1}$Q91-tdTomato*
Figure 4J-L	*W1118/Y;Or47b-Gal4/repo-Cas9;gRNA-draper/UAS- UAS-pHluorin-HTT$_{ex1}$Q91-tdTomato*
Figure 5A	*w1118*; *UAS-GFP/+;orco-Gal4/+* & *w1118*; *UAS-HTT$_{ex1}$Q25-GFP/+;orco-Gal4/+* & *w1118*; *UAS-HTT$_{ex1}$Q91-GFP/+;orco-Gal4/+*
Figure 5C & E	*w1118/Y*; *UAS-HTT$_{ex1}$Q25-V5/+;orco-Gal4/*Toll6^{MIMICGFP}
Figure 5D-E	*w1118/Y*; *UAS-HTT$_{ex1}$Q91-V5/+;orco-Gal4/*Toll6^{MIMICGFP}
Figure 5F & H	*w1118/Y*; *UAS-HTT$_{ex1}$Q25-V5/+;orco-Gal4/Jra.GFP*
Figure 5G-H	*w1118/Y*; *UAS-HTT$_{ex1}$Q91-V5/+;orco-Gal4/Jra.GFP*
Figure 6A-H	*w1118*; *UAS-HTT$_{ex1}$Q25-GFP/+;orco-Gal4/+* & *w1118*; *UAS-HTT$_{ex1}$Q91-GFP/+;orco-Gal4/+*

Figure 7A, A, C, E	*w1118*; *QUAS-HTT$_{ex1}$Q25-mCherry/+;orco-QF2/+*
Figure 7B-D, F-H	*w1118*; *QUAS-HTT$_{ex1}$Q91-mCherry/+;orco-QF2/+*
Figure 8A & C-D	*or67d-QF,QUAS-HTT$_{ex1}$Q91-mCherry/+;QUAS-HTT$_{ex1}$Q25-GFP/+;mz0709-Gal4/+*
Figure 8B-D	*or67d-QF,QUAS-HTT$_{ex1}$Q91-mCherry/+;QUAS-HTT$_{ex1}$Q25-GFP/+;alrm-Gal4/+*
Figure 9A-B, E	(control) *or67d-QF,QUAS-HTT$_{ex1}$Q91-mCherry/+;+/+;mz0709-Gal4 /+ & or67d-QF,QUAS-HTT$_{ex1}$Q91-mCherry/+;+/+;mz0709-Gal4/UAS-RNAi-X & or67d-QF,QUAS-HTT$_{ex1}$Q91-mCherry/+; UAS-RNAi-X /+;mz0709-Gal4/+*
Figure 9C-E	(control) *or67d-QF,QUAS-HTT$_{ex1}$Q91-mCherry/+;+/+;repo-Gal4,Gal80^{ts}/UAS-RNAi-mCherry & or67d-QF,QUAS-HTT$_{ex1}$Q91-mCherry/+;+/+;repo-Gal4,Gal80^{ts}/UAS-RNAi-Ets21c*
Figure 10A & C-D & F	*w1118/Y;UAS-HTT$_{ex1}$Q25-GFP/+;orco-Gal4/+*
Figure 10B-C & E-H	*w1118/Y;UAS-HTT$_{ex1}$Q91-GFP/+;orco-Gal4/+*
Figure 11A & G-I	*w1118/Y;QUAS-HTTex1Q25-mCherry/UAS-LAMP1-GFP;orco-QF2/repo-Gal4*
Figure 11B-C & G-I	*w1118/Y;QUAS-HTTex1Q91-mCherry/UAS-LAMP1-GFP;orco-QF2/repo-Gal4*
Figure 11D & G-I	*w1118/Y;QUAS-HTTex1Q25-mCherry/UAS-GFP-LAMP1;orco-QF2/repo-Gal4*
Figure 11E-I	*w1118/Y;QUAS-HTTex1Q91-mCherry/UAS-GFP-LAMP1;orco-QF2/repo-Gal4*
Figure 12A-B & E-G	Control: *QUAS-HTT$_{ex1}$Q25-GFP/+/+;repo-Gal4,orco-QF2/UAS-mCherry-LGals3 & QUAS-HTT$_{ex1}$Q91-GFP/+/+;repo-Gal4,orco-QF2/UAS-mCherry-LGals3*
Figure 12C-G	Control: *QUAS-HTT$_{ex1}$Q25-GFP/+/+;repo-Gal4,orco-QF2/UAS-mCherry-LGals8 & QUAS-HTT$_{ex1}$Q91-GFP/+/+;repo-Gal4,orco-QF2/UAS-mCherry-LGals8*
Fig 13A-C	Control*: UAS-HTT$_{ex1}$Q25-GFP/Or67d-QF,QUAS-HTT$_{ex1}$Q91-mCherry;+/+;repo-Gal4/UAS-RNAi.mCherry & UAS-HTT$_{ex1}$Q25-GFP/Or67d-QF,QUAS-mHTT-mCherry;+/+;repo-Gal4/UAS-RNAi-X* or *UAS-HTT$_{ex1}$Q25-GFP//Or67d-QF,QUAS-mHTT-mCherry /+;UAS-RNAi-X/+ ; repo-Gal4/+*
Figure 14A-C	*Or67d-QF,QUAS-HTT$_{ex1}$Q91-mCherry /+;QUAS- HTT$_{ex1}$Q25-GFP/UAS-RNAi-X;repo-Gal4/+ & Or67d-QF,QUAS-HTT$_{ex1}$Q91-mCherry /+;QUAS-HTT$_{ex1}$Q25-GFP/+;repo-Gal4/UAS-RNAi-X*
Figure 14D-E	*Or67d-QF,UAS-HTTex1Q25-GFP/+ ; GH146-Gal4,QUAS-HTTex1Q91-mCherry/+ & Or67d-QF,UAS-HTTex1Q25-GFP/+ ; GH146-Gal4,QUAS-HTTex1Q91-mCherry/+ ; drprD5/+ & Or67d-QF,UAS-HTTex1Q25-*

	GFP/rab10{CRISPR-KO} ; GH146-Gal4,QUAS-HTTex1Q91-mCherry/+ & Or67d-QF,UAS-HTTex1Q25-GFP/rab10{CRISPR-KO} ; GH146-Gal4,QUAS-HTTex1Q91-mCherry/+ ; drprD5/+ & Or67d-QF,UAS-HTTex1Q25-GFP/rab10CRISPR ; GH146-Gal4,QUAS-HTTex1Q91-mCherry/rab14{CRISPR-KO} & Or67d-QF,UAS-HTTex1Q25-GFP/rab10CRISPR ; GH146-Gal4,QUAS-HTTex1Q91-mCherry/rab14{CRISPR-KO} ; drprD5/+
Figure 14F	*UAS-HTT$_{ex1}$Q25-GFP,QUAS-HTT$_{ex1}$Q91-mCherry/Or67d-QF;+/+;repo-Gal4/+ & UAS-HTT$_{ex1}$Q25-GFP,QUAS-HTT$_{ex1}$Q91-mCherry/Or67d-QF;+/+;repo-Gal4/UAS-RNAi-Rab10 & UAS-HTT$_{ex1}$Q25-GFP,QUAS-HTT$_{ex1}$Q91-mCherry/Or67d-QF;UAS-draper-I/+;repo-Gal4/UAS-RNAi-Rab10*
Figure 14G	*w1118/ w1118;+/+;+/+ (w1118) & Rab10(CRISPR-KO)/w1118;+/+;+/+ & Rab10(CRISPR-KO)/ Rab10(CRISPR-KO);+/+;+/+*
Figure 15A	controls: *w1118*; *UAS-GFP/+;orco-Gal4/+* & *w1118*; *UAS-HTT$_{ex1}$Q25-GFP/+;orco-Gal4/+* & *w1118*; *UAS-HTT$_{ex1}$Q91-GFP/+;orco-Gal4/+*
Figure 15B-C & H-I	*TI{TI}Rab10[EYFP]/Y;UAS-HTT$_{ex1}$Q25-V5/+;orco-Gal4/+ & TI{TI}Rab10[EYFP]/Y;UAS-HTT$_{ex1}$Q91-V5/+;orco-Gal4/+*
Figure 15D-E & H-I	*w1118/Y;UAS-HTT$_{ex1}$Q25-V5/TI{TI}Rab5[EYFP];orco-Gal4/+ & w1118/Y;UAS-HTT$_{ex1}$Q91-V5/TI{TI}Rab5[EYFP];orco-Gal4/+*
Figure 15F-I	*w1118/Y;UAS-HTT$_{ex1}$Q25-V5/+;orco-Gal4/TI{TI}Rab7[EYFP] & w1118/Y;UAS-HTT$_{ex1}$Q91-V5/+;orco-Gal4/ TI{TI}Rab7[EYFP]*
Figure 16A-B & G-I	*w1118/Y;QUAS-HTTex125-mCherry/UAS-YFP-Rab10;orco-QF2,repo-Gal4/+ & w1118/Y;QUAS-HTTex1Q91-mCherry/UAS-YFP-Rab10;orco-QF2,repo-Gal4/+*
Figure 16C-D & 16G-I	*w1118/Y;QUAS-HTTex125-mCherry/UAS-YFP-Rab5;orco-QF2,repo-Gal4/+ & w1118/Y;QUAS-HTTex1Q91-mCherry/UAS-YFP-Rab5;orco-QF2,repo-Gal4/+*
Figure 16E-I	*w1118/Y;QUAS-HTTex125-mCherry/UAS-YFP-Rab7;orco-QF2,repo-Gal4/+ & w1118/Y;QUAS-HTTex1Q91-mCherry/UAS-YFP-Rab7;orco-QF2,repo-Gal4/+*
Figure 17A1-3	*w1118/Y;QUAS-HTTex1Q91-mCherry/UAS-YFP-Rab10;orco-QF2,repo-Gal4/+*
Figure 17B1-2	*w1118/Y;QUAS-HTTex1Q91-mCherry/UAS-YFP-Rab5;orco-QF2,repo-Gal4/+*
Figure 17C1-2	*w1118/Y;QUAS-HTTex1Q91-mCherry/UAS-YFP-Rab7;orco-QF2,repo-Gal4/+*

Table 3. Primer sequences used for qPCR analyses.

Gene Target	Forward (F) and Reverse (R) Primer Sequences (5'-3')
rpl32	F: CCGCTTCAAGGGACAGTATCTG R: ATCTCGCCGCAGTAAACGC
toll-6	F: AATATTGTGGAGTGCTCGGG R: GCGTTTAAGGCCACTGAAAG
dorsal	F: ATGCGAGCGGTGTTCAGTAA R: ACGATGCGAAAAGCCAGTCT
relish	F: ACAGGACCGCATATCG R: GTGGGGTATTTCCGGC
draper-I	F: TGTGATCATGGTTACGGAGGAC R: CAGCCGGGTGGGCAA
mmp1	F: GAAGGCTCGGACAACGAGT R: GTCGTTGGACTGGTGATCG
ets21c	F: CAACGACGACGAACCAAAT R: GTTCGCGTTGGACGAATC
rab10	F: ACATCCGCCAAGTCGAACAT R: CTGGTTCCGGCGATCGATAA
rab5	F: AGTCCGCTGTGGGCAAGTC R: CTCCTGGTACTCGTGGAACTGTC
rab7	F: AATTTTGCACGCAACCGCTG R: GAGTAGCCAATTCGATGGTGC
drosomycin	F: GCTGTCCTGATGCTGGTGGT R: CGGAAAGGGACCCTTGTATCTTC
attacin-a	F: CTCGTTTGGATCTGACCAAGG R: CCATGACCAGCATTGTTGTAG
attacin-d	F: CGTTGAGGTTGAGATTGCCACT R: CGGTCCCTCAGTTCGGCATGAC
diptericinA	F: CCACCGCAGTACCCACTCAAT R: CGATGACTGCAAAGCCAAAACCA
metchnikowin	F: CAGTGCTGGCAGAGCCTCAT R: CGTCGGTTAGGATTGAAGGGCGA